

STUDIES OF HUNTINGTON'S DISEASE ASSOCIATED MOTOR DOMAIN
PHOSPHORYLATION OF KINESIN-1

BY

HANNAH A DEBERG

DISSERTATION

Submitted in partial fulfillment of the requirements
for the degree of Doctor of Philosophy in Physics
in the Graduate College of the
University of Illinois at Urbana-Champaign, 2013

Urbana, Illinois

Doctoral Committee:

Assistant Professor Yann Chemla, Chair
Professor Paul R. Selvin, Director of Research
Associate Professor Aleksei Aksimentiev
Professor Paul Kwiat

Abstract

In neurons, microtubule motor driven transport is crucial for communication between processes and the cell body. Disruptions in transport are associated with a variety of neurodegenerative diseases. Recent studies implicate phosphorylation of serine 175, a conserved residue found in all three isoforms of kinesin-1 in impaired axonal transport associated with Huntington's disease. Phosphorylation adds both negative charge and bulk to a protein. The mechanism by which S175 modification is related to impaired transport is not very well understood. It is not known whether phosphorylation of kinesin alone is sufficient to cause impaired cargo transport. To investigate the isolated effect of residue 175 on kinesin transport, we used optical trapping and single-molecule fluorescence imaging to study purified kinesin. We found no significant difference in the processivity or ATPase activity of a phosphomimetic S175D construct or the non-phosphorylatable S175A construct. However, we did find that addition of a negative charge at S175 through phosphorylation or mutation led to a decreased stall force. Furthermore, polystyrene bead cargos coated with dynein and kinesin traveled preferentially in the minus direction when residue 175 of kinesin was negatively charged. These results show that modification of serine 175 alone is sufficient to alter the behavior of kinesin.

Acknowledgements

I would like to thank the many people whose support made this work possible. I would like to thank my adviser, Paul Selvin for his support and the opportunity to work in his lab. His enthusiasm for science was always an inspiration. I was fortunate to work with many wonderful individuals in the Selvin lab who were both great collaborators and friends: Benjamin Blehm, Janet Sheung, Melinda Tonks-Hoffman, Pinghua Ge, Paul Simonson, Ruobing Zhang, HyeonJun Kim, Murat Baday, Sank Hak Lee, En Cai, Tobias Rosencrantz, Yong Wang, Marco Tjioe, and Eli Rothenberg. I would also like to thank Ward Lopes for advice during the semester he spent in Champaign and Nir Friedman, who developed the hidden markov model theory in collaboration with the Selvin lab. In addition to the Selvin group at UIUC, I was lucky to collaborate with fantastic scientists at many different institutions. The kinesin studies would not have been possible without the protein and knowledge shared by Kathy Trybus, Chris Berger, Andrew Thompson and Carol Bookwalter at the University of Vermont. The generosity and knowledge of Bill Green and his lab at the University of Chicago was crucial for work involving nicotinic acetylcholine receptors.

I would like to thank my family for their support. My mom, dad, Vera and Duwayne have supported me throughout my graduate studies. I would like to thank Dan for many flights in between Champaign and Seattle and for making sure that I was always adequately supplied with chocolate.

Work with kinesin motors was supported by NIH Grant R01 AR44420 and acetylcholine receptor work was supported by NIH Grant R01 GM086214. I would also like to acknowledge support from the National Science Foundation Graduate Research Fellowship, the L.S. Edelheit Family Biological Physics Fellowship, the Linda Su-Nan Chang Sah Doctoral Fellowship, and the UIUC SURGE (Support for Under-Represented Groups in Engineering) Fellowship.

Table of Contents

Chapter 1: Introduction and Background.....	1
Chapter 2: Materials and Methods.....	32
Chapter 3: Results.....	63
Chapter 4: Conclusions.....	80
Chapter 5: Future Experiments.....	84
Chapter 6: SHRImP Measurements of Ion Channels.....	87
Appendix: Glossary of Biological Terms.....	102

Chapter 1: Introduction and Background

This chapter will introduce the study of a modification of one cytoskeletal motor, kinesin. This modification, called phosphorylation, involves the addition of a phosphate group in the kinesin motor domain and has been linked to neurodegenerative disease. Microtubule-based cytoskeletal motors and the biophysical techniques used to study these motors will be introduced.

Section 1.1: Intracellular Transport

The inside of a cell is a complex, crowded environment. To survive, a cell must ensure that all of the components within it exist at the right locations at the right time. For small cells, such as bacteria, the problem of moving intracellular components around is solved by simple diffusion. A typical protein inside a cell has a diffusion coefficient of 5-15 $\mu\text{m}^2/\text{s}$ (1). The time to cross a cell can be solved from the relationship between the diffusion coefficient and mean-squared displacement in 3 dimensions:

$$\langle x^2 \rangle = 6Dt.$$

For *E. coli*, which is approximately 1-2 μm long, this corresponds to approximately 10-100 ms for a protein to move across the cell (Figure 1.1A). This is fast enough for bacteria, which do rely on diffusion to move components from one location in the cell to another. In mammalian cells, which are much larger than bacteria, the time scales associated with using diffusion to move components to the correct positions become problematic. A typical mammalian cell is around 20 μm in diameter, which corresponds to 10 seconds for diffusion to move a protein from one end of the cell to the other, two to three orders of magnitude slower than in *E. coli*. While protein lifetimes vary from a few minutes to several weeks, diffusion in a typical mammalian cell would still be a viable transport mechanism for most proteins, but would not function well for both the shortest-lived proteins and large, membrane-enclosed organelles with much lower diffusion coefficients.

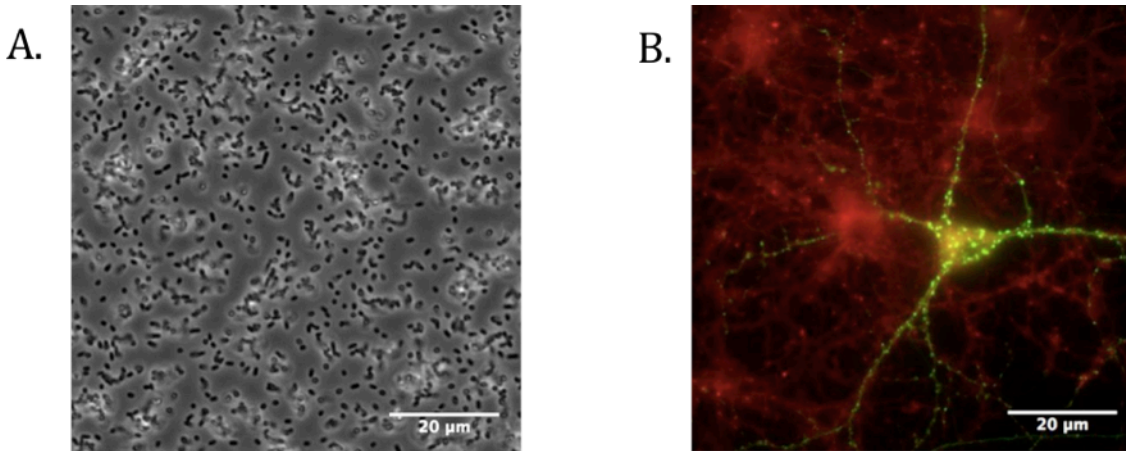


Figure 1.1: Size of different cell types. A. Bright-field image of *E. coli* cells. A typical *E. coli* bacterium is 2 μm long. B. Fluorescence image of a neuron with many processes that extend for hundreds of microns. Red is a mitochondria marker while green is fluorescent Homer1. The image of a neuron was recorded by En Cai.

In neurons, the problem of transport becomes a concern (Figure 1.1B). A typical neuron is made of a central cell body from which many dendrites and a single axon extend (Figure 1.2). In humans, axons vary from 1 mm to 1m in length with the longest axon belonging to the sciatic nerve, which stretches from the base of the spine to each foot. It would take diffusion over 1,000 years to move a protein from the base of the spine to the foot down the axon of the sciatic nerve.

Transport in neurons and all other eukaryotic cells does not depend only on diffusion, as it is too slow and undirected. Eukaryotic cells contain a nucleus. Animals, plants, fungi and a number of unicellular organisms are all eukaryotes. In these cells, molecular motors carry cargo along cytoskeleton tracks within the cell. These are a set of proteins that bind cargo and walk along polymer filaments. The primary proteins involved in transport are the motors kinesin-1 and dynein. The filamentous tracks that the motors move on are made up of tubulin. These tracks extend down axons and dendrites in neurons and out from the nucleus in other eukaryotic cells. Tubulin units polymerize into microtubule tracks that have polarity. The “plus ends” of these

tracks are positioned at the tip of the axon, away from the cell body, while the “minus ends” are located closer to the cell body (Figure 1.2). Kinesin is responsible for plus end directed transport, while dynein moves toward the minus end.

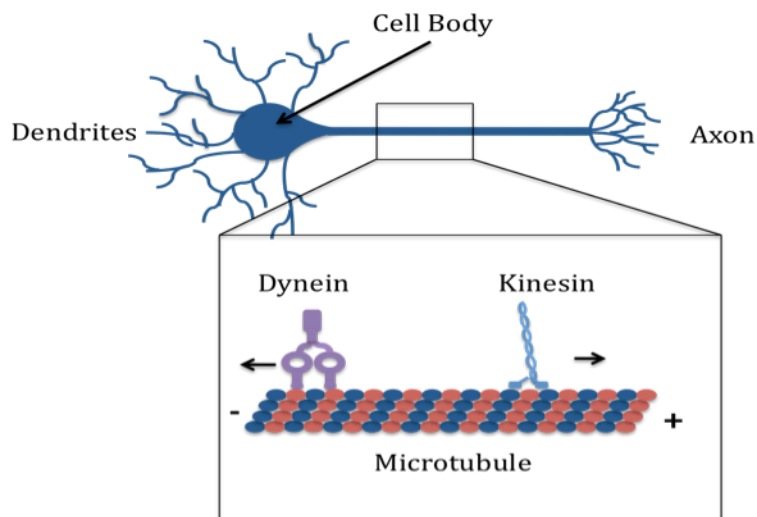


Figure 1.2: Microtubule motor transport in neurons. The axons of neurons are densely packed with microtubules with plus ends pointing toward the axon tip. Kinesin is a molecular motor that carries cargo toward the plus end of microtubules and dynein carries cargo toward the minus end.

Many mechanisms are used by cells to regulate microtubule motor-based transport and direct cellular traffic (2). Cargo, tracks, and motors are modified to control the flow of traffic within the cell. Cargo attachment is regulated by a variety of scaffolding proteins that can specifically link cargo to a certain motor species (3). Microtubule tracks can be coated with tau and other microtubule-associated proteins (MAPs), which modify transport (4, 5). Both kinesin and dynein motors are also modified: for example, dynein is regulated by a large number of activator proteins that bind to it and modulate transport. Modification of kinesin-1 light chains, the parts of the protein that mediate attachment to cargo, is known to affect the association of cargo with the motor (6-9).

Every neuron has a single axon, which is a long, narrow process that extends off the cell body. The axon of one neuron contacts the dendrites of adjacent neurons at synapses. Neurons communicate through electrical and chemical signals that move across synapses. Most protein synthesis in a neuron takes place in the cell body, so the ability of kinesin to move proteins and organelles down axons is crucial for the normal functioning of the nervous system. Defects in the regulation of axonal transport play an important role in a number of neurological disorders, including Alzheimer's disease, Amyotrophic Lateral Sclerosis, Huntington's disease, and Spinal and Bulbar Muscular Atrophy (SBMA) (10, 11).

Section 1.2: Kinesin-1 Phosphorylation and Neurodegenerative Disease

Studies have implicated the misregulation of kinesin in Huntington's disease and SBMA, two incurable neurodegenerative disorders (12-16). In Huntington's disease, neurons in the brain degenerate and die over time, leading to a loss of control of motion, personality changes, dementia, and death. The loss of brain matter associated with Huntington's is illustrated in Figure 1.3. A 20-30% reduction in the volume of brain matter can occur (17). Huntington's disease affects 5-10 out of every 100,000 people.

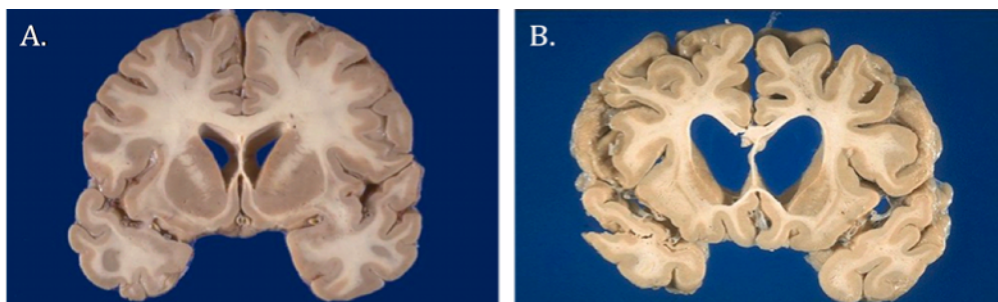


Figure 1.3: A. Normal brain B. Huntington's disease affected brain. Images from marcora.caltech.edu/science.htm.

In SBMA, motor neurons in the brain stem and spine degenerate, resulting in progressive muscle weakness and atrophy. SBMA is an X-chromosome-linked disease that affects fewer than 1 in 150,000 males (females are not affected by SBMA) (18, 19). Both Huntington's and

SBMA are genetic, trinucleotide-repeat diseases that are caused by excessive repetitions of the coding sequence for the amino acid glutamine (18-20). An expanded polyglutamine tract in the gene for huntingtin protein causes Huntington's disease, while in SBMA, the disease is due to polyglutamine repetitions in the androgen receptor. Table 1 displays the relationship between the number of glutamine repetitions in these genes and disease pathology.

DISEASE	NUMBER OF GLUTAMINE REPETITIONS	EFFECT
Huntington's	Less than 26	No disease
	27-35	No disease, increased risk in offspring
	36-39	Possible disease, later onset, reduced severity, 50% chance of passing disease to offspring
	40+	Disease, 50% chance of passing disease to offspring
SBMA	Less than 34	No disease
	35	No consensus as to whether there is a elevated risk of disease
	36-37	Possible disease, but reduced severity
	38+	Disease

Table 1.1: The relationship between the number of glutamine repetitions and disease state for Huntington's disease and SBMA (19, 20).

Although it is well established that Huntington's is a polyglutamine repeat disorder which occurs when more than 36-40 glutamine repetitions occur on the huntingtin protein, the function of huntingtin in the cell is poorly understood, but it is known to play some role in vesicle transport, endocytosis, cell signaling and apoptosis (21). In contrast, the role of the androgen receptor is better understood. It binds to DNA and regulates the expression of a variety of sex-linked genes. Despite their different roles, both mutant huntingtin and mutant androgen receptor are linked to a decrease in axonal transport via the activation of c-Jun N-terminal kinase-3 (referred to as JNK3), a stress-signaling protein that phosphorylates the motor domain of kinesin. The motor domain of kinesin is the region responsible for binding to microtubules and hydrolyzing ATP, kinesin's energy source.

As a serine kinase, the role of JNK3 is to covalently attach a phosphate group to serine residues on other proteins (see Figure 1.4). It does this by reacting with its substrate, which is kinesin in this case, and a molecule of adenosine triphosphate (ATP), the energy currency of the cell. At neutral pH, the phosphate group has a charge of approximately $-2e$, while serine alone has no charge. Thus, the addition of a phosphate decreases a protein's charge and also adds some bulk, slightly increasing the size of the phosphorylated serine. Phosphorylation by a kinase generally modifies the behavior of the substrate protein and is frequently used as a switch to turn proteins "on" or "off" as needed. Once activated by a cellular signal, a typical kinase will phosphorylate many different substrate proteins, amplifying the effect of the signal. The JNK family of kinases (which includes JNK1, JNK2, and JNK3) are stress signaling kinases that phosphorylate proteins in response to environmental cellular stressors such as UV radiation, heat shock and osmotic shock. Of these three, JNK1 and JNK2 are found throughout all mammalian body cells and JNK3 is specific to the nervous system (22).

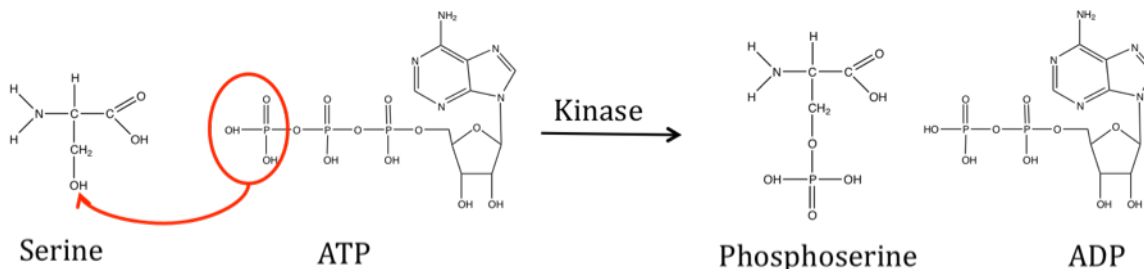


Figure 1.4: Phosphorylation of serine by a kinase. Serine is one of three amino acids that can be phosphorylated (the other two are tyrosine and threonine). A kinase is an enzyme that transfers a phosphate group from ATP to an amino acid residue, creating a phosphorylated protein and ADP. At neutral pH, the phosphate group has a charge of $-2e$.

Morfini et al. linked mutant huntingtin and mutant androgen receptor to an increase in activated JNK3 (13, 14). Using mass spectrometry, they discovered that JNK3 phosphorylates a serine that is found in all isoforms of kinesin-1 and is therefore said to be a "conserved" serine (14). In mammals, kinesin-1 occurs in three similar isoforms called "A", "B", and "C". JNK3 specifically

phosphorylates serine 176 in the A and C isoforms and serine 175 in the B isoform. The numbering of amino acids is based on the convention that the first amino acid in a protein is located at the “N” terminus, or end of the protein with an exposed amino group. Under this convention, serine 175(176) is the 175th(176th) amino acid in kinesin.

Morfini and Brady also established a link between addition of a negative charge at serine 175/6 of kinesin and decreased axonal transport. They created a mutant form of kinesin in which the serine was replaced with a glutamine residue. Glutamine has a negative charge of approximately -1e at neutral pH and is slightly bulkier than serine. The negative charge and added bulk make it a common biological model used to mimic phosphorylation. In addition to the phosphomimetic mutation, a green fluorescent protein was attached to the kinesin for visualization in a fluorescence microscope. Upon expression of the mutant kinesin in rat neurons, less phosphomimetic kinesin was found in the axon tips than wild-type kinesin, suggesting a defect in the ability of the phosphomimetic kinesin to move along the microtubules in the axon.

The Morfini, et al. studies did not suggest a mechanism for how addition of a negative charge could alter the behavior of kinesin. There are many unanswered questions regarding the mechanism by which JNK3 phosphorylation of kinesin leads to impaired transport. It is not known whether the addition of negative charge due to phosphorylation alone is sufficient to cause impaired cargo transport. It is also unknown what biochemical and biophysical properties of kinesin are modified as a result of S175/6 phosphorylation. To investigate the isolated effect of residue 175 on kinesin transport, we used optical trapping and single-molecule fluorescence imaging to probe the behavior of two kinesin mutants: a phosphomimetic construct S175D and a non-phosphorylatable construct S175A. We also used JNK3 to directly phosphorylate kinesin. We find that both phosphorylation and the S175D mutation attenuate the motor’s stall force and

bias cargo transport toward the minus end of microtubules. Thus, we conclude that phosphorylation alone is sufficient to alter the behavior of kinesin and thus affect transport. In order to develop an understanding of how phosphorylation could affect kinesin transport, the structure and function of the major players in microtubule transport must be first be considered. We therefore spend the rest of this section describing the key proteins involved in microtubule-based motility and the techniques that permit the investigation of these proteins at both at the single-molecule level and in bulk assays.

Section 1.3: Microtubules as Cellular Highways

Microtubules are polymers that are part of the cytoskeleton. They provide structure to the cell, helping it to maintain its shape and also act as tracks along which motor proteins can carry cargo. They can be up to 25 μm long and are around 25 nm in diameter. They are hollow cylinders made up of protofilaments of tubulin dimers (Figure 1.5 A and B). Most microtubules inside a cell contain 13 protofilaments, but the number can vary from 8-19, depending on polymerization conditions (23, 24). The alpha and beta tubulin dimer is the basic unit from which protofilaments form. The end-to-end attachment of the tubulin dimers, with the fact that protofilaments form parallel to each other means that one end of the microtubule will have exposed alpha tubulin while beta tubulin will be exposed at the other end. This gives the microtubule polarity. The end with exposed alpha subunits is called the minus end and the end with exposed beta subunits is the plus end. Polymerization at the plus end is much more rapid than from the minus end. Inside a cell, most microtubules are oriented such that the minus ends are near the nucleus with the plus ends pointing radially outward. Transport from the center of the cell outward is called anterograde and transport from the membrane in toward the center of the cell is referred to as retrograde movement.

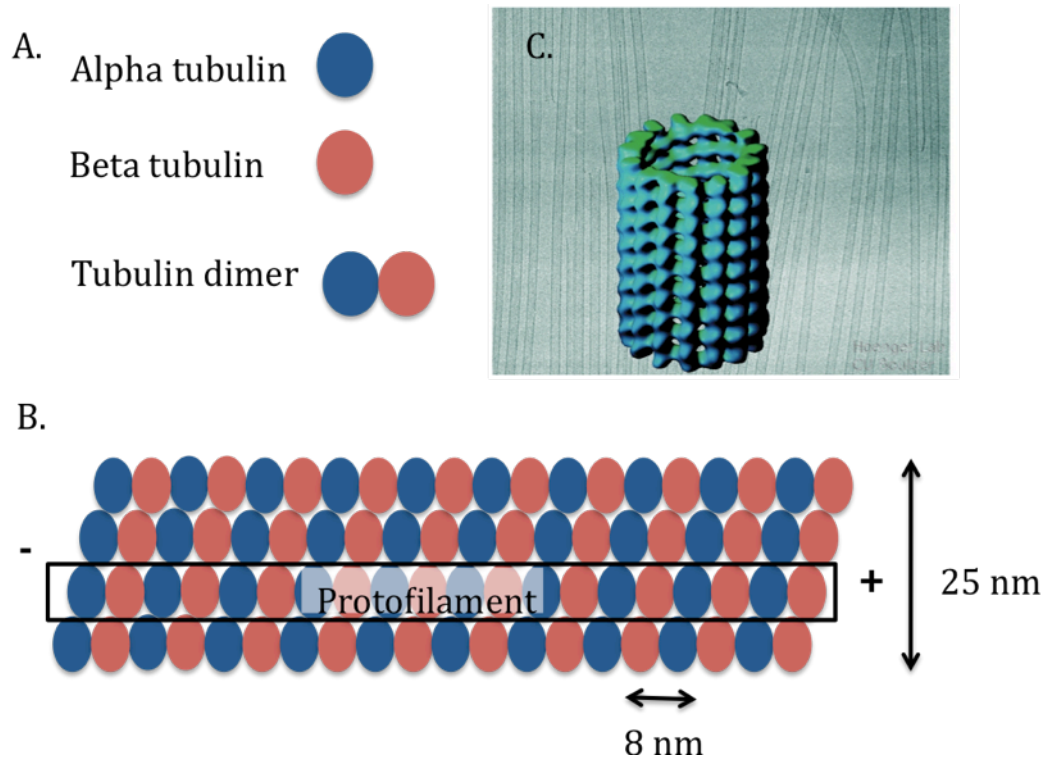


Figure 1.5: Microtubules. A. Tubulin monomers bind to form dimers. B. Dimers polymerize in protofilaments that form a hollow tube known as a microtubule. C. EM image and 3-D reconstruction of microtubules, from the Andreas Hoenger Lab at CU Boulder, <http://hoengerlab.colorado.edu/docs/mm1.html>.

Section 1.4: Kinesin, a Strong, Plus End Motor

The kinesin superfamily is a class of over 40 different proteins that hydrolyze ATP and move along microtubules. They are found in all eukaryotic cells. Most members of the family are plus end directed motors and play a role in transport or cellular division (25). Kinesin-1, also called conventional kinesin, is the prototypical superfamily motor. It is responsible for the transport of diverse cargos such as vesicles, organelles, mRNA, and chromosomes.

Kinesin-1 (referred to as “kinesin” hereafter for simplicity) is made up of two 120-130 kilodalton (kDa) heavy chains and two 60-70 kDa light chains as is shown in Figures 1.6 and 1.7. The light chains are not essential for motor function, but rather play a role in cargo-binding and motor

regulation. There are two different light chain isoforms, KLC1 and KLC2. Different types of cargo bind to different light chain isoforms, but the two light chain isoforms attached to the heavy chains are always identical (26). The heavy chains consist of three regions, an N-terminal motor domain, or “head”, a coiled-coil stalk and a C-terminal domain that associates with the light chains to bind cargo. The two heavy chains dimerize along the stalk region to form a motor with two motor domains and two C-terminal domains.

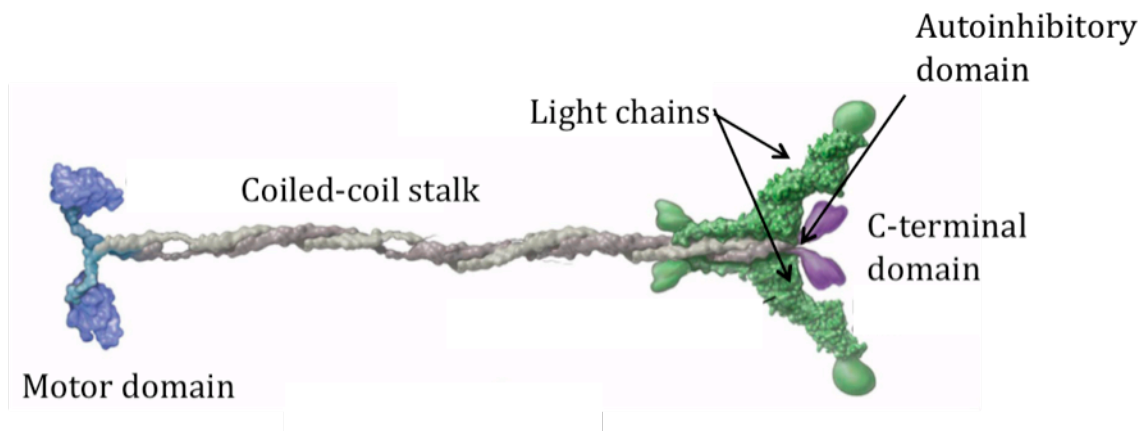


Figure 1.6: Kinesin-1. The motor domains which bind to microtubules and hydrolyze ATP are shown in blue. The coiled-coil stalk is in grey, the cargo-binding domain is purple and the light chains are in green. The autoinhibitory domain consists of residues within the C-terminal domain. From Vale, 2003 (27).

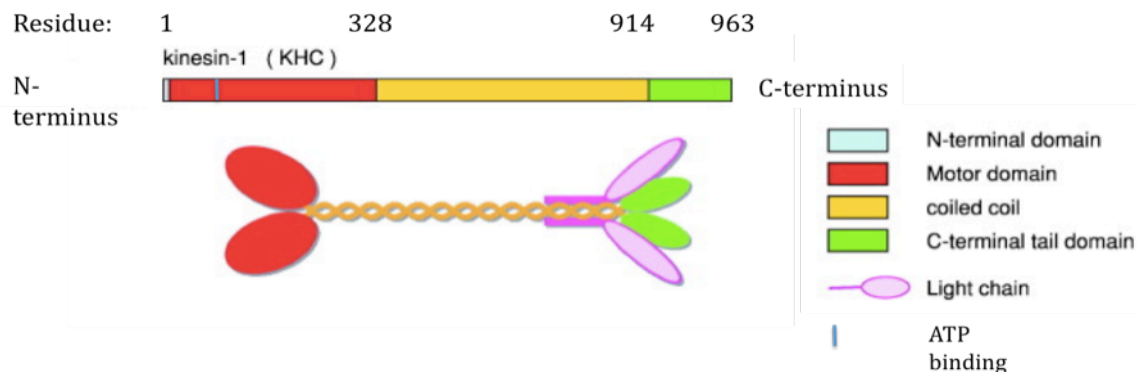


Figure 1.7: Kinesin-1 domains according to residue number in isoform “B”. The motor domain is made up of residues 1-328. The stalk consists of 329-914 and the C-terminal domain consists of 915-963. From Marx, 2005 (28).

The motor domain binds to microtubules and hydrolyzes ATP, which provides the energy for kinesin to walk along the microtubule in a hand-over-hand manner. As it walks, kinesin moves along a single protofilament, taking 8 nm steps in a hand-over-hand style (29, 30). With every step, kinesin hydrolyzes a single molecule of ATP (31). Kinesin is a highly processive motor; it will take approximately 100 steps before dissociating from a microtubule. A single molecule will walk along a microtubule for $\sim 1 \mu\text{m}$ before dissociating and several kinesin working together can have run lengths greater than $10 \mu\text{m}$ (32). Under conditions of saturating ATP, as is the case inside the cell, kinesin moves at a speed of $\sim 1 \mu\text{m/s}$. A single kinesin molecule is capable of exerting force up to 5-7 pN (33, 34). The maximum force kinesin can exert is called its “stall force”. Under no load, kinesin steps toward the plus end of the microtubule almost all of the time, taking backward steps toward the microtubule minus end less than 5% of the time (35). Under a load, backwards steps become more common, approaching the frequency of forward steps as the load applied to kinesin approaches its stall force (34, 35).

Near the C terminus, kinesin has an autoinhibition domain (Figure 1.6). When not bound to cargo, kinesin adopts a folded configuration in which the autoinhibition domain docks at the motor domain (36, 37). In such a folded configuration, kinesin cannot hydrolyze ATP and has greatly reduced motility (38, 39). Cargo binding to kinesin relieves the autoinhibition, unfolding kinesin and restoring motility (38). Physiologically, autoinhibition is thought to prevent kinesin from unnecessarily hydrolyzing ATP when it is not needed for cargo transport.

In mammals, there are three different isoforms of the kinesin heavy chain, labeled A, B, and C. The A and C isoforms are expressed only in neurons, but B is expressed in all cell types (40). Only recently differences in isoform function have begun to be investigated, but there is evidence that the transport of some types of intracellular cargo is isoform specific (41-43).

A conserved serine in all three isoforms, serine 176 in the A and C and serine 175 in the B isoform, can be phosphorylated by JNK3 (Figure 1.8). All experiments performed for this dissertation used the kinesin-1B isoform in which S175 is the relevant residue. S175 is located in the motor domain of kinesin, but does not fall in the ATP binding domain (residues 97-104) or the microtubule binding-domain (44, 45). However, computational and experimental studies of kinesin-microtubule interactions have traditionally focused on mutagenesis studies in which alanine is used to replace positive residues in the motor head, while the effect of adding an extra negative charge has not been investigated thoroughly (44, 45).

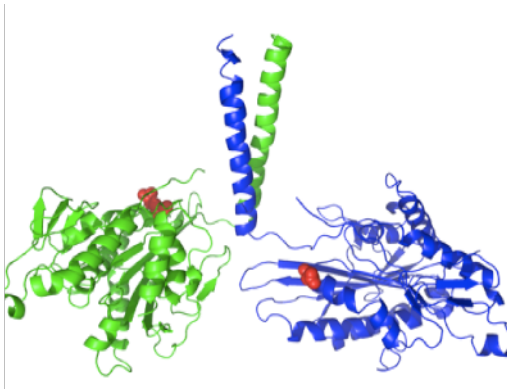


Figure 1.8: Motor domain and location of S176. The motor domain of kinesin is shown in blue and green with serine 176 highlighted in red. The figure was created by Yong Wang, using the PDB ID: 3KIN structure (46,47).

Section 1.5: Dynein, a Minus End Motor

Although dynein is the minus end directed counterpart to kinesin, it is a very different motor. In contrast to kinesin, which has been extensively studied and is well understood, there are many open questions about how mammalian dynein functions and is regulated. All three kinesin isoforms have been cloned and can be expressed heterologously and purified. This has permitted detailed studies of point mutations of kinesin and the attachment of fluorescent proteins and other tags; two developments that have been useful for tracking the motor. In contrast, mammalian dynein has not been successfully cloned purified in a non-native expression system (largely due to its large size), but instead must be purified from native tissue

and can therefore not be mutated or tagged with fluorescent proteins for tracking. Also, while there is a large superfamily of kinesin proteins, and different family members can exist as different isoforms, there are only two types of dynein. The first type, axonemal dynein, powers the beating motion of cilia and flagella, two microtubule rich structures, but does not play a role in transport. The second type, cytoplasmic dynein, is the only minus end directed microtubule motor that transports cargo in cells and will be referred to as “dynein” hereafter.

Dynein is a large multi-subunit protein (Figure 1.9). It is 1.5 MDa in size, making it over 4 times as massive as kinesin. Dynein consists of two 530 kDa heavy chains, six 50-75 kDa intermediate chains, and several light chains of approximately 10 kDa. The heavy chains are responsible for motility. Each contains one microtubule binding site and four ATP binding sites. Unlike kinesin, in which the ATP and microtubule binding sites are separated by only a few nanometers and the coupling of ATP to stepping is well understood, dynein’s ATP binding sites are located in a ring that is separated from the microtubule binding domain by a 15 nm long stalk. There are unanswered questions about how ATP binding in the rings is communicated down the stalk to the microtubule-binding domain. Studies in yeast and dictyostelium dynein suggest that ATP hydrolysis is coupled to stepping via sliding of the stalk coils, but the behavior of mammalian dynein has not been probed (48-50). The intermediate chains mediate cargo binding and the function of the light chains is poorly understood.

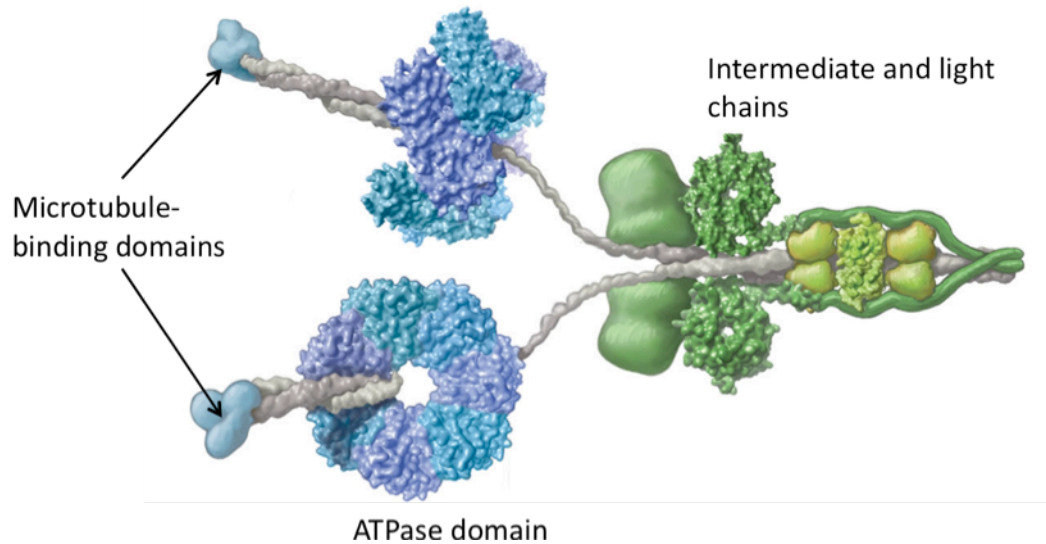


Figure 1.9: Dynein structure (combination of known structures and artist's interpretation). The microtubule binding domains are shown in light blue, the ATPase domains are in blue and purple, and the intermediate and light chains are in green. From Vale (27).

Like kinesin, dynein is a processive motor. Yeast dynein is very processive, with a run-length of approximately $1 \mu\text{m}$. Mammalian dynein is slightly less processive with reported run lengths of 300-900 nm (51-54). Unlike kinesin, which only takes 8 nm steps along a single protofilament, dynein is capable of stepping in multiples of 8 nm and can take off-axis steps across different protofilaments (51, 52). Furthermore, backwards stepping in which dynein moves toward the plus end of microtubules is observed even in the absence of a load (51, 55). This contrasts with kinesin, which only takes backward steps 5% of the time when no load is present, but will take more backward steps in response to an increasing load until, at a load equal to its stall force, kinesin takes equal numbers of backwards and forwards steps. Furthermore, kinesin walks strictly in a hand-over-hand manner in which the trailing head is always the head to step forward, but both the trailing and leading heads of dynein can take forward steps, suggesting that the ATPase activity of the two heavy chain monomers is uncoordinated (56, 57). However, most of these studies were performed in yeast and there is evidence that there are fundamental differences in the behavior of mammalian and yeast dynein. Studies have consistently

measured a 7 pN stall force for yeast dynein, but the stall force of mammalian dynein is controversial (55). For mammalian dynein, most studies measure a 1 pN stall force, but some have measured 7 pN (53,58-60). Recent studies in two-motor transport (i.e., both kinesin and dynein) indicate that mammalian dynein interacts with the microtubule during motion toward the plus end, creating a drag force (60). Thus dynein is thought to “drag” behind kinesin. Mammalian dynein was used for the experiments in this dissertation.

Section 1.6: Fluorescent Imaging with One-Nanometer Accuracy (FIONA)

To track the motion of kinesin and dynein, sub-diffraction limited fluorescent imaging has been a valuable tool. With 8-nm step sizes, the nanometer is the relevant length scale for watching the motion of these molecules. FIONA (Fluorescence Imaging with One Nanometer Accuracy) is a very powerful technique that can be used to make such nanometer-scale measurements on motors. It was pioneered by Ahmet Yildiz in the Selvin lab. The first application of FIONA to a biological system was to measure the step size of the myosin V molecular motor with 1.5-nm precision in 2003 (61). Since then, FIONA has been applied to many other biological systems and has been very useful in tracking the diffusion of different species in the cytoplasm and cell membrane as well as in tracking motors (62). The premise behind FIONA is that one can measure the center of a point-spread function much more accurately than the diffraction limit of light, provided enough photons can be collected. To perform FIONA, single dye molecules are attached to the biological system of interest.

The emission pattern of a fluorescent dye, known as a point-spread function (PSF), can be modeled as a two-dimensional Gaussian function. Although the physical form of a point-spread function from a point source is an Airy function, an analysis by Cheezum et al. discovered that the best fit to individual dye molecules is a Gaussian function (63). The distance from the central

maximum to the first minimum of the Airy disk of a point source of light, such as a single fluorescent dye is

$$R = \frac{1.22\lambda}{2NA}$$

For a 1.4 NA microscope objective and 500 nm light, this is approximately 250 nm. However, by localizing the centroid of the Gaussian with the precision given by the standard error of the mean, the position of the dye can be determined to within a few nanometers. This is illustrated in Figure 1.10. The diffraction-limited width of the pattern of emission of a single fluorophore is around 250 nm, but the center of the emission can be located with much greater precision than 250 nm.

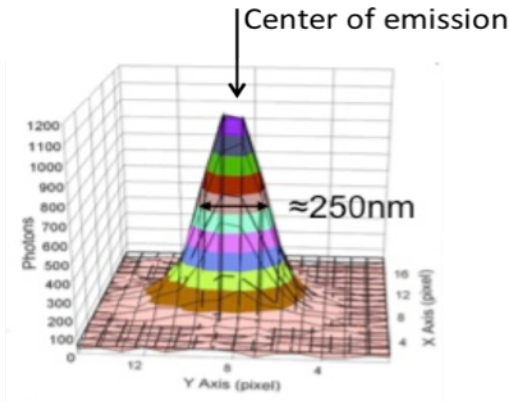


Figure 1.10: Fluorescence from a single dye molecule. From Yildiz, et al. (61).

The precision is governed by the number of photons emitted by the dye and by noise in the experimental apparatus, according to

$$\sigma = \sqrt{\frac{s^2}{N} + \frac{a^2}{12N} + \frac{8\pi s^4 b^2}{a^2 N^2}}$$

Here N is the number of photons observed by the detector (a CCD camera for our experiments), s is the standard deviation of the Gaussian fit to the dye molecule fluorescence, a is the

effective size of the pixel, and b is the standard deviation of background counts observed by the detector. The first term under the square root describes the photon noise, the second term is due to the finite pixel size of the detector, and the final term is the noise of the background. For large numbers of photons, the limiting term is the photon noise. Our fluorescence imaging falls into this regime. Our apparatus has an effective pixel size of 106.7 nm and a background standard deviation of approximately 5 photons per pixel. For these settings if 10,000 photons are collected, the photon noise term is a factor of six larger than the background noise and a factor of 70 larger than the pixel noise term.

In theory, the localization precision can be made arbitrarily small by collecting more photons at the detector. In practice, the precision is limited by the brightness and lifetime of organic dyes. After prolonged excitation with a laser, organic dyes will photobleach, undergoing irreversible chemical damage or covalent modification. This occurs primarily when a dye enters an excited triplet state in which it can react with chemicals in its environment. In order to be suitable for biological experiments, a dye must not only emit a sufficient number of photons but do so on a timescale appropriate for the measurement. The motility experiments performed for this dissertation used large (500 nm) fluorescent beads coated with many dyes and quantum dots, semiconductor nanocrystals that do not photobleach, so fluorescent lifetimes were not a concern as both of these probes remained very bright for the duration of all experiments.

Section 1.7: Total Internal Reflection Microscopy

The signal to background ratio must be very high for tracking single fluorescent particles. To achieve this, total internal reflection fluorescence microscopy (TIRF) is used. The TIRF technique was first used to study cell membranes by Daniel Axelrod in 1981 and used in vitro to study single myosin motors in 1995 by the Yanagida laboratory (64, 65). To accomplish TIRF,

the laser used to excite the fluorescent probes is angled such that it hits the glass-buffer interface at an angle greater than the critical angle for total internal reflection (Figure 1.11).

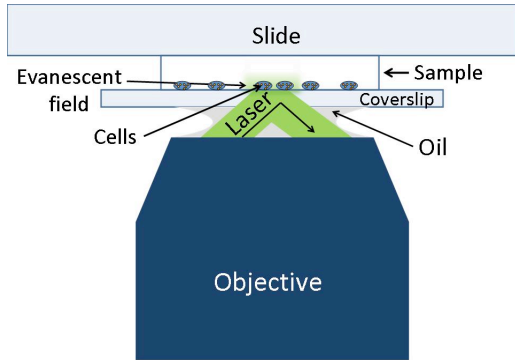


Figure 1.11: TIRF microscopy: When laser light hits the glass-water interface at an angle greater than the critical angle, the laser will be reflected. An evanescent wave will illuminate a thin section (~100nm) near the surface of the coverslip.

This creates an evanescent field that decays exponentially according to

$$I = I_0 e^{-z/d},$$

where I_0 is the incident intensity at the glass-buffer interface, z is the distance away from the interface and d is the penetration depth of the laser. The penetration depth, d , is given by

$$d = \frac{\lambda}{4\pi} (n_1^2 \sin^2 \theta - n_2^2)^{-1/2}.$$

In this expression, λ is the wavelength of the incident light (in a vacuum), n_1 is the index of refraction of the cover slip, n_2 is the index of refraction of the buffer solution, and θ is the angle of incidence. For the imaging conditions used in this work, TIRF microscopy was employed to create an evanescent field that penetrated the sample to a depth of approximately 100 nm. By only exciting the sample to a depth of 100 nm, we excited only the material close to the cover slip surface while excluding the volume above the surface, avoiding the background fluorescence of particles in solution far away from the cover slip surface.

Section 1.8: Optical Trapping

The forces generated by cytoskeletal motors are on the order of a few piconewtons. Optical traps, which exert forces in the piconewton regime, are well suited for probing the force of single kinesin molecules. By attaching micron-sized cargo to a kinesin motor, it is possible to optically trap the cargo and measure the force the motor can exert.

Optical traps use highly focused light to hold micron-sized particles in place. Arthur Ashkin and colleagues at Bell Laboratories developed the first optical trap in 1985, when they used focused light to trap polystyrene spheres (66). Since then, optical traps have been applied to a wide variety of systems, but have been particularly useful in measuring the biological forces of single molecules. In biology, optical traps have been used to measure forces associated with molecular motors, DNA, microtubules, and even entire cells (67-70).

Objects from tens of nanometers to tens of micrometers in diameter can be trapped. To create an optical trap, a lens is used to bring a beam of light to a sharp focus. If a spherical object with an index of refraction that is higher than that of the surrounding media is brought in the vicinity of the focus, it will experience a force that tends to pull it towards the focus. The large range of utility of optical tweezers makes it difficult to give a single theoretical explanation of optical trapping. If the object to be trapped is much larger than the wavelength of light used for trapping, a geometric, or ray, optics approach is valid and can be used to calculate the trapping force on the object (71). However, if the object is much smaller than the wavelength of light, the particle can be modeled as a tiny induced dipole in an oscillating electric field. The trapping force then results from the interaction of the electric field with this dipole (72). The question of how to explain the trapping force becomes substantially more complicated if the particle is approximately equal in size to the wavelength of incident light. In this situation, neither the ray

optics nor the dipole approximation is valid, but a generalized Lorenz-Mie approach must be used (73).

The trapping process in the ray optics regime is illustrated in Figure 1.12 for a sphere that is positioned slightly above the focus of the light rays, located where the orange lines cross in the figure. If the sphere has a greater index of refraction than the surrounding media, as is the case for polystyrene spheres in an aqueous buffer, which are commonly used to study motor proteins, the light rays will bend toward the normal as they enter the spheres. As the two light rays exit the sphere, they are bent away from the normal of the sphere according to Snell's law. The net change in momentum of the light will be in the up direction, so the conservation of momentum dictates that the sphere will experience a change in momentum in downward, and hence move towards the focus. Similarly, if the sphere is placed slightly below the focus, the net change in momentum for the light will be in the downward direction, so the sphere will experience a force that tends to pull it up into the focus.

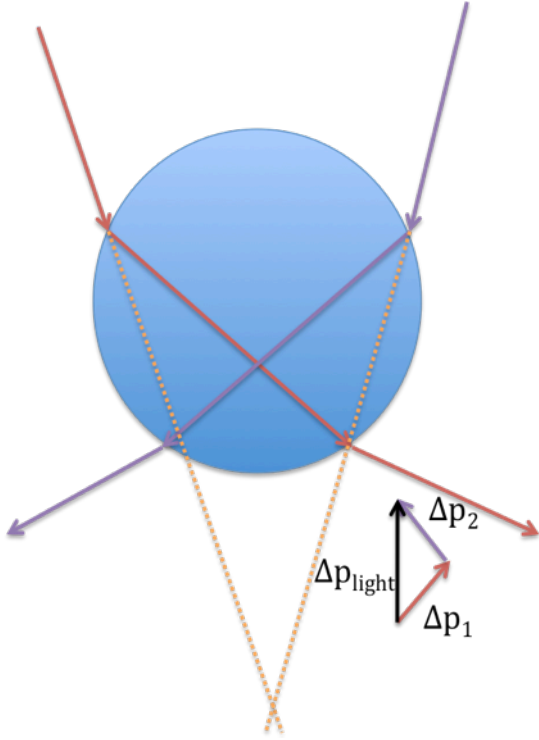


Figure 1.12: Illustration of the momentum change of focused light rays passing through a sphere. The refraction of the focused incident light rays is shown in purple and red while the dotted orange lines show the path the incident beams would take in the absence of the bead. The force diagram indicates that the net change in momentum of the light is upward, so the sphere will experience a downward force that will pull it to the focal point of the rays.

A particle much smaller than the wavelength of the incident light can be modeled as a dipole.

The expression for the force experienced by a small dipole, $\vec{p}(\vec{r}, t)$, in a non-constant electric

field, $\vec{E}(\vec{r}, t)$, is

$$F = (\alpha \vec{E}(\vec{r}, t) \cdot \nabla) \vec{E}(\vec{r}, t),$$

where the dipole moment of the sphere is assumed to be linearly related to the electric field

according to $\vec{p} = \alpha \vec{E}$. The vector identity,

$$\nabla E^2 = 2(\vec{E} \cdot \nabla) \vec{E} + 2\vec{E} \times (\nabla \times \vec{E}),$$

and the fact that the curl of an electric field is zero in electrostatics result in the simplification of

the expression for the electric force on the dipole

$$\vec{F}_{grad} = \frac{\alpha}{2} \nabla E^2 .$$

This force is directed towards where the electric field is strongest. If the trapping beam is Gaussian, the maximum electric field will be located at the focus and the particle will be trapped there.

Although the third situation in which the particle is approximately the same size as the incident wavelength is the regime we operate in for most molecular motor experiments (using 1064 nm light and 500-1000 nm motor-coated beads), the derivation of the generalized Lorenz-Mie approach to solve for trapping forces is substantially more complicated than trapping in the ray optics or electric dipole regimes and is not given here. A good description of the theory in this regime can be found in Mazolli et al. (73).

Section 1.9: Chemical Kinetics

As it walks along the microtubule tracks, kinesin hydrolyzes one ATP molecule for every step it takes. The hydrolysis and stepping of the motor domains are highly coordinated, allowing for long processive runs in which kinesin takes 100 or more steps before dissociating from its microtubule track. A defect in kinesin's ability to bind ATP or microtubules could impair kinesin and result in slower or less processive motion. Measuring the chemical kinetics of kinesin is one way to probe whether phosphorylation may affect kinesin's motility by interfering with ATP or microtubule binding. This is done by determining the rate constants of ATP hydrolysis.

Kinesin hydrolyzes ATP even in the absence of microtubules, but microtubules accelerate this process 1000-fold (74). In the presence of microtubules, kinesin's ATP hydrolysis and stepping are coupled (75, 76). Figure 1.13 depicts the cycle of microtubule-enhanced ATP hydrolysis. In the top panel (A), kinesin is in a state with ATP bound to the trailing head, while the leading

head is nucleotide free. Kinesin will hydrolyze the ATP of the trailing head to ADP, which remains bound to the head, and phosphate, which is released into solution (panel B). An ADP-bound head has a much lower affinity for microtubules than an ATP-bound head and will dissociate. The state shown in panel B is known as the “ATP waiting state”. In panel C, ATP binding to the leading head induces strain in the neck linker, which biases the rear head forward. Once the rear head releases ADP, it will bind to the microtubule in front of the original “leading head” (panel D) and the cycle can restart.

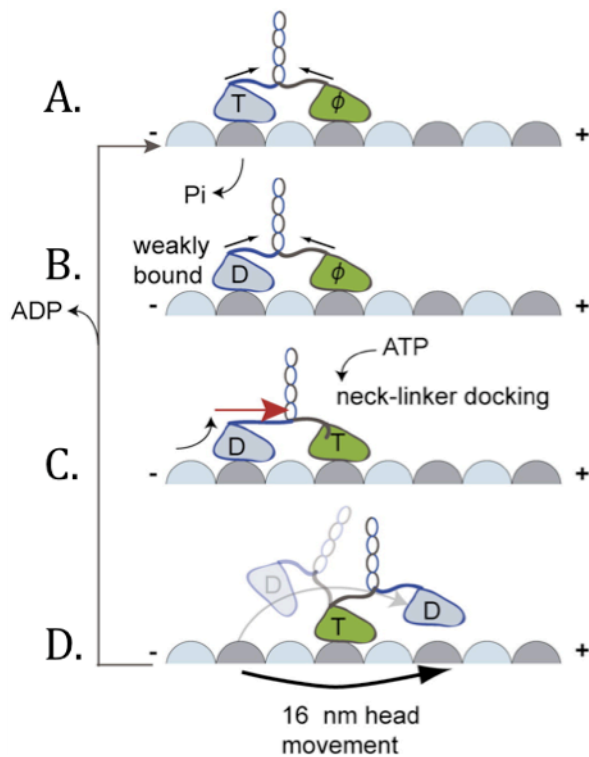


Figure 1.13: Coordination of ATP hydrolysis and kinesin stepping. Figure used with permission (modified) from Yildiz, et al. (73). T indicates an ATP-bound head, D indicates an ADP-bound head, and φ indicates a nucleotide-free head.

The ATP hydrolysis of kinesin follows Michaelis-Menten kinetics (74, 77). Michaelis-Menten kinetics model the rate of an enzymatic reaction in which an enzyme, E, acts on a single substrate, S, converting it into a product, P, according to



The rate constants in this process are commonly denoted as k_{on} for the combination of the enzyme and substrate, k_{off} for their separation and k_{cat} for the formation of product. It is assumed that the formation of the product is irreversible, but that enzyme substrate formation is reversible. For ATP hydrolysis by the kinesin enzyme, these assumptions are true. The hydrolysis of ATP into ADP and free phosphate releases 30.5 kJ/mol of energy, which makes the reverse process highly unfavorable. The rate equations for an enzymatic reaction are given by the law of mass action:

$$\begin{aligned}
 1. \frac{d[E]}{dt} &= -k_{on}[E][S] + (k_{off} + k_{cat})[ES] \\
 2. \frac{d[S]}{dt} &= -k_{on}[E][S] + k_{off}[ES] \\
 3. \frac{d[ES]}{dt} &= k_{on}[E][S] - (k_{off} + k_{cat})[ES] \\
 4. \frac{d[P]}{dt} &= k_{cat}[ES]
 \end{aligned}$$

To derive the Michaelis-Menten result for the rate of product formation, it is assumed that the enzyme-substrate complex, ES, is at a constant concentration. In most systems, this assumption is correct. Shortly after the reaction begins, ES reaches a steady state and its concentration does not change appreciably until large amounts of the substrate, S, have been reacted. Assuming ES is at a steady state, equation 3 above becomes

$$k_{on}[E][S] = (k_{off} + k_{cat})[ES].$$

The total enzyme concentration, $[E_T]$ is equal to the sum of the concentrations $[E]$ and $[ES]$, so

$$k_{on}([E_T] - [ES])[S] = (k_{off} + k_{cat})[ES].$$

Solving for $[ES]$,

$$[ES] = \frac{[E_T][S]}{\left(\frac{k_{off} + k_{cat}}{k_{on}}\right) + [S]}.$$

The rate of product formation is given by equation 4 of the rate equations. Substituting the above formula for [ES] into equation 4, yields

$$\frac{d[P]}{dt} = \frac{k_{cat}[E_T][S]}{\left(\frac{k_{off} + k_{cat}}{k_{on}}\right) + [S]}$$

The maximum possible rate of product formation occurs when [ES]=[E_T] and is v_{max}=k_{cat}[E_T].

Substituting this into the equation above and defining a Michaelis constant, K_m=(k_{off}+k_{cat}/k_{on}),

produces the Michaelis-Menten equation for enzyme kinematics:

$$v = \frac{d[P]}{dt} = \frac{v_{max}[S]}{K_m + [S]}$$

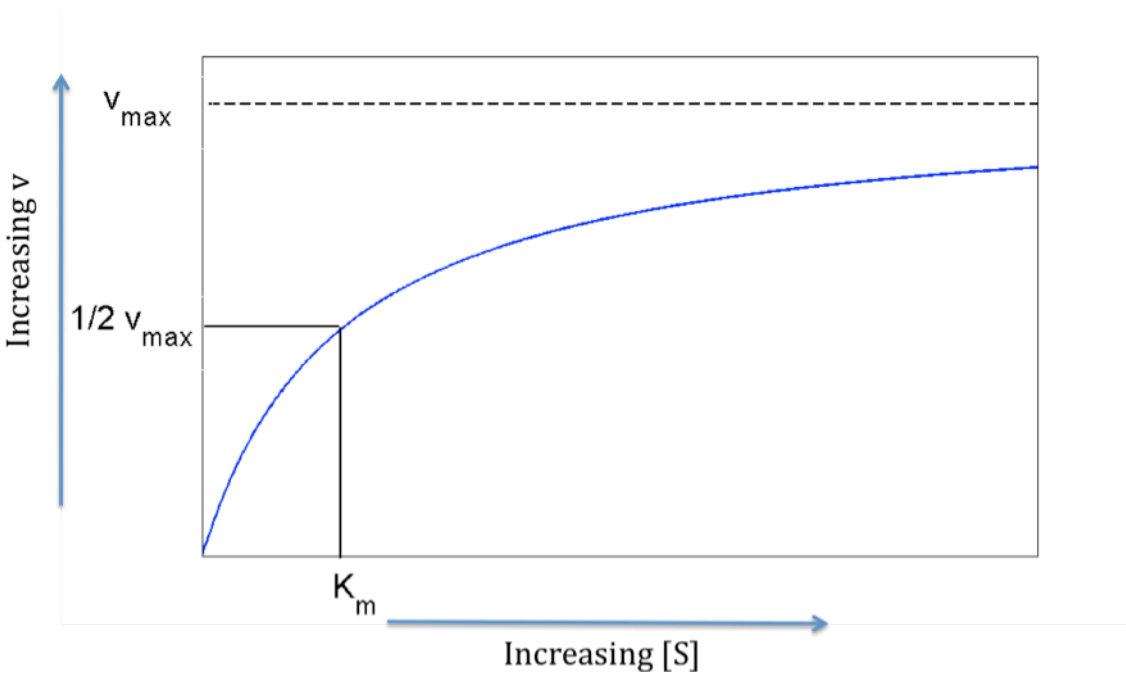


Figure 1.13: An example of a typical Michaelis-Menten curve. [S] is the substrate concentration in the reaction and v is the reaction rate.

For the hydrolysis of ATP by kinesin, P is ADP, S is ATP, and E is kinesin. Every time it takes a step, one molecule of ADP is released, so the reaction rate will be directly proportional to the velocity of kinesin so v and v_{max} in the Michaelis-Menten equation can be expressed as

velocities in nm/s. K_m is the concentration of substrate at which a reaction runs at half its maximum rate and measures the relative affinity of the enzyme for the substrate. The lower K_m is, the higher the affinity between the enzyme and substrate. For ATP hydrolysis, kinesin has a K_m of approximately 50 μ M. The microtubule dependence of kinesin's ATPase activity also follows Michaelis-Menten kinetics, making it possible to define a K_{mMT} that describes the relative affinity of kinesin for microtubules (78, 79). K_{mMT} will vary according to the amount of kinesin and ATP used in the reactions to determine it and is therefore most useful as a comparative measurement.

References

1. Moran, U., R. Phillips and R. Milo 2010. SnapShot: Key numbers in biology. *Cell*. 141, 1262-1262.e1.
2. Caviston, J. P. and E.L. Holzbaur 2006. Microtubule motors at the intersection of trafficking and transport. *Trends Cell Biol.* 16, 530-537.
3. Hirokawa, N., Y. Noda, Y. Tanaka and S. Niwa 2009. Kinesin superfamily motor proteins and intracellular transport. *Nat. Rev. Mol. Cell Biol.* 10, 682-696.
4. Dixit, R., J.L. Ross, Y.E. Goldman and E.L. Holzbaur 2008. Differential regulation of dynein and kinesin motor proteins by tau. *Science*. 319, 1086-1089.
5. Vershinin, M., J. Xu, D.S. Razafsky, S.J. King and S.P. Gross 2008. Tuning microtubule-based transport through filamentous MAPs: The problem of dynein. *Traffic*. 9, 882-892.
6. Hollenbeck, P. J. 1993. Phosphorylation of neuronal kinesin heavy and light chains in vivo. *J. Neurochem.* 60, 2265-2275.
7. Kardon, J. R. and R.D. Vale 2009. Regulators of the cytoplasmic dynein motor. *Nat. Rev. Mol. Cell Biol.* 10, 854-865.
8. Morfini, G., G. Szebenyi, R. Elluru, N. Ratner and S.T. Brady 2002. Glycogen synthase kinase 3 phosphorylates kinesin light chains and negatively regulates kinesin-based motility. *EMBO J.* 21, 281-293.
9. Sato-Yoshitake, R., H. Yorifuji, M. Inagaki and N. Hirokawa 1992. The phosphorylation of kinesin regulates its binding to synaptic vesicles. *J. Biol. Chem.* 267, 23930-23936.
10. Chevalier-Larsen, E. and E.L. Holzbaur 2006. Axonal transport and neurodegenerative disease. *Biochim. Biophys. Acta.* 1762, 1094-1108.

11. Hirokawa, N., S. Niwa and Y. Tanaka 2010. Molecular motors in neurons: Transport mechanisms and roles in brain function, development, and disease. *Neuron*. 68, 610-638.
12. Gunawardena, S., L.S. Her, R.G. Brusch, R.A. Laymon, I.R. Niesman, B. Gordesky-Gold, L. Sintasath, N.M. Bonini and L.S. Goldstein 2003. Disruption of axonal transport by loss of huntingtin or expression of pathogenic polyQ proteins in drosophila. *Neuron*. 40, 25-40.
13. Morfini, G., G. Pigino, G. Szebenyi, Y. You, S. Pollema and S.T. Brady 2006. JNK mediates pathogenic effects of polyglutamine-expanded androgen receptor on fast axonal transport. *Nat. Neurosci.* 9, 907-916.
14. Morfini, G. A., Y.M. You, S.L. Pollema, A. Kaminska, K. Liu, K. Yoshioka, B. Bjorkblom, E.T. Coffey, C. Bagnato, D. Han, C.F. Huang, G. Banker, G. Pigino and S.T. Brady 2009. Pathogenic huntingtin inhibits fast axonal transport by activating JNK3 and phosphorylating kinesin. *Nat. Neurosci.* 12, 864-871.
15. Piccioni, F., S. Simeoni, I. Andriola, E. Armatura, S. Bassanini, P. Pozzi and A. Poletti 2001. Polyglutamine tract expansion of the androgen receptor in a motoneuronal model of spinal and bulbar muscular atrophy. *Brain Res. Bull.* 56, 215-220.
16. Szebenyi, G., G.A. Morfini, A. Babcock, M. Gould, K. Selkoe, D.L. Stenoien, M. Young, P.W. Faber, M.E. MacDonald, M.J. McPhaul and S.T. Brady 2003. Neuropathogenic forms of huntingtin and androgen receptor inhibit fast axonal transport. *Neuron*. 40, 41-52.
17. Fennema-Notestine, C., S. Archibald, M. Jacobson, J. Corey-Bloom, J. Paulsen, G. Peavy, A. Gamst, J. Hamilton, D. Salmon and T. Jernigan 2004. In vivo evidence of cerebellar atrophy and cerebral white matter loss in huntington disease. *Neurology*. 63, 989.
18. La Spada, A. R., E.M. Wilson, D.B. Lubahn, A.E. Harding and K.H. Fischbeck 1991. Androgen receptor gene mutations in X-linked spinal and bulbar muscular atrophy. *Nature*. 352, 77-79.
19. Walker, F. O. 2007. Huntington's disease. *Lancet*. 369, 218-228.
20. La Spada, A. 1993. Spinal and bulbar muscular atrophy; In *GeneReviews*, Pagon, R. A., Bird, T. D., Dolan, C. R., Stephens, K. and Adam, M. P., editors. University of Washington, Seattle, Seattle (WA).
21. Harjes, P. and E.E. Wanker 2003. The hunt for huntingtin function: Interaction partners tell many different stories. *Trends Biochem. Sci.* 28, 425-433.
22. Mohit, A. A., J.H. Martin and C.A. Miller 1995. p493F12 kinase: A novel MAP kinase expressed in a subset of neurons in the human nervous system. *Neuron*. 14, 67-78.
23. Chretien, D., F. Metoz, F. Verde, E. Karsenti and R.H. Wade 1992. Lattice defects in microtubules: Protofilament numbers vary within individual microtubules. *J. Cell Biol.* 117, 1031-1040.
24. Pierson, G. B., P.R. Burton and R.H. Himes 1978. Alterations in number of protofilaments in microtubules assembled in vitro. *J. Cell Biol.* 76, 223-228.

25. Miki, H., Y. Okada and N. Hirokawa 2005. Analysis of the kinesin superfamily: Insights into structure and function. *Trends Cell Biol.* 15, 467-476.
26. Gyoeva, F. K., D.V. Sarkisov, A.L. Khodjakov and A.A. Minin 2004. The tetrameric molecule of conventional kinesin contains identical light chains. *Biochemistry.* 43, 13525-13531.
27. Vale, R. D. 2003. The molecular motor toolbox for intracellular transport. *Cell.* 112, 467-480.
28. Marx, A., J. Muller and E. Mandelkow 2005. The structure of microtubule motor proteins. *Adv. Protein Chem.* 71, 299-345.
29. Ray, S., E. Meyhöfer, R.A. Milligan and J. Howard 1993. Kinesin follows the microtubule's protofilament axis. *J. Cell Biol.* 121, 1083-1093.
30. Yildiz, A., M. Tomishige, R.D. Vale and P.R. Selvin 2004. Kinesin walks hand-over-hand. *Science.* 303, 676-678.
31. Schnitzer, M. J. and S.M. Block 1997. Kinesin hydrolyses one ATP per 8-nm step. *Nature.* 388, 386-390.
32. Furuta, K., A. Furuta, Y.Y. Toyoshima, M. Amino, K. Oiwa and H. Kojima 2013. Measuring collective transport by defined numbers of processive and nonprocessive kinesin motors. *Proc. Natl. Acad. Sci. U. S. A.* 110, 501-506.
33. Meyhöfer, E. and J. Howard 1995. The force generated by a single kinesin molecule against an elastic load. *Proceedings of the National Academy of Sciences.* 92, 574-578.
34. Svoboda, K. and S.M. Block 1994. Force and velocity measured for single kinesin molecules. *Cell.* 77, 773-784.
35. Carter, N. J. and R.A. Cross 2005. Mechanics of the kinesin step. *Nature.* 435, 308-312.
36. Kaan, H. Y., D.D. Hackney and F. Kozielski 2011. The structure of the kinesin-1 motor-tail complex reveals the mechanism of autoinhibition. *Science.* 333, 883-885.
37. Verhey, K. J. and J.W. Hammond 2009. Traffic control: Regulation of kinesin motors. *Nat. Rev. Mol. Cell Biol.* 10, 765-777.
38. Coy, D. L., W.O. Hancock, M. Wagenbach and J. Howard 1999. Kinesin's tail domain is an inhibitory regulator of the motor domain. *Nat. Cell Biol.* 1, 288-292.
39. Hackney, D. D. and M.F. Stock 2000. Kinesin's IAK tail domain inhibits initial microtubule-stimulated ADP release. *Nat. Cell Biol.* 2, 257-260.
40. Xia, C., A. Rahman, Z. Yang and L.S. Goldstein 1998. Chromosomal localization reveals three kinesin heavy chain genes in mouse. *Genomics.* 52, 209-213.
41. Encalada, S. E., L. Szpankowski, C.H. Xia and L.S. Goldstein 2011. Stable kinesin and dynein assemblies drive the axonal transport of mammalian prion protein vesicles. *Cell.* 144, 551-565.

42. Nakajima, K., X. Yin, Y. Takei, D.H. Seog, N. Homma and N. Hirokawa 2012. Molecular motor KIF5A is essential for GABA(A) receptor transport, and KIF5A deletion causes epilepsy. *Neuron*. 76, 945-961.
43. Wang, L. and A. Brown 2010. A hereditary spastic paraplegia mutation in kinesin-1A/KIF5A disrupts neurofilament transport. *Mol. Neurodegener.* 5, 52-1326-5-52.
44. Woehlke, G., A.K. Ruby, C.L. Hart, B. Ly, N. Hom-Booher and R.D. Vale 1997. Microtubule interaction site of the kinesin motor. *Cell*. 90, 207-216.
45. Li, M. and W. Zheng 2011. Probing the structural and energetic basis of kinesin-microtubule binding using computational alanine-scanning mutagenesis. *Biochemistry*. 50, 8645-8655.
46. UniProt Consortium 2012. Reorganizing the protein space at the universal protein resource (UniProt). *Nucleic Acids Res.* 40, D71-5.
47. Kozielski, F., S. Sack, A. Marx, M. Thormahlen, E. Schonbrunn, V. Biou, A. Thompson, E.M. Mandelkow and E. Mandelkow 1997. The crystal structure of dimeric kinesin and implications for microtubule-dependent motility. *Cell*. 91, 985-994.
48. Gibbons, I. R., J.E. Garbarino, C.E. Tan, S.L. Reck-Peterson, R.D. Vale and A.P. Carter 2005. The affinity of the dynein microtubule-binding domain is modulated by the conformation of its coiled-coil stalk. *J. Biol. Chem.* 280, 23960-23965.
49. Kon, T., K. Imamula, A.J. Roberts, R. Ohkura, P.J. Knight, I.R. Gibbons, S.A. Burgess and K. Sutoh 2009. Helix sliding in the stalk coiled coil of dynein couples ATPase and microtubule binding. *Nat. Struct. Mol. Biol.* 16, 325-333.
50. Redwine, W. B., R. Hernandez-Lopez, S. Zou, J. Huang, S.L. Reck-Peterson and A.E. Leschziner 2012. Structural basis for microtubule binding and release by dynein. *Science*. 337, 1532-1536.
51. Reck-Peterson, S. L., A. Yildiz, A.P. Carter, A. Gennerich, N. Zhang and R.D. Vale 2006. Single-molecule analysis of dynein processivity and stepping behavior. *Cell*. 126, 335-348.
52. Wang, Z., S. Khan and M.P. Sheetz 1995. Single cytoplasmic dynein molecule movements: Characterization and comparison with kinesin. *Biophys. J.* 69, 2011-2023.
53. Mallik, R., B.C. Carter, S.A. Lex, S.J. King and S.P. Gross 2004. Cytoplasmic dynein functions as a gear in response to load. *Nature*. 427, 649-652.
54. Ori-McKenney, K. M., J. Xu, S.P. Gross and R.B. Vallee 2010. A cytoplasmic dynein tail mutation impairs motor processivity. *Nat. Cell Biol.* 12, 1228-1234.
55. Gennerich, A., A.P. Carter, S.L. Reck-Peterson and R.D. Vale 2007. Force-induced bidirectional stepping of cytoplasmic dynein. *Cell*. 131, 952-965.
56. DeWitt, M. A., A.Y. Chang, P.A. Combs and A. Yildiz 2012. Cytoplasmic dynein moves through uncoordinated stepping of the AAA+ ring domains. *Science*. 335, 221-225.

57. Qiu, W., N.D. Derr, B.S. Goodman, E. Villa, D. Wu, W. Shih and S.L. Reck-Peterson 2012. Dynein achieves processive motion using both stochastic and coordinated stepping. *Nature Structural & Molecular Biology*. 19, 193-200.
58. Toba, S., T.M. Watanabe, L. Yamaguchi-Okimoto, Y.Y. Toyoshima and H. Higuchi 2006. Overlapping hand-over-hand mechanism of single molecular motility of cytoplasmic dynein. *Proceedings of the National Academy of Sciences*. 103, 5741-5745.
59. Walter, W. J., M.P. Koonce, B. Brenner and W. Steffen 2012. Two independent switches regulate cytoplasmic dynein's processivity and directionality. *Proc. Natl. Acad. Sci. U. S. A.* 109, 5289-5293.
60. Blehm, B. H., T.A. Schroer, K.M. Trybus, Y.R. Chemla and P.R. Selvin 2013. In vivo optical trapping indicates kinesin's stall force is reduced by dynein during intracellular transport. *Proceedings of the National Academy of Sciences*. 110, 3381-3386.
61. Yildiz, A., J.N. Forkey, S.A. McKinney, T. Ha, Y.E. Goldman and P.R. Selvin 2003. Myosin V walks hand-over-hand: Single fluorophore imaging with 1.5-nm localization. *Science*. 300, 2061-2065.
62. Toprak, E., C. Kural and P.R. Selvin 2010. Chapter one-super-accuracy and super-resolution: Getting around the diffraction limit. *Meth. Enzymol.* 475, 1-26.
63. Cheezum, M. K., W.F. Walker and W.H. Guilford 2001. Quantitative comparison of algorithms for tracking single fluorescent particles. *Biophys. J.* 81, 2378-2388.
64. Axelrod, D. 1981. Cell-substrate contacts illuminated by total internal reflection fluorescence. *J. Cell Biol.* 89, 141-145.
65. Funatsu, T., Y. Harada, M. Tokunaga, K. Saito and T. Yanagida 1995. Imaging of single fluorescent molecules and individual ATP turnovers by single myosin molecules in aqueous solution. *Nature*. 374, 555-559.
66. Ashkin, A., J.M. Dziedzic, J.E. Bjorkholm and S. Chu 1986. Observation of a single-beam gradient force optical trap for dielectric particles. *Opt. Lett.* 11, 288.
67. Block, S. M., L.S. Goldstein and B.J. Schnapp 1990. Bead movement by single kinesin molecules studied with optical tweezers. *Nature*. 348, 348-352.
68. Felgner, H., R. Frank and M. Schliwa 1996. Flexural rigidity of microtubules measured with the use of optical tweezers. *J. Cell. Sci.* 109 (Pt 2), 509-516.
69. Wang, M. D., H. Yin, R. Landick, J. Gelles and S.M. Block 1997. Stretching DNA with optical tweezers. *Biophys. J.* 72, 1335-1346.
70. Zhang, H. and K.K. Liu 2008. Optical tweezers for single cells. *J. R. Soc. Interface.* 5, 671-690.
71. Ashkin, A. 1992. Forces of a single-beam gradient laser trap on a dielectric sphere in the ray optics regime. *Biophys. J.* 61, 569-582.

72. Harada, Y. and T. Asakura 1996. Radiation forces on a dielectric sphere in the rayleigh scattering regime. *Opt. Commun.* 124, 529-541.
73. Mazolli, A., P.A.M. Neto and H.M. Nussenzveig 2003. Theory of trapping forces in optical tweezers. *Proceedings: Mathematical, Physical and Engineering Sciences.* 459, 3021-3041.
74. Kuznetsov, S. A. and V.I. Gelfand 1986. Bovine brain kinesin is a microtubule-activated ATPase. *Proc. Natl. Acad. Sci. U. S. A.* 83, 8530-8534.
75. Clancy, B. E., W.M. Behnke-Parks, J.O. Andreasson, S.S. Rosenfeld and S.M. Block 2011. A universal pathway for kinesin stepping. *Nat. Struct. Mol. Biol.* 18, 1020-1027.
76. Yildiz, A., M. Tomishige, A. Gennerich and R.D. Vale 2008. Intramolecular strain coordinates kinesin stepping behavior along microtubules. *Cell.* 134, 1030-1041.
77. Hackney, D. D. 1988. Kinesin ATPase: Rate-limiting ADP release. *Proc. Natl. Acad. Sci. U. S. A.* 85, 6314-6318.
78. Gilbert, S. P. and K.A. Johnson 1993. Expression, purification, and characterization of the drosophila kinesin motor domain produced in escherichia coli. *Biochemistry.* 32, 4677-4684.
79. Huang, T. G. and D.D. Hackney 1994. Drosophila kinesin minimal motor domain expressed in escherichia coli. purification and kinetic characterization. *J. Biol. Chem.* 269, 16493-16501.

Chapter 2: Materials and Methods

This chapter describes the preparation of reagents, protocols, and data analysis procedures used in experiments.

Section 2.1: Preparation of Motors and Their Tracks

2.1.1 Buffers

Various buffer solutions were used for the experiments. The formulations are listed below. The pH of all buffers was adjusted using KOH. Sodium inhibits kinesin, so it was important that NaOH was avoided when adjusting pH. EGTA did not go into solution until around a pH of 6, so pHing buffers carefully was crucial to getting all components to dissolve. In the buffer solutions we used, either PIPES (piperazine-N,N'-bis(2-ethanesulfonic acid)) or HEPES (4-(2-hydroxyethyl)-1-piperazineethanesulfonic acid) was the a buffering agent. Both have pKa values (pKa = 7.5 for HEPES and pKa = 6.8 for PIPES) near the typical physiological pH of 7.3 for mammalian cells, which made them useful buffering agents for biochemical reactions. EGTA (ethylene glycol tetraacetic acid) was used in all solutions to chelate calcium. Physiological concentrations of calcium are very low, and using EGTA to bind any calcium impurities in buffers mimicked the low physiological calcium levels and prevents unwanted interactions between calcium and the proteins in solution. Inside of cells, ATP is almost always found in complex with magnesium ions and Mg^{2+} is a required cofactor for many ATP hydrolysis reactions, including that of kinesin, so a magnesium salt was added to each buffer.

BRB-80

80mM PIPES

1mM EGTA

1mM $MgCl_2$

pH to 6.9 with KOH

Dynein Motility Buffer (DMB)

30mM HEPES

50mM KAcetate

2mM MgAcetate

1mM EGTA

pH to 7.2 with KOH

HEM

50mM HEPES

1mM EGTA

2mM MgSO₄

pH to 7.2 with KOH

2.1.2 Kinesin Constructs

Experiments were performed using kinesin protein of three different lengths (Fig 2.1). The longest was full-length kinesin that contained all 963 residues in the heavy chain and was purified by Carol Bookwalter in the laboratory of Kathleen Trybus at the University of Vermont. The second-longest construct was truncated to remove residues after 888, keeping only the first 888 residues of the kinesin heavy chain. Andrew Thompson in the Chris Berger laboratory at the University of Vermont purified this construct. An even shorter construct consisting of only residues 1-432 was purified by Marco Tjioe in the Selvin laboratory. Figure 2.1 illustrates the different kinesin constructs.

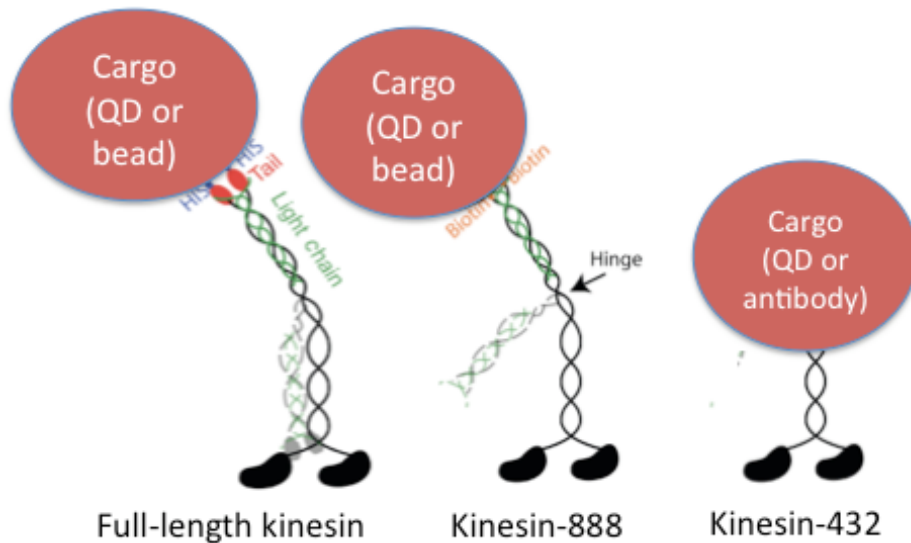


Figure 2.1: Illustration of kinesin constructs used in experiments. Adapted from (1).

The full-length and Kinesin-888 (K888) constructs were purified as described in the literature (1). Mouse kinesin-1B heavy chains and light chains were cloned into baculovirus vectors for expression in Sf9 cells. A hexahistidine tag was cloned to the N terminus of the heavy chain of the full-length heavy chain and a C-terminal biotin tag was added to the K888 heavy chains. Three different K888 heavy chain vectors were created. One in which the serine at residue 175 was mutated to an alanine residue (S175A), one in which the serine was mutated to aspartic acid (S175D) and one in which the original serine was left unmutated (WT). A C-terminal yellow fluorescent protein was added to the light chains. Sf9 cells were transfected with the baculovirus DNA coding for the heavy and light chains and recombinant baculovirus was purified. The recombinant virus was used to infect Sf9 cells and induce production of kinesin. Infected cells were lysed by sonication and centrifuged to separate the kinesin-enriched cytoplasm from other cell components. The supernatant of the centrifugation was applied to a His-Select nickel affinity column (Sigma-Aldrich) and washed with 30 mM imidazole to elute the his-tagged kinesin. The eluted kinesin fractions were concentrated and dialyzed against a buffer containing 10 mM HEPES, pH 7.3, 200 mM NaCl, 50% glycerol, 1 mM DTT, 10 μ M MgATP and 1 μ g/mL leupeptin and stored at -20 $^{\circ}$ C.

The truncated K432 was purified according to a protocol developed by Qiagen Inc. (2). A C-terminal his tag and a biotin tag were added to a copy of the human kinesin heavy chain gene that had been truncated to contain the first 432 residues and the entire gene was inserted into a pET21a vector. BL-21 (DE3) *E. coli* cells were transfected with the vector and plated on Luria Broth (LB) agar with ampicillin for selection. A single colony from a plate was used to inoculate 20 ml LB containing 100 µg/ml ampicillin and incubated at 37 °C overnight in a shaker at 200 rpm. The next day the overnight culture was diluted 1:50 into 1 L of LB containing ampicillin and grown at 37 °C in a shaker at 300 rpm until an OD600 of 0.6 was reached. At OD600 of 0.6, expression was induced by adding isopropyl β-D-1-thiogalactopyranoside (IPTG) to a final concentration of 0.25 mM. The cells were grown for another 4-5 hours and then harvested by centrifugation at 4000 g for 20 minutes at 4 °C. The cell pellets were frozen and stored overnight at -80 °C.

The next day, the pellets were thawed and purified using a Nickel-NTA resin (Qiagen, 30210) according to protocol 9 in the QiaExpressionist handbook (2). MgATP was added to all buffers to a final concentration of 40 µM. Eluted fractions enriched in protein were pooled and 10% sucrose was added as a cryoprotectant. Aliquots were flash frozen in liquid nitrogen and stored at -80 °C.

2.1.3 Dynein

Dynein protein was prepared by the laboratory of Trina Schroer at Johns Hopkins University (3). It was extracted from native bovine brain tissue. To summarize the protocol briefly, bovine brains were homogenized and centrifuged at 230,000 g to separate the cytoplasmic fraction, which contains dynein, from membranous components of the tissue. The supernatant of the

centrifugation was flowed over an SP sepharose column (GE) to separate dynein from other cytoplasmic components based on charge (see section 2.2.3 for a discussion of ion exchange chromatography). The protein-enriched fractions from the SP sepharose column were then added to 20-60% sucrose gradients and centrifuged. In a sucrose gradient, proteins in the dynein-enriched fraction traveled through the gradient until they reached a point of equal density with the gradient. The centrifuged gradient was fractionated to separate the components in it based on density. Fractions enriched in dynein were run over a Mono Q column. (GE) The equilibration buffer consisted of 35 mM Tris, 5 mM MgSO₄, pH 7.2 and KCl was added to elute the protein. After elution, 0.5 mM ATP and 1.0 mM DTT were added to dynein-enriched fractions. These fractions were mixed in a 1:1 ratio with a buffer containing 2.5 M sucrose, 35 mM Tris, 5 mM MgSO₄, pH 7.2 and flash frozen for storage at -80 °C.

2.1.4 Microtubules

For fluorescence experiments, unmodified bovine brain tubulin (Cytoskeleton, HTS02), biotinylated porcine brain tubulin (Cytoskeleton, T333P) and fluorescent, HiLyte tubulin (Cytoskeleton, TL488M) were polymerized in a 25:5:1 ratio in BRB-80 containing 1 mM DTT, 1 mM GTP, and 25% glycerol and a final tubulin concentration of 3.1 mg/ml. For microtubule activated ATPase assay experiments, the biotinylated tubulin and fluorescent tubulin were omitted. The reagents were mixed on ice and then incubated at 37°C for 30 minutes to induce polymerization. After polymerization, the sample was diluted with a 4X volume of taxol solution consisting of room temperature 1 mM GTP and 20 µM taxol in BRB-80. Taxol binds to and stabilizes microtubules by inhibiting depolymerization. To remove unpolymerized tubulin monomers, the mixture was centrifuged at 15,000 g for 30 minutes at 24 °C. The supernatant was discarded and the pellet of tubulin polymers was gently resuspended in the desired concentration of taxol solution.

2.1.5 Axonemes

Axonemes were prepared according to a protocol adapted from Gibbons and Fonk by Pierce and Vale (4, 5). Sea urchins were obtained from the Pt. Loma Marine Invertebrate Lab. Twenty sea urchins were ordered with the expectation that ten would be male. The protocol below was followed to obtain axonemes from the sea urchins.

1. Inject live sea urchins (*S. purpuratus*) with a few ml of 0.5 M KCl. The exterior of the sea urchins is hard and cannot be penetrated with a syringe, except near the mouth opening. Set them on Styrofoam cups at 4°C so that semen or eggs will drip into the cup. Female sea urchins will produce orange-colored eggs. These are to be discarded. The white-colored semen from male urchins should be collected.
2. Collect the semen and dilute 3-fold with seawater (or Instant Ocean, sold at aquarium stores) at 20 °C. Rinsing remaining semen off the urchins may increase the yield. All solutions should be maintained at 4°C for this step and the remainder of the preparation.
3. Centrifuge at 2000 g for 5 min to pellet sperm.
4. Resuspend by douncing the pellet in the same volume of buffer 1 (5 mM imidazole : Cl⁻, pH 7.0, 100 mM NaCl, 4 mM MgSO₄, 1 mM CaCl₂, 0.1 mM EDTA, 0.1 mM ATP, 7 mM BME) with 1% Triton X-100. Five or six passes of the douncing rod should be sufficient to resuspend the pellet in each step. Excessive douncing will shear the axonemes, resulting in shorter than desirable structures. Centrifuge at 1500g for 5 min to pellet sperm heads. Centrifuge the supernatant at 12,000g for 5 min.
5. Repeat step 4.
6. Resuspend the pellet by gently douncing in buffer 1. Centrifuge at 12,000g for 5 min. Repeat.
7. Resuspend the pellet by gently douncing in buffer 2 (5 mM imidazole:Cl⁻, pH 7.0, 600 mM NaCl, 4 mM MgSO₄, 1 mM CaCl₂, 0.1 mM EDTA, 7 mM BME, 1 mM DTT). Incubate for 10 min, then centrifuge at 12,000g for 5 min.

8. Repeat step 7, but add 1% Triton X-100 to buffer 2 and raise the pH to 8.0.
9. Repeat step 6 with one additional resuspension and centrifugation (total of three spins).
10. Resuspend pellet in one-fifth volume of buffer 1 containing 50% v/v glycerol. Store at -20 °C.

Ideally, 20-30 mm long axonemes will be achieved.

These steps produced a final volume of approximately 10 ml of axonemes at a concentration twenty or thirty times higher concentration than was used for experiments. The axonemes were stored in liquid nitrogen for long-term storage or at -20 °C for use within a year.

Section 2.2: JNK3 Mediated Phosphorylation of Kinesin

2.2.1 Phosphorylation

To phosphorylate kinesin at S175, purified JNK3 enzyme was purchased from Millipore (JNK3/SAPK1b, 14-501). The concentrated enzyme was diluted to a concentration of 0.1 mg/ml in a buffer containing 50 mM Tris/HCl, pH 7.5, 150 mM NaCl, 0.1 mM EGTA, 270 mM sucrose and 0.1% 2-mercaptoethanol. Aliquots were flash frozen in 1ml volumes in liquid nitrogen and stored at -80 °C. Phosphorylation was performed following a protocol based on that of Morfini (6). A basic reaction mixture is listed below which could be scaled up as necessary to produce more phosphorylated protein. We found that the activity of the kinase could differ significantly from lot to lot. The reaction as outlined here produced 80% phosphorylated protein with one lot of kinase, but only 30% phosphorylated with a different lot. The concentrations and volumes below was a good starting point, but amount of kinase that should be added to the reaction to produce good phosphorylation had to be optimized for each lot.

1. On ice mix:

2 ml of approximately 20 μ M kinesin

1 ml of 7 mM ATP
0.5 ml of JNK-3 diluted to 0.1 mg/ml
3.5 ul HEM buffer

2. Incubate the mixture at 37 °C for 30 minutes
3. Add 50% sucrose in HEM to the mixture for a final concentration of 10%v/v
4. Flash freeze and store at -80 °C

2.2.2 Radiolabeling Assay to Quantify Phosphorylation

To quantify phosphorylation, a radiolabeling assay was used. All radiolabeling assays were performed in the lab of Yi Lu at UIUC behind plexiglass shielding. In the Lu lab, reactions were run in collaboration with Seyed F. Torabi. Alongside the standard phosphorylation protocol outlined above, a second reaction was run which also contained 0.25 ml of [γ - ^{32}P] ATP (Perkin-Elmer) at a stock concentration of 1.67 mM. This ATP contains a radioactive phosphate at the γ -position that JNK3 transfers to S175 of kinesin during the phosphorylation reaction.

To measure the percentage of phosphorylated kinesin, an SDS-PAGE (Sodium dodecyl sulfate-PolyAcrylamide Gel Electrophoresis) gel was run. SDS-PAGE was run by first mixing a protein sample with a loading buffer which contains SDS. SDS is a detergent that denatures protein and coats it with a negative charge (Figure 2.2 A). The SDS-protein mixture was loaded into a polyacrylamide gel matrix and an electric field was applied. Smaller proteins moved through the matrix faster, allowing different protein species in a mixture to be separated based on length (Figure 2.2 B).

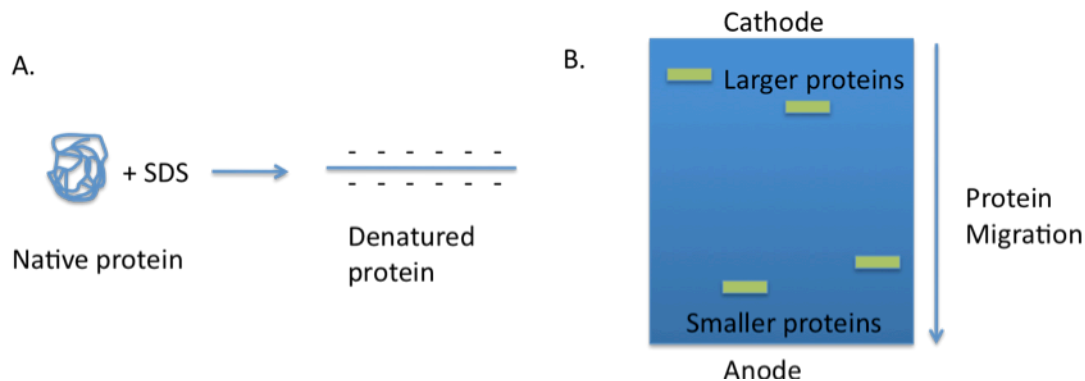


Figure 2.2: SDS-PAGE. A. Native protein is denatured and coated with negative charges. B. Protein is run through a gel. Small proteins encounter less resistance as they move through the gel matrix and migrate farther into the gel than larger proteins.

For the radiolabeling assay, the phosphorylation assay mix was run through a gel at 200 V for 20 minutes to separate the kinesin from free, excess [$g\text{-}^{32}\text{P}$] ATP and JNK-3. After this initial run, ATP standards were added to the gel. The standards were diluted such that the 100% standard would contain as much radioactive phosphate as kinesin that was 100% phosphorylated, the 50% standard would contain as much ^{32}P as 50% phosphorylated kinesin, and so on. ATP migrates very quickly through the gel due to its small size in comparison to kinesin (kinesin heavy chains are 120 kDa, each, and ATP is only 0.5 kDa). To visualize ATP standards alongside the kinesin, the standards were added to the gel after the initial 20-minute run and allowed to enter the gel during a second run of 5 minutes at 200 V.

The gel was exposed on a phosphorimager plate overnight and the resulting images were scanned. The intensity of the kinesin and ATP standard bands were measured and compared to determine the efficiency of phosphorylation.

2.2.3 Ion-Exchange Chromatography

Although ultimately unsuccessful, as an alternative to radiolabeling, an attempt was made to separate phosphorylated from unphosphorylated kinesin using anion-exchange chromatography. Ion-exchange chromatography separates components in a mixture according to charge. In anion exchange chromatography, a sample is flowed through a column bed containing a positively charged resin. Negatively charged species will bind to the resin. A buffer gradient of increasing salt concentration is then flowed through the column and highly charged species will elute from the column at higher salt concentrations than species with less charge. Phosphorylation adds a charge of approximately $-2e$ to a kinesin monomer in a solution at neutral pH. If successful, chromatography would have two advantages over radiolabeling. First, it does not involve the use of radioactive material and therefore avoids safety concerns associated with this. Second, if chromatography could separate the phosphorylated and unphosphorylated species, it would produce a sample with 100% phosphorylation. To be successful, differently charged species must elute from the column at distinct salt points, but only one broad elution peak of kinesin was ever observed for a variety of buffer and gradient conditions.

Initially, an attempt was made to separate phosphorylated and unphosphorylated protein using a HiTrap Q HP 1ml column (GE, 17-1153-01). The column was equilibrated with HEM buffer containing 2 mM DTT and 0.1 mM ATP. The elution buffer was identical to that used for equilibration, but with the addition of 1 M KCl. JNK3 treated kinesin was added to the column and the unbound sample was washed out with 5ml of equilibration buffer. A linear gradient from 0 to 1M KCl extending over 20 ml was applied at a flow rate of 3 ml/min. A single kinesin peak eluted at around 300 mM salt. The result of a single peak instead of a multiple peak indicated that the FPLC purification protocol was not sensitive enough to separate phosphorylated from unphosphorylated protein based on charge.

The protocol described above was iterated in an attempt to isolate phosphorylated protein. The attempted changes are listed below. None of the attempts led to a separation of phosphorylated and unphosphorylated protein.

1. HEM was replaced with BRB-80 to evaluate the effect of buffer conditions.
2. A shallower gradient from 0 to 500 mM over 20 ml was tested to evaluate whether multiple peaks would separate when the salt concentration was increased more gradually.
3. A Hi-Trap ANX-FF 1ml column (GE, 17-5162-01) was used in place of the Hi-Trap Q HP column to test whether a weaker anion exchange material would separate phosphorylated from unphosphorylated species.
4. A Resource-Q 1ml column (GE, 17-1177-01) was used in place of the Hi-Trap Q HP column to test whether an anion exchange material with higher resolving power would separate phosphorylated from unphosphorylated protein.

Section 2.3: Biochemical Assays

2.3.1 Motor Concentration Measurement

A Bradford assay was used to measure protein concentration. It is a colorimetric assay based on an absorbance shift in Coomassie Blue dye in acidic solution upon the addition of protein (7). In the absence of protein, Coomassie dye has an absorbance maximum at 365nm and is a reddish-brown color. Upon addition of protein, the absorbance maximum shifts to 595nm and the dye turns blue. This shift is only observed in an acidic solution. Commercial formulations of the Bradford assay reagent contain a mixture of Coomassie dye and phosphoric acid.

To measure protein concentration, 10 μ l of a protein sample was diluted into 50 μ l of Coomassie Plus (Bradford) Protein Assay (Thermo Scientific) solution in a glass test tube and left to

incubate at room temperature for 5 min. After 5 min, the mixture was transferred to a cuvette and the absorbance at 595 was measured using a UV/Vis spectrometer (BioRad). The protein concentration was measured by comparing the absorbance at 595nm to a standard curve of known concentrations of bovine serum albumin (Figure 2.3). The reactivity of the Bradford solution changes slowly over time, so a new standard curve was created monthly.

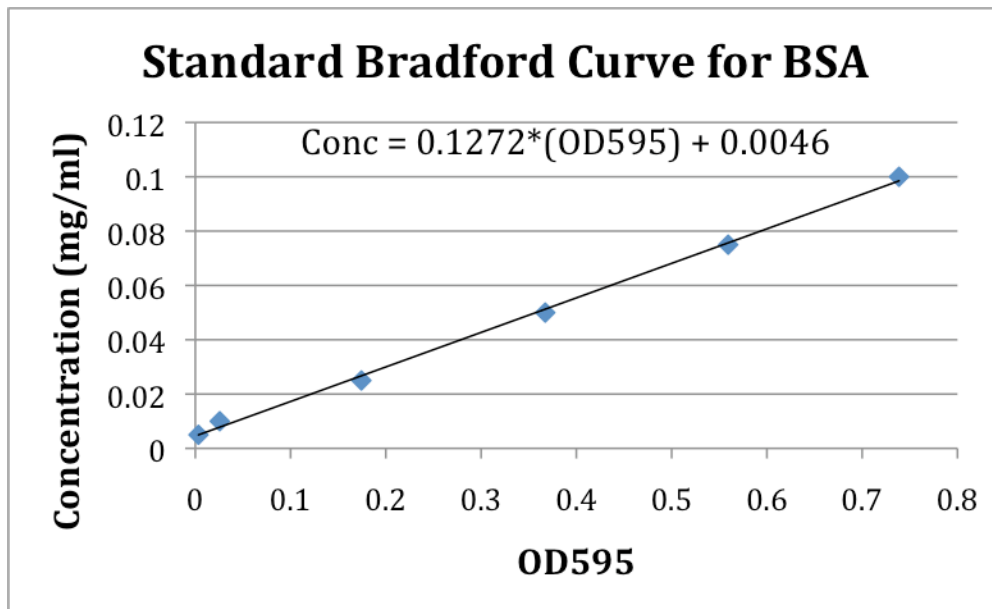


Figure 2.3: Standard Bradford assay curve created using known concentrations of bovine serum albumin (BSA) protein.

2.3.2 Single-Molecule ATPase Assay

To measure the ATPase activity of kinesin, the velocity of quantum-dot labeled kinesin was measured at different ATP concentrations. The rate of ATP hydrolysis by kinesin follows Michaelis–Menten kinetics. At a given ATP concentration, [ATP], the velocity, v , of kinesin will follow

$$v = \frac{v_{\max} [ATP]}{K_m + [ATP]}$$

Here, the maximum velocity at saturating levels of ATP is v_{\max} and K_m , the Michaelis constant, describes the affinity of kinesin for ATP.

To measure velocity as a function of ATP concentration, axoneme tracks were first stuck to cover glass in a flow chamber and motors were allowed to walk on these. Flow chambers were prepared by attaching two pieces of double-sided tape to a glass slide with a separation of approximately 0.5 cm. A glass coverslip was placed on top of the tape and excess tape was trimmed away with a razor blade. This created a narrow capillary chamber with a volume of 10-20 μ l.

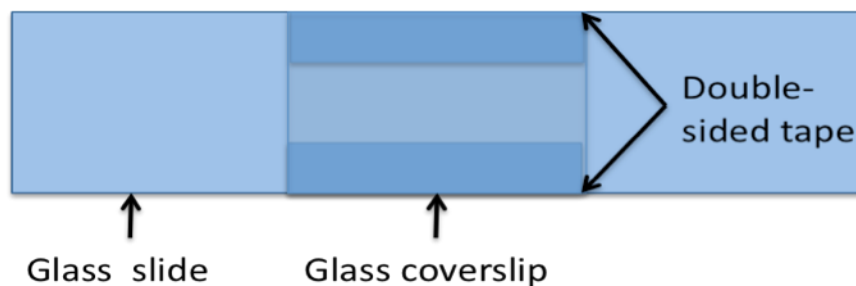


Figure 2.4: Diagram of a flow-chamber

Reagents were flowed into the chamber according to the following protocol.

Axoneme Preparation

1. Dilute axonemes 1:30 in BRB-80 buffer. Flow the dilution into the chamber.
2. Incubate the axoneme-containing chamber for at least 20 minutes at 4°C. Wrap in foil to protect the chamber.
3. Wash the chamber with DMB containing 8 mg/ml of BSA (DMB-BSA) and 1 mg/ml casein for blocking and incubate for 10 minutes at 4°C.

Motor Preparation

1. While the axonemes are incubating, dilute kinesin to 0.8 μM in BRB-80 containing 10 mg/ml of BSA and 10 mM DTT
2. Mix 0.5 μl of the diluted kinesin with 0.5 μl of 2 μM 655-streptavidin coated quantum dots (Invitrogen, Q10021MP) and incubate at 4°C for 30 minutes.
3. Dilute the kinesin and quantum dot mixture 1:5 into 100 μM biotin in BRB-80 and incubate for 10 minutes on ice.
4. Prepare an imaging buffer. To a base of DMB-BSA, add 1 mg/ml PCA (3,4-Dihydroxybenzoic acid, Fluka, 37580), 100 nM PCD (Protocatechuate 3,4-Dioxygenase, Sigma, P8279), 2 mM creatine phosphate, 5 U/ml creatine kinase, 10 mM DTT and varying ATP concentrations from 10 μM to 1 mM
5. Dilute the quantum-dot kinesin mixture 1 to 100 into the imaging buffer and flow into the casein-blocked axoneme chamber from step 3 of the axoneme preparation.

Images were recorded for no more than 15 minutes following the introduction of kinesin into the imaging buffer to ensure the optimal functioning of the creatine kinase-creatine phosphate ATP regeneration system. Images were taken on inverted Olympus Ixon 70 microscope with a 100X 1.45 numerical aperture objective (PlanApo 100X 1.45 NA $\infty/0.17$) plus an extra 1.5 X magnification sliding lens, for 150X total magnification. A 488 nm argon-ion (Melles Griot, 60mW, 543-AP-01) was used to excite the quantum dots and an Andor iXon EM + (DV-897E-CS0) CCD camera was used to record images. ATP concentrations over 100 μM were recorded with a 50 ms frame exposure and those at less than 100 μM were recorded at with 100 ms exposures.

Individual, motile quantum dots were tracked using an IDL FIONA program and velocities were extracted using Matlab code. For each ATP concentration, the velocities of at least 40 quantum dots were averaged. K_m and v_{max} were extracted using enzkin, a nonlinear fitting program for

enzyme kinematics in Matlab (enzkin.m by Giuseppe Cardillo,
<http://www.mathworks.com/matlabcentral/fileexchange/26653>)

2.3.3 Microtubule Activated ATPase Assay

A microtubule-activated ATPase assay was used to measure the affinity of kinesin for microtubules. For these experiments, microtubules consisting of native tubulin only were polymerized in BRB-80, as described previously. Tubulin was freshly polymerized immediately prior to each microtubule-activated assay experiment. The concentration of microtubules was measured by recording the absorbance at 280 nm of microtubules diluted in 6 M guanidine hydrochloride. The 6 M guanidine hydrochloride breaks up the microtubules into tubulin monomers and denatures the tubulin. The extinction coefficient, ϵ , of denatured tubulin at 280 nm is $115,000 \text{ M}^{-1}\text{cm}^{-1}$. Beer's law gives the relationship between the extinction coefficient, the tubulin concentration, c , the absorption path length, l , and the absorbance, A :

$$A = \epsilon cl.$$

ATPase activity was assayed using an ATPase Kinetic ELIPA Assay Kit (Cytoskeleton, BK051). This enzyme linked assay works based on the protocol developed by Webb (8). Free inorganic phosphate is released when kinesin catalyzes ATP. The assay mix contains another enzyme, purine nucleotide phosphorylase (PNP), which catalyzes the reaction of 2-amino-6-mercapto-7-methylpurine ribonucleoside (MESG) and inorganic phosphate into 2-amino-6-mercapto-7-methyl purine. This conversion is accompanied by a shift in the absorbance from 330 nm to 360 nm.

The following protocol was repeated for each assay point.

1. Mix fresh ELIPA assay buffer (EAB), consisting of 100 ml of the ELIPA reaction buffer with 20 μM taxol, 24 μl Reagent 1 (MESG), and 1.2 ml of 100U/ml Reagent 2 (PNP).

2. Combine EAB with 50 nM kinesin, 0.5 mM ATP and vary the microtubule concentration between 0.1 and 8 mM microtubules, depending on the assay point. Add the ATP last as this starts the reaction.
3. Immediately transfer the mixture to a cuvette and record the 360 nm absorbance at 3-second intervals for 5 minutes.

It should be noted that MESG degrades quickly at room temperature and is only good for approximately 30 minutes after having been thawed, so these steps should be performed quickly. Also, the reaction begins as soon as the ATP is thawed, so it is important to minimize the delay between steps 2 and 3 as much as possible.

To measure the rate of phosphate release, a straight line was fit to the initial, linear section of the rate of change of 360 nm absorption to form an ATPase activity curve for a given assay point. A standard phosphate curve was used to convert the absorbance into number of moles of inorganic phosphate released. This standard curve was created by adding known concentrations of a phosphate standard (KH_2PO_4) to EAB. To calculate the $K_{m\text{MT}}$ and v_{maxMT} , for microtubule activation, the ATPase activity in units of moles of phosphate hydrolyzed per kinesin head per second were plotted as a function of the microtubule concentration. The resulting data followed Michaelis-Menten kinetics, agreeing with results in the literature (9, 10). A non-linear Michaelis-Menten fit was performed using the same enzkin matlab code as was used for the single-molecule ATPase assay (enzkin.m by Giuseppe Cardillo, <http://www.mathworks.com/matlabcentral/fileexchange/26653>).

Section 2.4: TIRF Motility Assay of Kinesin and Dynein

2.4.1 Axoneme Purification of Kinesin

For an accurate comparison of two different kinesin protein samples, it was crucial that measurements of the two different samples had identical activity and concentration. Immediately prior to every fluorescence measurement an axonemal purification was performed. The purification removed two undesirably protein fractions. It eliminated both kinesin that did not bind to microtubules and kinesin that bound, but did not walk. The purification was performed by diluting 2 ml of concentrated kinesin stock (6-20 μM) in 30 ml BRB-80 containing 20 mM DTT. 10 μl purified axonemes were added and 3 ml of 50 mM adenosine 5'-(β,γ -imido)triphosphate (AMP-PNP, Roche, 10102547001) were added to the mixture and it was allowed to incubate on ice for ten minutes. AMP-PNP is an ATP analog that is only slowly hydrolyzed by kinesin, effectively trapping it in a microtubule-bound state (Figure 2.5).

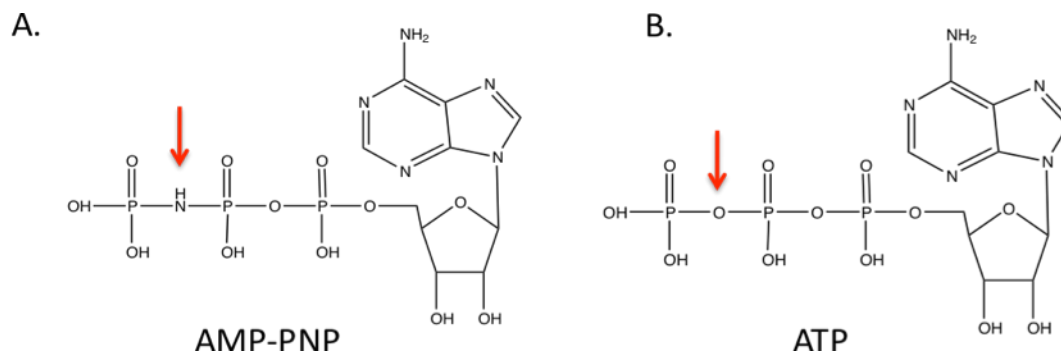


Figure 2.5: Chemical formulas of A. AMP-PNP and B. ATP. The red arrows indicate the position at which kinesin will cleave ATP. The presence of a nitrogen at this position in AMP-PNP inhibits cleavage.

The axonemes were then centrifuged at 14,000 rpm at 4°C for 30 minutes. The centrifugation pelleted motors that successfully bound to the axonemes and were trapped by AMP-PNP. Dead motors that never bound to the axonemes remained in the supernatant, which was discarded. The pellet was visible as a fine, almost transparent layer on the bottom of tube used for centrifugation.

To release the active motors, the pellet was resuspended in an excess of ATP. 40 μ l BRB-80 containing 20 mM DTT and 8 mM ATP was added to the tube containing the pellet and the mixture was gently pipetted up and down several times to break up the pellet. 8mM ATP was far in excess of what would be saturating for the amount of kinesin in the mixture. As a result the kinesin motors began to hydrolyze ATP and in the process, some dissociated from the axonemes. The mixture was incubated on ice for 10 minutes and then spun in the centrifuge a second time at 14,000 rpm at 4 °C for 30 minutes. Any dead, stuck motors that were unable to hydrolyze ATP remained attached to axonemes and were pelleted along with them. The supernatant contained only motors that successfully hydrolyzed ATP. The concentration of the supernatant was measured using a Bradford assay and the supernatant was then diluted to an appropriate concentration for subsequent steps.

2.4.2. Attachment of Motors to Cargo

Motors were non-specifically attached to carboxylated beads according to a protocol developed by Melinda Hoffman-Tonks. 500-nm red carboxylated microspheres (beads) were diluted 2:3 into DMB containing 8mg/ml of BSA (DMB-BSA) and briefly sonicated in an ice bath to dissociate any large aggregates of beads. Kinesin and dynein were diluted to the desired concentrations and were mixed with the beads in a ratio of 1:1:1. For experiments involving the K888 mutants, dynein was added at a concentration of 500 nM and kinesin at 10 nM prior to incubation with beads and for experiments involving full-length kinesin, dynein was added at a concentration of 167 nM and kinesin was diluted to 32 nM. The bead and motor mixture was incubated at 4°C for 30 minutes prior to imaging.

To measure the polarity of microtubules, a reference kinesin, K432 was used. This was coupled to a fluorescent antibody as cargo (Figure 2.6B). 1ul of 4.4 mM K432 with a C-terminal His tag was mixed with 1 ml of Alexa-647 labeled anti-his (Qiagen, 126244141). This mixture was

covered with foil to prevent photobleaching of the dye and incubated on ice for 30 minutes.

Figure 2.6 depicts the motor-coated beads and labeled reference kinesin.

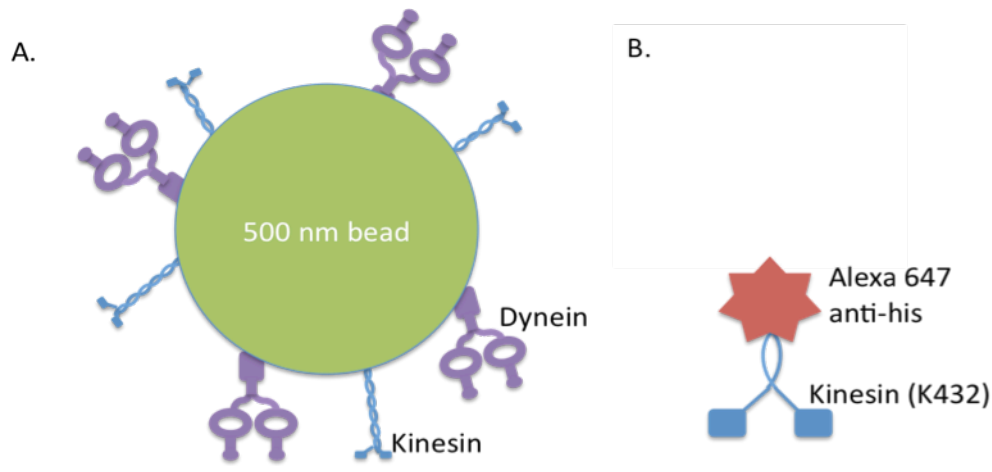


Figure 2.6: A. Fluorescent bead sample. B. Reference K432 sample

A flow chamber was prepared according to the following instructions.

1. Dilute BSA-biotin to 1 mg/ml in BRB-80 and flow into the chamber. Incubate at room temperature for 5 minutes. This step both functionalizes the glass with biotin and provides a coating of BSA to minimize non-specific interactions between the motors and glass surface.
2. Flush the chamber with BRB-80 to remove excess BSA-biotin.
3. Dilute neutravidin to 0.5 mg/ml in BRB-80 and flow into the chamber. Neutravidin has four biotin-binding sites and is thus able to link biotinylated microtubules to the biotinylated glass chamber. The neutravidin solution was incubated for 5 minutes at room temperature.
4. Flush excess, unbound neutravidin with BRB-80.
5. Dilute biotinylated, fluorescent microtubules were diluted to a final tubulin concentration of 50-100 nM in BRB-80 containing 20 μ M taxol and flow into the chamber. Incubate for ten minutes at room temperature.

6. Check the microtubules at a microscope to ensure that they are at an appropriate density of a few per field of view and are firmly bound to the glass surface.
7. Flush the chamber with BRB-80 plus 20 μM taxol.
8. Prepare an imaging buffer consisting of DMB-BSA, 20 mM DTT, 4 mM ATP, 1 mg/ml PCA, 100 nM PCD, and 20 μM taxol.
10. Add the reference kinesin to the imaging buffer to a final concentration of 3 nM.
11. Dilute the motor and bead mixture 1:50 into the imaging buffer.
12. Briefly sonicate the mixture in a water bath sonicator chilled with ice to break up any clusters of beads. Dip the imaging buffer tube into the mixer for a 1-2 seconds and repeat 5 or 6 times.
13. Flow the imaging buffer with beads and reference kinesin into the flow chamber. An illustration of the inside of an experimental chamber is shown in figure 2.7.

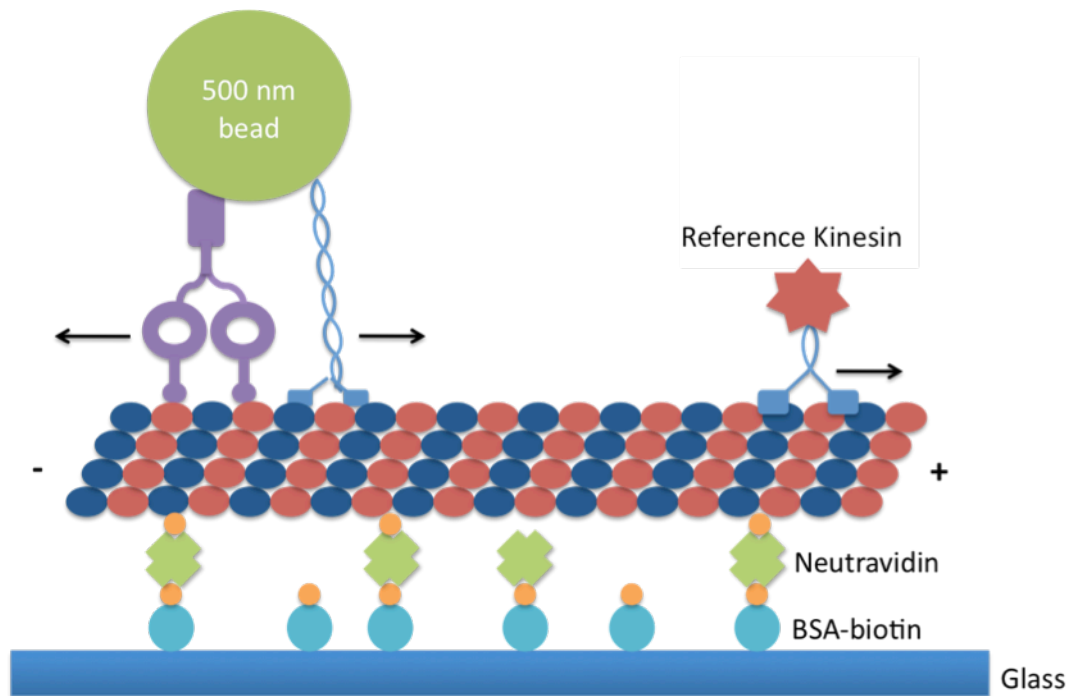


Figure 2.7: Illustration of the two-motor experiment inside a glass chamber. Biotin-neutravidin linkages stick microtubules to the glass surface. Reference kinesin move toward the plus-end of the microtubule. Beads coated with both kinesin and dynein can move in either direction.

2.4.3 Imaging

Images were acquired on an inverted Olympus Ixon 70 microscope with a 100X 1.45 numerical aperture objective (PlanApo 100X 1.45 NA $\infty/0.17$) plus an extra 1.5X magnification sliding lens coupled to an Andor EM-CCD camera (DV-897E-CS0). A 488-nm argon-ion laser (Melles Griot, 60mW, 543-AP-01),) was used to excite the HiLyte488 microtubules, a 532-nm diode laser (World Star Tech, 30 mW, model #TECGL-30) was used to excite the fluorescent beads and a 633-nm HeNe laser (Coherent HeNe laser, 4mW, model #31-2041-000) was used for imaging the Alexa647 dye attached to the reference K432. In the microscope, optical filters were used to separate the laser lines from the sample fluorescence. A z488/532/633rpc (Chroma) triple bandpass dichroic mirror was used in combination with a z488/532/635m (Chroma) triple bandpass emission filter. For viewing the microtubules, an additional sliding filter (Chroma, HQ525/50M) was used to block the emission of the fluorescent beads, which was very broad. For each field of view, images with the three lasers were taken sequentially. A single image of the microtubules was taken, followed by a 50 second movie of the reference kinesin taken at a frame rate of 10 Hz. Each fluorescent bead movie was taken at 10 Hz for 2000 frames. For every field of view, no more than 4 fluorescent bead movies were recorded. No more than 90 minutes was allowed to elapse while recording data from a sample.

2.4.4 Data Analysis

Data was analyzed using Matlab code based on that written by Melinda Tonks-Hoffman and the PolyParticleTracker code package. PolyParticleTracker is localization and tracking code written by Salman Rogers that is freely available online (11). The analysis of data begins with using the Tonks-Hoffman program to determine the polarity of the microtubules in a field of view. An example of a field of view containing several microtubules is shown in figure 2.8A. First, a mask covering regions of the field of view where microtubules were located was created (Figure 2.8B) and was blocked into a set of rectangles (Figure 2.8C). Then, a kymograph of the reference

kinesin movie was created for each rectangular region in the mask (Figure 2.8D). The program displays the kymograph and asked the user to input the polarity of each microtubule or discard the microtubule for further analysis if the polarity was unclear from the kymograph. The most common reason for an unclear kymograph was that the microtubule was located at the edge of the 488 nm laser excitation, but just outside of the 633 nm laser excitation and therefore no reference kinesin could be seen traversing the microtubule. Rarely, two microtubules with opposite polarities would intertwine and reference kinesin could be seen walking in two directions over the microtubule.

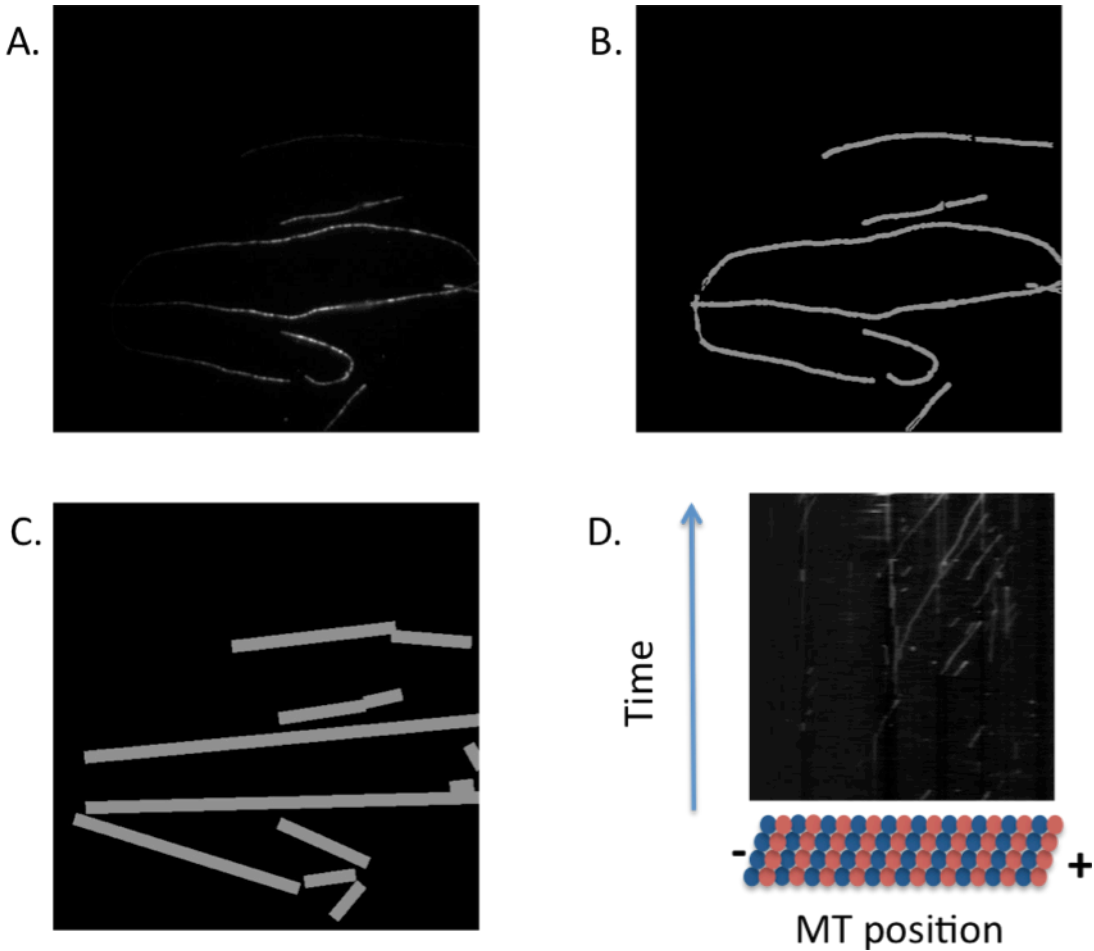


Figure 2.8: A. Image of fluorescent microtubules. B. Mask created by thresholding the microtubule image. C. Rectangularization of the mask in B. D. Kymograph. The fluorescence across a microtubule was plotted horizontally with time on the vertical axis. The positive slope of the reference kinesin on this microtubule indicates that the plus end must be on the right. Vertical lines in the kymograph occur when reference kinesin stick to microtubules but are not motile.

Once microtubules have been located and the polarity was known, a particle location algorithm was used to detect moving beads. The fluorescence intensity of the movie was normalized by summing the total intensity of each pixel throughout the bead movie and dividing each pixel by this sum. The movie was also masked according to the microtubule image results. Thresholding was then applied to the masked, normalized image. Pixels that were brighter than two times the standard deviation of the background were marked. In the three dimensional array of the

imaging plane as a function of time, volumes were formed which consisted of continuous areas marked pixels. For our imaging system, a threshold of 1,500 cubed pixels was applied as a lower bound for volume regions containing spots. This lower bound was necessary to remove beads which briefly diffused near the microtubule, but did not move along it or single, bright pixels due to cosmic rays hitting the EM-CCD camera. The overlap between regions of high intensity and the microtubule mask was compared to match moving beads to microtubules. Moving beads were excised into smaller sub-arrays and the polarity of the corresponding microtubule was recorded.

Each bead sub-array that could be matched to a microtubule was then tracked using both PolyParticleTracker and an Interactive Data Language (IDL) FIONA program.

PolyParticleTracker was used to roughly track bead position and further crop the images of the beads. Tracking was necessary to allow closer cropping of spots. The rough cropped trace of the sub-array could have spatial dimensions of tens of pixels. For long traces, it was likely that a second bead would also be seen moving along the microtubule for part of the movie or diffuse into the array and the FIONA Gaussian fitting was not equipped to handle more than one bright spot in a field of view. To separate multiple beads, PolyParticleTracker computed the tracks of all beads in the sub-array. Once the tracks were known, a 13x13 pixel box, centered at the bead position was cropped for each frame around each bead. FIONA was applied to locate the bead with approximately 1 nm precision within each 13 by 13 box. The PolyParticleTracker algorithm did a good job of locating and linking images into tracks, its fit to the center of each bead was computed by fitting the fluorescent to a polynomial and was less accurate than the Gaussian fitting of FIONA. The FIONA results and track from PolyParticleTracker were then combined to produce a trace of the bead position as a function of time.

The resulting traces and cropped beads were checked by eye a final time. Occasionally, several beads would stick together in a large, bright cluster and move along a microtubule. These clusters were obvious from their intensity and size and were removed to create a dataset consisting of only single, motile beads. The net distance traveled and average velocities over the course of the trace of these beads were plotted. Also, for every bead, the direction and motion and number of reversals, if any, was recorded. A reversal was defined as a change in direction of the bead with at least 500 nm traveled on either side of reversal point.

Section 2.5: Optical Trapping Experiments

2.5.1 Optical Trap Construction

The optical trap was custom built by Benjamin Blehm. All data acquired on the trap was taken in collaboration with Benjamin Blehm or Janet Sheung, who operated the trap during data acquisition. The trapping and detection of particles was accomplished by two different lasers, a 1064-nm trapping laser (SpectraPhysics, Nd:YVO₄, BL-106C) and a 845-nm detection laser (Lumics, LU0845M150-1G36F10A). A Nikon 60X 1.2 NA water immersion microscope objective inside of an inverted Nikon TE-2000-U microscope was used to image the beads in the trap and both the detection and trapping lasers were directed through this objective.

The position of the trapping laser was controlled by an acousto-optic modulator (Gooch & Housego, 23080-3-1.06). An AOM precisely controls the deflection of the trap laser on short time scales (100 ns), making it well suited for controlling the position of the trap. It is made of a material like quartz or glass that is attached to a piezo-electric transducer. The piezo-electric transducer vibrates at radio frequencies, causing waves to propagate through the glass. The sound waves alter the index of refraction of the glass in a periodic manner, creating an effective diffraction grating with “slit” spacing that depends on the wavelength of the input RF signal. The

AOM is designed such that most of the incident light ends up in the first diffraction maxima. Varying the RF signal changes the effective slit spacing of the grating and is used to control the position of the beam.

The position of the bead within the trap is detected by a quadrant photodiode (QPD) placed conjugate to the back focal plane of the objective. As the particle moves in the trap, it will scatter light at an angle relative to the laser. Angular changes in the focal plane of the particle become position changes in the back focal plane of the objective. The back focal plane of the objective is imaged onto the QPD. The quadrant photodiode consists of four diodes in a 2 by 2 configuration. The voltage of each diode is proportional to the intensity of light that is incident on it. Subtracting the two rows of the QPD produces a voltage that is proportional to the position in one dimension and subtracting the columns produces a voltage proportional to the position in the other dimension (Figure 2.9). For an appropriately chosen laser power, the voltage and position are linearly related. To convert the signal in of the QPD into position, a volts to nanometer calibration was performed by oscillating the position of the trap at 100Hz and comparing the amplitude of motion of a trapped bead to the known amplitude of the trap oscillation as described by Tolic-Norrelykke, et al (12). The trap electronics were controlled using a field programmable gate array (FPGA) data acquisition card and custom Labview code written by Benjamin Blehm (National Instruments, PXI-7851R and Labview v8.5).

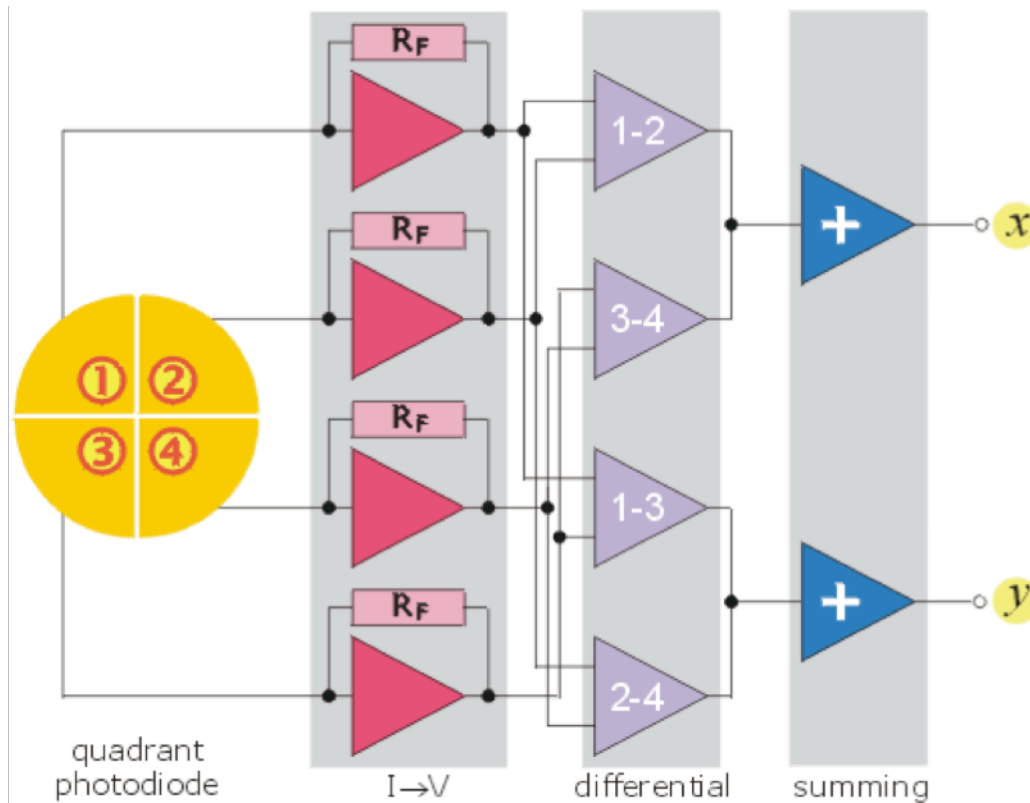


Figure 2.9: Diagram of a quadrant photodiode. The diode current is first converted to a voltage and amplified. By selectively subtracting and adding voltages, voltages proportional to the particle position relative to the center of the trap are obtained. From <http://www2.bioch.ox.ac.uk/oubsu/ebjknigh/q4d.html>.

The power spectrum method was used to measure trap stiffness. The equation of motion of a particle in the trap is given by the Langevin equation,

$$m\ddot{x} + \gamma\dot{x}(t) + kx(t) = F(t),$$

where m is the mass of the particle, $\gamma = 6\pi\eta r$ is the viscous drag coefficient (Stokes' drag) of the buffer on the particle, k is the trap stiffness. $F(t)$ is the Brownian noise due to thermal fluctuations and will have a mean of zero and a constant power spectrum such that

$$|F(f)|^2 = 4\gamma k_B T.$$

Here T is the temperature and k_B is the Boltzmann constant. The mass of the bead is very small, so the inertial term from the Langevin equation can be neglected. Taking the Fourier transformation of the rest of the equation of motion,

$$(-2\pi\gamma f_i + k)x(f) = F(f).$$

Setting $f_c = k/2\pi\gamma$, and taking the modulus of this equation yields,

$$|x(f)|^2 = \frac{k_B T}{\gamma(f_c + f)^2}.$$

This is a Lorentzian function with a corner frequency of f_c . The stiffness of the trap, k , can be measured by fitting the power spectrum of a bead in the trap to a Lorentzian function and using $f_c = k/2\pi\gamma$. For convenience, in our study the volts to nanometers conversion factor and stiffness were measured simultaneously by oscillating the trap position at a known frequency. The oscillation gives the V-to-nm factor and the power spectrum, excluding the peak due to the driving oscillation gave the stiffness.

2.5.2 Optical Trapping Assay

Motors were non-specifically attached to carboxylated beads in a similar manner as used in fluorescence imaging experiments. 500 nm red carboxylated microspheres (beads) were diluted 2:3 into DMB containing 8 mg/ml of BSA (DMB-BSA) and briefly sonicated in an ice bath to dissociate any large aggregates of beads and then mixed in a 1:1 ratio with diluted kinesin. Kinesin was diluted such that no more than 50% of the beads in a given sample were motile. This criteria of 50% comes from the assumption that the number of motors bound to a bead follows a Poisson distribution in which the probability of having n motors bound is given by

$$P(n) = \frac{\lambda^n e^{-\lambda}}{n!},$$

where λ is a fitting parameter. If less than 50% of beads brought near an axoneme bind, then by setting $P(0) > 0.5$, one finds that λ is no greater than 0.7. In this case, the probability of a bead having two or more motors attached to it is no more than 14%. If one further considers that two motors at opposite locations on the bead will not be able to both simultaneously engage with the microtubule, the probability of having two motors simultaneously pull on a cargo would be less

than 2% for a sample in which 50% of beads did not bind (13). By requiring that fewer than 50% of beads in a sample were motile ensures that no more than one motor be attached to a bead and the trapping measurements were reflective of single-molecule behavior and not the result of multiple motors pulling against the trap.

In practice, we found that diluting kinesin to 5-10 nM before mixing it with beads would produce a sample where 30-50% of beads were motile. After incubating the beads and kinesin for 30 minutes at 4 °C an imaging buffer was prepared containing DMB-BSA, 20 mM DTT, 4 mM ATP, 1mg/ml PCA, and 100 nM PCD. The bead and kinesin mixture was diluted 1:1000 in the imaging buffer and flowed over an axoneme slide. The axoneme slide was prepared in the same manner as for the single-molecule ATPase assay. A complete description of its preparation can be found in the section describing these experiments.

Trap data was acquired at room temperature with a data acquisition rate of 4000Hz. The trap stiffness was set by adjusting the trapping laser power such that the stall force of a motor corresponded to a position approximately 100 nm away from the center of the trap. This ensured that the motion of the motors would be confined to the region where force was a linear function of cargo position.

2.5.3 Data Analysis

Matlab software written by Benjamin Blehm was used to find motor stalls. The program converts the data from the QPD into motor force using both the volts-to-nanometers conversion factor and the trap stiffness determined during calibration. The force exerted on a bead by the motor is plotted as a function of time and the user is asked to manually identify regions where the motor stalls. For this analysis, stalls were defined as flat periods of less than 1 pN variation in force

which last for at least 0.5 seconds that are followed by a sharp drop back to the center of the trap. An illustration of the general shape of a stall is shown in figure 2.10.

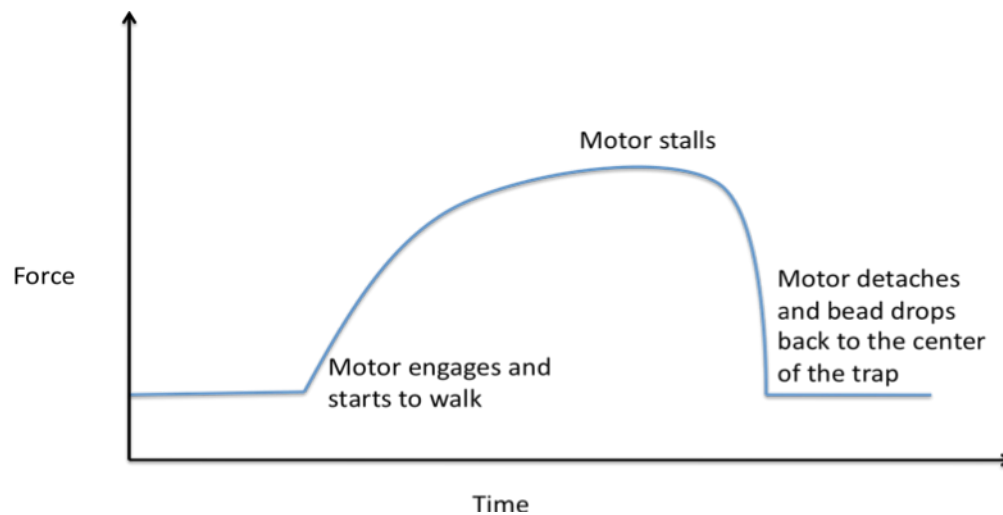


Figure 2.10: Illustration of a stall. As the motor engages and begins to walk on the microtubule, the restoring force of the trap that the motor must work against increases. When the motor can no longer pull against the trap, it stalls for a period of time, creating a flat region in the force vs. time curve. Once the motor detaches, the bead will drop back to the center of the trap.

References

1. Lu, H., M.Y. Ali, C.S. Bookwalter, D.M. Warshaw and K.M. Trybus 2009. Diffusive movement of processive kinesin-1 on microtubules. *Traffic*. 10, 1429-1438.
2. Crowe, J. and K. Henco 1992. *The QIAexpressionist*. Qiagen Inc, Chatsworth, CA, USA.
3. Bingham, J. B., S.J. King and T.A. Schroer 1998. [15] purification of dynactin and dynein from brain tissue. *Meth. Enzymol.* 298, 171-184.
4. Pierce, D. W. and R.D. Vale 1998. Assaying processive movement of kinesin by fluorescence microscopy. *Methods Enzymol.* 298, 154-171.
5. Gibbons, I. and E. Fronk 1979. A latent adenosine triphosphatase form of dynein 1 from sea urchin sperm flagella. *J. Biol. Chem.* 254, 187-196.
6. Morfini, G., G. Pigino and S.T. Brady 2007. Approaches to kinesin-1 phosphorylation. *Methods Mol. Biol.* 392, 51-69.
7. Bradford, M. 1976. A rapid and sensitive method for the quantitation of microgram quantities of protein utilizing the principle of protein-dye binding *anal biochem* 72: 248–254. Find this Article Online.

8. Webb, M. R. 1992. A continuous spectrophotometric assay for inorganic phosphate and for measuring phosphate release kinetics in biological systems. *Proceedings of the National Academy of Sciences*. 89, 4884-4887.
9. Hackney, D. D. 1988. Kinesin ATPase: Rate-limiting ADP release. *Proc. Natl. Acad. Sci. U. S. A.* 85, 6314-6318.
10. Woehlke, G., A.K. Ruby, C.L. Hart, B. Ly, N. Hom-Booher and R.D. Vale 1997. Microtubule interaction site of the kinesin motor. *Cell*. 90, 207-216.
11. Rogers, S. S., T.A. Waigh, X. Zhao and J.R. Lu 2007. Precise particle tracking against a complicated background: Polynomial fitting with gaussian weight. *Physical Biology*. 4, 220.
12. Tolic-Nørrelykke, S. F., E. Schaffer, J. Howard, F.S. Pavone, F. Julicher and H. Flyvbjerg 2006. Calibration of optical tweezers with positional detection in the back focal plane. *Rev. Sci. Instrum.* 77, 103101-103101-11.
13. Svoboda, K. and S.M. Block 1994. Force and velocity measured for single kinesin molecules. *Cell*. 77, 773-784.

Chapter 3: Results

Section 3.1: S175 Modification Does Not Alter Kinesin's Chemical Kinetics

3.1.1: Summary of Experiments

We measured the ATPase activity of kinesin-888 in two different contexts. First, we measured the rate of ATP hydrolysis of different S175 mutants. To accomplish this goal, we varied the ATP concentration, while keeping the other experimental parameters constant. By measuring kinesin's velocity as a function of ATP concentration, we determined the Michaelis-Menten constant, K_m , which is a measure of the affinity of an enzyme for its substrate, here, ATP. We also measured the microtubule-activated ATPase activity of kinesin-888. In these experiments, the microtubule concentration was titrated and ATP and kinesin concentrations were kept constant. These second experiments measured the affinity of kinesin for microtubules since microtubules are required for kinesin to hydrolyze ATP effectively (1).

For both sets of experiments, we chose to focus on different kinesin-888 mutants. To briefly review, these three mutants were a phosphomimetic kinesin construct, S175D, in which an aspartic acid residue mimicked the negative charge of phosphate, a non-phosphorylatable alanine mutant, S175A, and a truncated mutant with a wild-type sequence (unmutated kinesin-888, which we will refer to as WT). All of these mutants were truncated to remove the auto-inhibitory C-terminal domain of kinesin, residues 889-963. The truncated kinesin is constitutively active and incapable of folding into its autoinhibited conformation. This allowed us to study the effects of S175 modification on kinesin-ATP and kinesin-microtubule interactions without autoinhibition, which by itself may be affected by S175 modification. For example an increase in autoinhibition would interfere with kinesin's ability to bind to microtubules and hydrolyze ATP and confound the results.

3.1.2 S175 Modification Has No Effect on Kinesin's Affinity for ATP

To test the effect of a negative charge at S175 on the ATPase activity of kinesin, we measured the velocity of quantum-dot labeled kinesin as a function of ATP concentration. Although there are many bulk assays that measure the level of free phosphate released in an enzymatic reaction, we chose to perform a single-molecule experiment. The weakness of bulk assays is that they can be biased by inactive kinesin in the solution. While small, there is always some fraction of protein in a purified batch that is not motile. A bulk assay would average over these differences, confounding the effect of a lower maximum reaction velocity and a less active motor preparation. The benefit of a single molecule experiment is that it allows a direct comparison of the maximum velocities of different preparations of kinesin. In our single molecule assay, only active motors that bound to the microtubule-rich axoneme tracks and walked were measured.

We used ATP concentrations between 10 μ M and 1 mM and measured the mean velocity of 40 to 70 kinesin molecules attached to fluorescent quantum dots for each ATP concentration. Representative histograms of velocities measured at defined ATP concentrations are shown in figure 3.1.

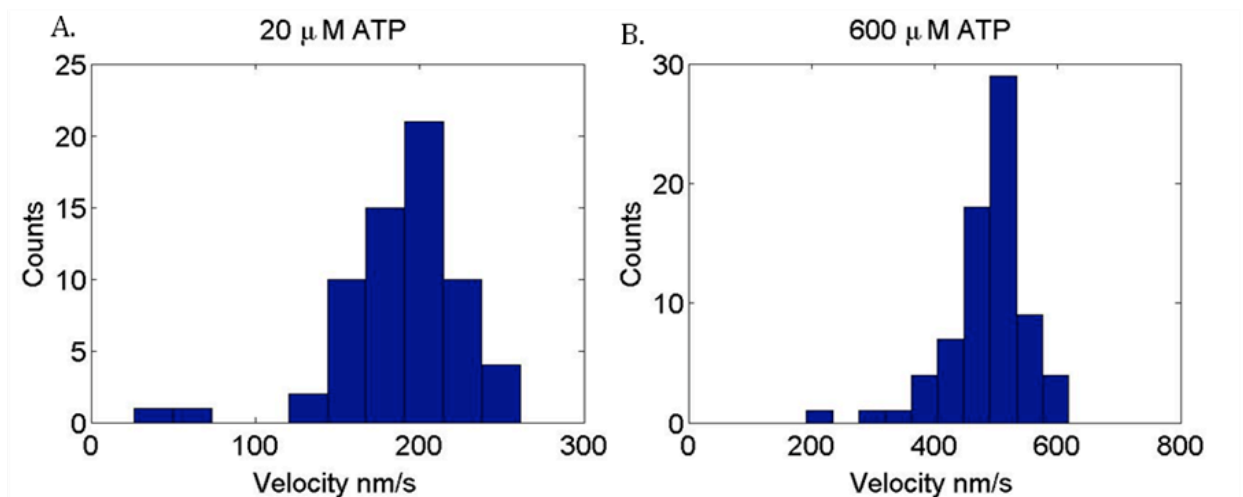


Figure 3.1: Kinesin velocity distributions at A. 20 mM ATP and B. 600 mM ATP. Both histograms were compiled from data taken with the S175A mutant.

The respective velocity was plotted against ATP the concentration and data was subsequently fit with the Michaelis-Menten function, as shown in Figure 3.2. The extracted kinetic parameters, maximal velocity and Michaelis-Menten constant, of each mutant are summarized in table 3.1. If adding a negative charge at S175 were to decrease the affinity of kinesin for ATP, we would expect a higher K_m for the S175D mutant we tested. We found that the S175D mutation did not significantly change the K_m or the maximum velocity of kinesin, (see Table 3.1). This indicates that an additional negative charge at this position does not alter kinesin's affinity for ATP. Additionally, we did not observe different parameters for the S175A mutation relative to wild-type protein.

KINESIN MODIFICATION	K_M (μM)	V_{MAX} (nm/s)
S175A	44 ± 9	493 ± 24
S175D	44 ± 10	494 ± 28
None (wild type)	35 ± 8	484 ± 23

Table 3.1: Table 3.1: Summary of the ATPase kinetics of kinesin-888 mutants.

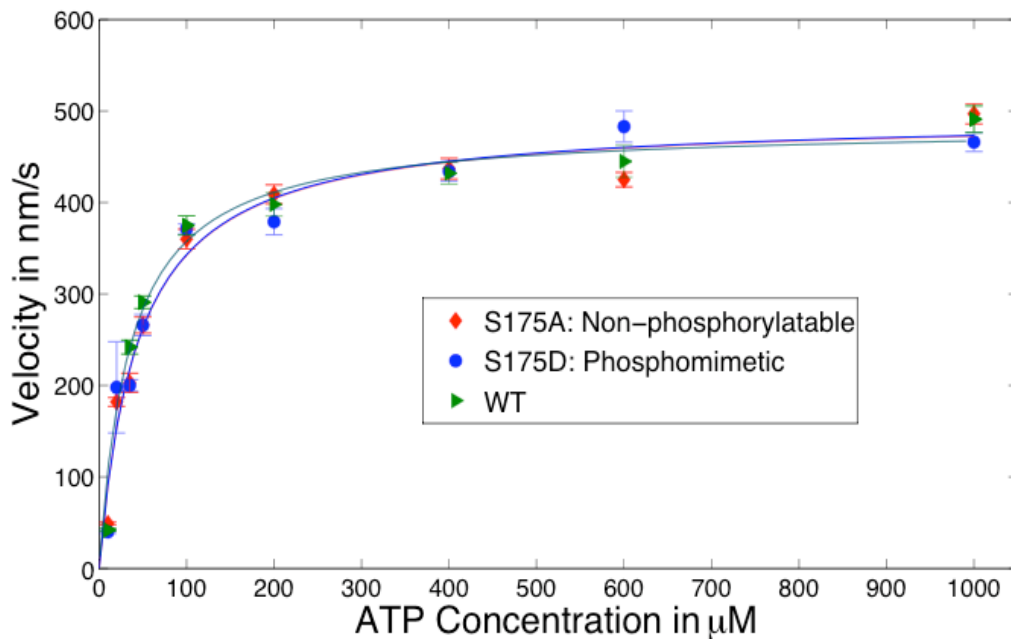


Figure 3.2: ATPase activity of kinesin. There is no significant difference in the velocity of the three different kinesin mutants as a function of ATP concentration. The error bars are the standard error of the mean velocity at each ATP concentration.

3.1.3 S175 Modification Does Not Have a Significant Effect on Microtubule Affinity.

Having found that kinesin's affinity for ATP was not affected, we next focused on its affinity for microtubules. These experiments had to be performed in bulk, to allow the precise adjustment of the microtubule concentration. In this set of experiments, the microtubule concentration was varied, while ATP was used at saturating concentrations. An enzyme-linked phosphatase assay was used to measure the rate of free phosphate released from ATP at different microtubule concentrations. As described in detail in the materials and methods section Chapter 2). The released phosphate was reflected by an increase in solution absorbance at 360 nm. Figure 3.3A shows an example plot of the increase in absorbance as a function of time. As time increases, the kinesin hydrolyzes progressively more of the ATP in the solution until the absorbance reaches a plateau. To measure the ATPase activity of the kinesin prior to ATP depletion, a linear fit to the data points in the first 30 seconds was used (Figure 3.3B).

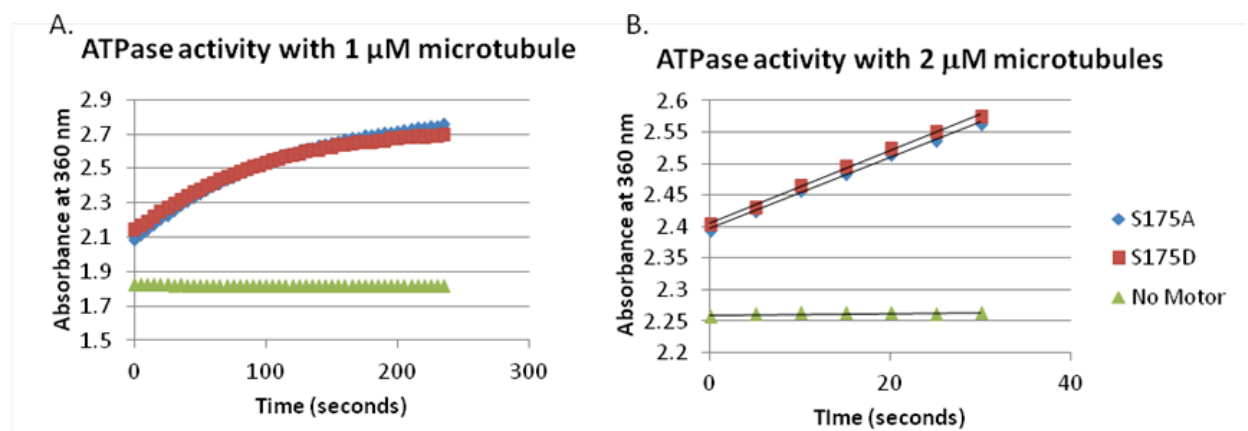


Figure 3.3: Microtubule activated ATPase assay data: The data for S175A is shown in blue, the data for S175D is shown in red and the green data points are control runs in which no motor was added to the assay mixture. The control shows that the addition of motor does not affect A_{360} . A. The absorbance at 360 nm increases over time as kinesin hydrolyzes ATP. B. The first 30 seconds can be fit to a line.

The resulting slope of the linear fit performed using the first thirty seconds can be converted into the number of ATP molecules hydrolyzed per motor domain of kinesin per second with two pieces of additional knowledge: the known concentration of kinesin that was added to the

solution and a standard curve relating A_{360} to the amount of phosphate added to the reaction. In between 1 and 10 nanomoles phosphate, A_{360} and the amount of phosphate in the assay mixture are linearly related. A standard curve linking phosphate concentration to A_{360} was generated using defined concentrations of KH_2PO_4 , and is shown in Figure 3.4..

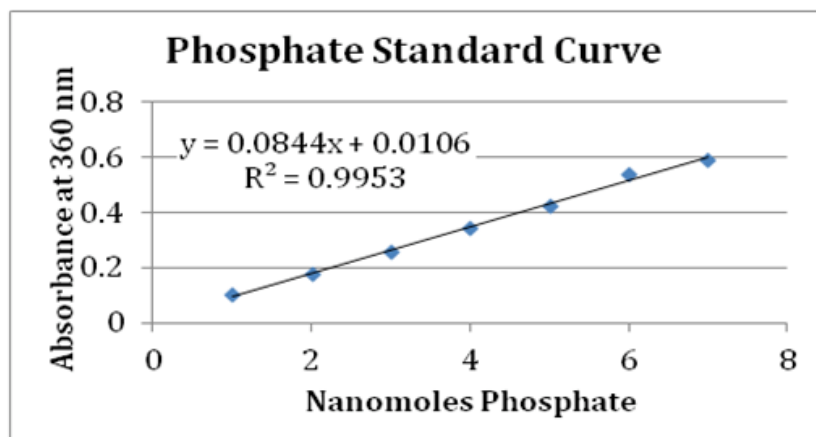


Figure 3.4: Phosphate standard curve. KH_2PO_4 , was added to the assay mixture to measure the increase in absorbance at 360 nm as a function of phosphate concentration

The microtubule activated ATPase activity of kinesin can reasonably be described by Michaelis-Menten kinetics (however, we note that strictly MM kinetics are only applicable for single substrate reactions, while kinesin has two “substrates” ATP and microtubules). It is difficult to directly compare the maximum reaction velocity of different types of kinesin due to differences in preparation. More useful, is the Michaelis constant, $K_m\text{MT}$, which is independent of the concentration of active protein in the solution. Figure 3.5 shows the resulting microtubule-activated ATPase curves and table 3.2 summarizes the kinetic parameters measured in the single-molecule and microtubule-activated ATPase experiments As previously discussed, mutations in kinesin that negatively affect microtubule binding, but don't affect the overall rate of ATP hydrolysis are expected to result in increased $K_m\text{MT}$ values (2). Our results show that there is no significant difference in microtubule affinity regardless of the charge at S175 (see Table 3.2). For each kinesin mutant, the assay was repeated for two or three data points to check the consistency of the results.

KINESIN MODIFICATION	$K_{M}MT$ (μM)	$V_{MAX}MT$ (ATP molecules/kinesin monomer/s)
S175A	0.65 ± 0.25	10.6 ± 1.4
S175D	0.74 ± 0.22	10.8 ± 1.1
None (wild type)	0.70 ± 0.26	11.3 ± 1.6

Table 3.2: Summary of the ATPase kinetics of kinesin-888 mutants.

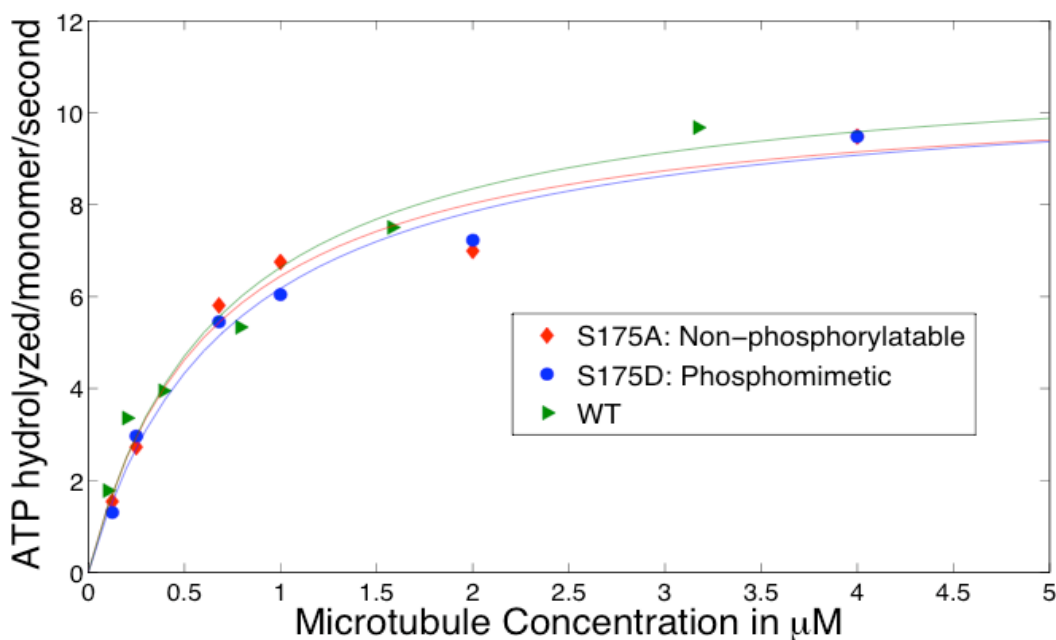


Figure 3.5: Microtubule activated ATPase curves. A nonlinear Michaelis-Menten fit was applied to each data set.

Section 3.2: The Processivity of Kinesin is Not Substantially Altered by Modification of Residue 175

Processivity describes the length scale of molecular motor transport. It is a measure of the distance a motor travels before dissociated from a microtubule. Kinesin is a very processive motor. It can take over 100 steps along a microtubule before dissociating (3, 4). Processivity depends on the mechanical coupling of kinesin's ATP hydrolysis and stepping of the two heads and the strength of the kinesin-microtubule interactions (4). To probe whether the S175D mutation would have an effect on processivity, we measured the run length of different kinesin mutants. We labeled kinesin with quantum dots and combined FIONA with tracking to measure

the distance travelled by kinesin before falling off the microtubule. All experiments were performed at saturating levels of ATP. Andrew Thompson at the University of Vermont performed experiments on the S175A and S175D kinesin-888 mutants and analyzed the data to extract distances. We plotted this data in the Selvin lab and fit it to an exponential distribution to extract the characteristic run length of kinesin. We measured a run length of $1.06 \pm 0.08 \mu\text{m}$ for S175A (N=117) and $0.89 \pm 0.08 \mu\text{m}$ for S175D (N=91). The resulting distributions are shown in figure 3.6. We applied a Kolmogorov-Smirnov significance test and found that the S175A and S175D distributions did not differ significantly with $p = 0.48$.

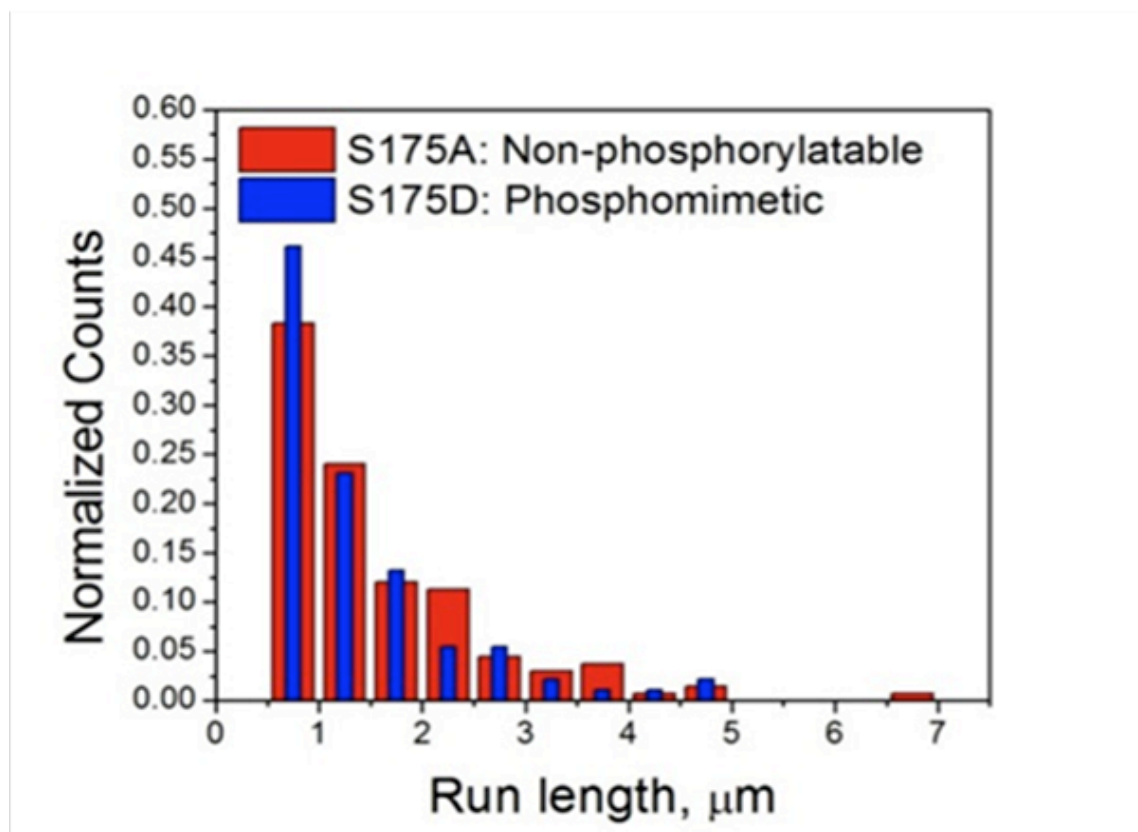


Figure 3.6: Processivity: Run length distributions for S175A and S175D.

Section 3.3: Measuring Phosphorylation Efficiency.

The kinetic studies involved genetically modified phosphomimetic kinesin only. However, for later studies, we wanted to look at true phosphorylation. To accomplish this we established an in vitro phosphorylation procedure to conduct experiments on physiologically relevant, S175

phosphorylated kinesin. We used JNK3 to phosphorylate full-length kinesin. A small reaction with radioactive ATP ($[\gamma\text{-}^{32}\text{P}]$ ATP) was run alongside a non-radioactive reaction to quantify the extent of phosphorylation as described detail in the materials and methods section. An example denaturing polyacrylamide gel of radiolabeled protein is shown in figure 3.7A. The first lane (1) contains the phosphorylated kinesin, indicated by an asterisk (*) near the band. The fainter band beneath the phosphorylated kinesin (**) is JNK3, which is known to autophosphorylate (5). The large dark spot at the bottom of the gel is unreacted, radiolabeled ATP. The right lanes, 2 through 6 (marked by the arrow) are different concentrations of $[\gamma\text{-}^{32}\text{P}]$ ATP, diluted such that the amount of radioactive phosphate in each band would correspond to a defined radiolabeling efficiency of kinesin. The intensities above the background level of the standard ATP bands were summed and compared to the intensity of the kinesin band. As shown as the black linear fit to the data points figure 3.7B, the band intensity as a function of phosphorylation efficiency increased linearly. The intersection of the standards with the red line, which marks the intensity of the kinesin band, occurs at 81%, indicating that around 80% of the kinesin motor domains in the reaction were phosphorylated.

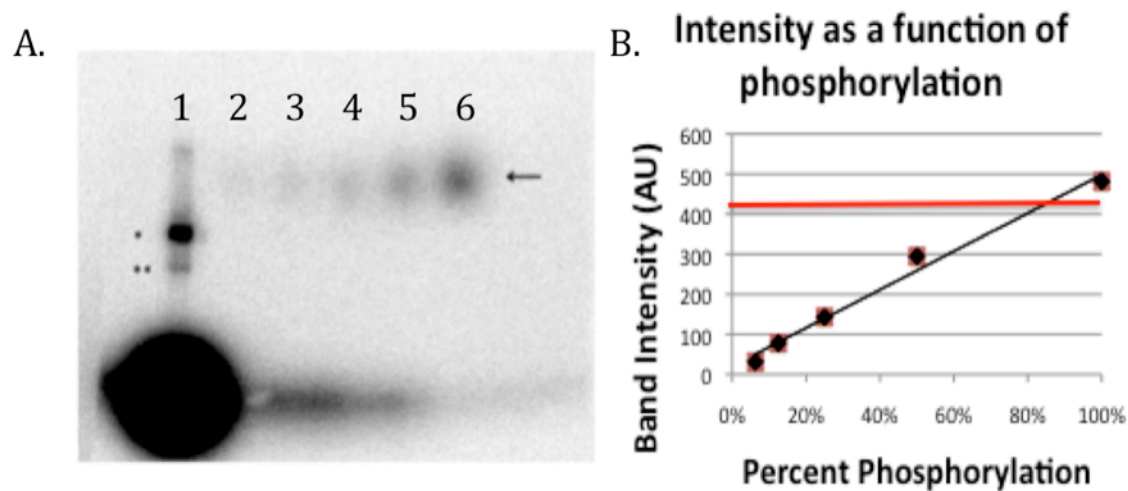


Figure 3.7: Measuring phosphorylation using radiolabeling. A. SDS-PAGE of radiolabeled kinesin-1. Lane 1 contains kinesin (*) and JNK3 (**), and unreacted $[\gamma\text{-}^{32}\text{P}]$ ATP (large dark spot at the bottom left). Lanes 2 through 6 contain ATP standards corresponding to labeling efficiencies varying from 6 to 100% (arrow). Lane 6 contained the amount of radioactive ATP that would correspond to 100% phosphorylation of kinesin, lane 5 to 50%, 4 to 25%, 3 to 12.5% and 2 to 6.25%. B. ATP standard band intensity as a function of P^{32} labeling of kinesin (black line) and kinesin band intensity (red line).

Section 3.4: Phosphorylated and Phosphomimetic Kinesin Have a Reduced Stall Force

We used optical trapping to measure the stall force of kinesin attached to 500 nm diameter polystyrene beads. For both phosphomimetic and phosphorylated kinesin, we observed a decrease in stall force relative to wild-type or non-phosphorylatable kinesin. We measured both types of different kinesin-888 mutants as well as full-length NK3 phosphorylated kinesin. The phosphomimetic S175D stalled at 5.28 ± 0.09 pN, while the non-phosphorylatable S175A mutant stalled at approximately 7.46 ± 0.25 pN (errors are given as standard error of the mean). Figure 3.8A shows a histogram of stall forces. Previous measurements have reported kinesin stall forces of 5-7 pN for unmutated protein (6, 7). Figure 3.8B shows a representative stall.

We also measured the stall force of JNK3 phosphorylated protein and found a decreased stall force. Wild-type kinesin-888 had a stall force of 7.44 ± 0.18 pN similar to the non-phosphorylatable S175A mutant. 60% phosphorylation of wild-type kinesin-888 was achieved. As no complete phosphorylation was achieved there are potentially three populations of kinesin present in the sample: unphosphorylated kinesin as well as single and double phosphorylated motors. Assuming that the two motor domains are phosphorylated independently, 60% phosphorylation of motor head monomers would imply that 36% of kinesin dimers had two phosphorylated heads, 48% had one phosphorylated head and 16% had no phosphate present in either head. While it is difficult to assign a characteristic stall force to a heterogeneous sample, the mean stall force of this partially phosphorylated sample was 6.80 ± 0.17 pN, a decrease of 0.64 pN from the stall force of unmodified kinesin-888. Figure 3.8C shows the stall force histograms for this data.

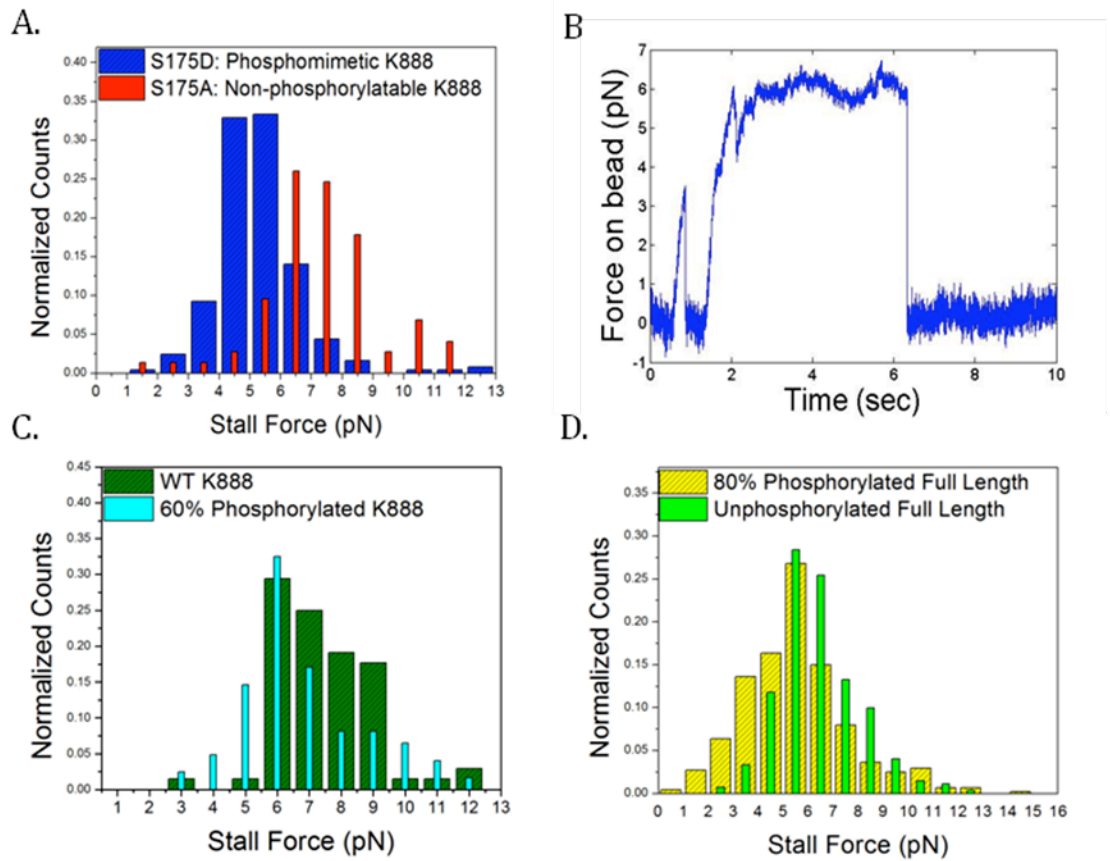


Figure 3.8. Stall force data. A. Kinesin-888 stalls for the S175A (N=73) and S175D (249) mutants. B. A characteristic stall. C. Stalls force of unphosphorylated wild type kinesin-888 (N=68) and 60% phosphorylated protein (N=123). D. Stall force of unphosphorylated full-length kinesin (N=271) and 80% phosphorylated protein (N=440).

A decreased stall force was also observed in phosphorylated wild-type, full-length kinesin. Unphosphorylated full-length kinesin had a stall force of 6.43 ± 0.10 pN. An 80% phosphorylated sample (assumed to consist of 64% dimers with two phosphorylated heads, 32% dimer with one phosphorylated head and 4% with no phosphorylation) had a mean stall force of 5.54 ± 0.10 pN. Figure 3.8D shows stall force histograms for full-length kinesin. Table 3.3 summarizes all stall force measurements.

KINESIN MODIFICATION	KINESIN LENGTH	STALL FORCE (pN)
S175A	888	7.46 ± 0.25
S175D	888	5.28 ± 0.09
None (wild type)	888	7.44 ± 0.18
60% phosphorylated	888	6.80 ± 0.17
None (wild type)	963 (Full)	6.43 ± 0.10
80% phosphorylated	963 (Full)	5.54 ± 0.10

Table 3.3: Summary of stall force measurements.

Section 3.5: S175 Modification Biases Transport Toward Microtubule Minus Ends

To study the effect of kinesin phosphorylation in a more physiological context, we coated polystyrene bead cargo with both kinesin and dynein. We attached kinesin and cytoplasmic dynein to 500 nm fluorescent polystyrene beads and observed the resulting motion. An example trace of bead position as a function of time is shown in figure 3.9.

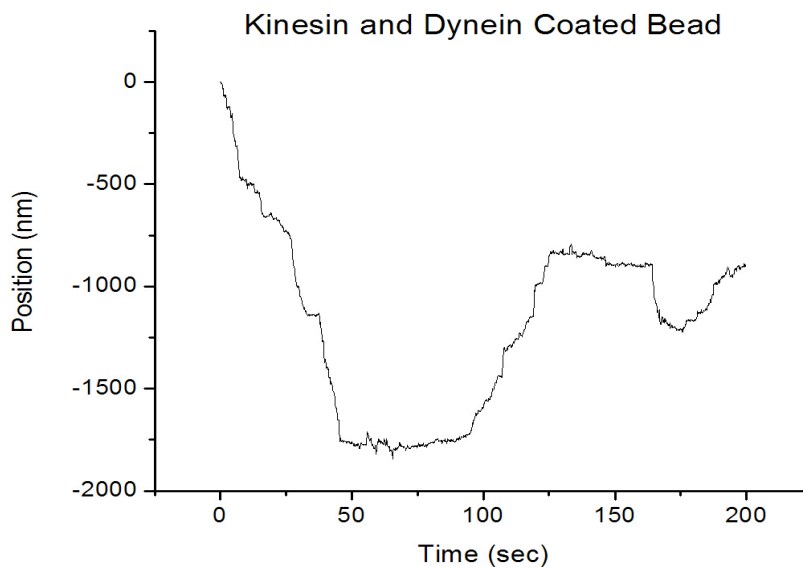


Figure 3.9: Example of a bead coated with full-length unphosphorylated kinesin and dynein undergoing bidirectional motion. FIONA was used to determine the position of the bead in each frame. Motion with a positive slope is directed towards the microtubule plus end and motion with a negative slope is directed toward the minus end.

We characterized the motion of the two-motor coated beads with several measurements. We first measured the direction of the bead along a microtubule, counting how frequently beads

moved toward the plus-end, the minus-end, or reversed directions. We also measured the total distance traveled by a bead along the microtubule from the time it first contacted the microtubule to when it finally released from its track and diffused away. We also measured the average velocity of a bead during its transit.

In our measurements of the direction traveled by beads, we looked at the motion of a reference kinesin that was labeled with a fluorescent antibody to determine the plus-end of the microtubule as described in chapter 2. We then monitored the direction of motion of beads coated with kinesin and dynein. We measured whether a bead moved only toward the plus-end, only toward the minus-end or underwent bidirectional motion. A trace was scored as displaying bidirectional motion if the bead was transported at least 500 nm in each direction both before and after a reversal. We found that beads coated with the phosphomimetic S175D kinesin mutant and dynein were showed decreased plus-end motility relative to beads coated with dynein and either wild-type kinesin or the S175A, alanine mutant. Figure 3.10A shows the results of our observation for the kinesin-888 mutants. Experiments using the JNK-3 treated, 80% phosphorylated kinesin also showed a bias away from plus-end transport and toward minus-end directed transport linked to phosphorylation (Figure 3.10B).

In order to control for the possibility that different protein preparations may have different amounts of active and inactive protein, we used the same dynein preparation for all experiments and performed an axoneme activity purification assay on the kinesin, as described in detail in the materials and methods chapter. The activity purification assay removed inactive proteins, leaving a sample consisting of active kinesin. The concentrations of dynein and kinesin were kept constant within the set of kinesin-888 experiments and the set of full-length experiments.

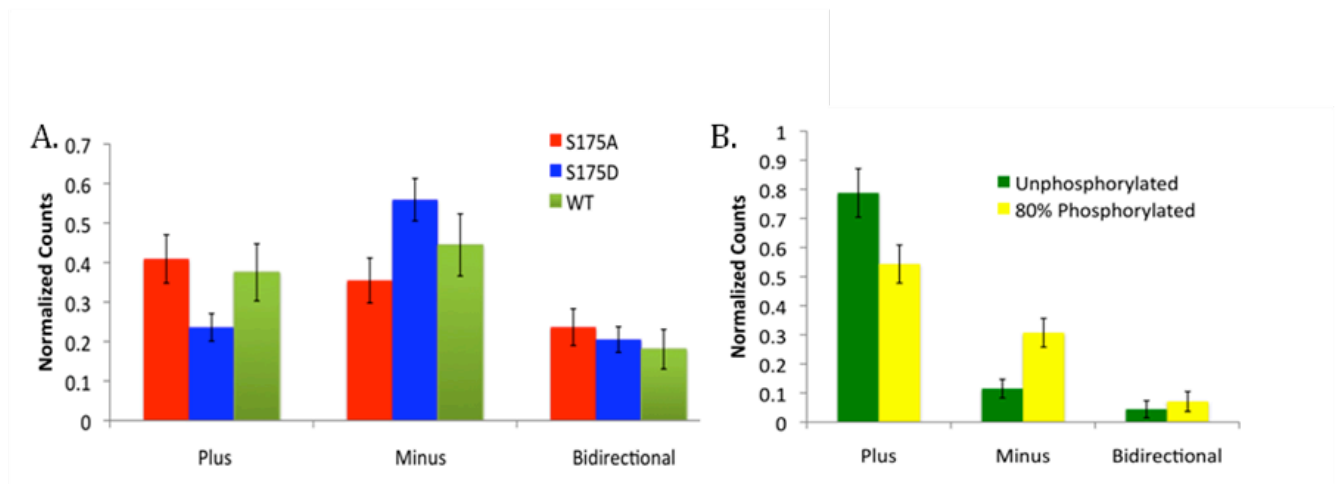


Figure 3.10: Direction traveled A. Cargo coated with S175A and dynein (red, N=110) or S175D and dynein (blue, N=195), and wild-type and dynein (green, N=72). (B) Cargo coated with full-length unphosphorylated kinesin and dynein (green, N=113), and full-length 80% phosphorylated kinesin and dynein (yellow, N=127).

We also measured the total distance traveled by beads carried by two different motors. We set the origin to be the location where the bead first contacted the microtubule. Positive distances corresponded to motion toward the plus-end and negative distances corresponded to motion toward the minus-end. On average, phosphomimetic kinesin (S175D) and dynein-coated cargo showed motion shifted toward the minus-end relative to motion of cargo coated with S175A and dynein. Table 3.3 summarizes the mean velocities and distances traveled and figure 3.11 shows the distributions of velocities and distances traveled for each mixture of kinesin and dynein. The distributions of distances travelled differ significantly ($p = 7.4 \times 10^{-5}$) as verified by a Kolmogorov–Smirnov test. The distributions of distances travelled by 80% phosphorylated and unphosphorylated beads also differed significantly ($p = 4.7 \times 10^{-5}$)

MIXTURE OF MOTORS	NUMBER OF OBSERVATIONS	MEAN DISTANCE	STANDARD DEVIATION OF DISTANCES	MEAN VELOCITY	STANDARD DEVIATION OF VELOCITIES
S175A + Dynein	74	1.7 μm	3.8 μm	23.5 nm/s	145.9 nm/s
S175D + Dynein	151	0.4 μm	4.3 μm	-55.6 nm/s	127.4 nm/s
Unphosphorylated kinesin + Dynein	105	3.4 μm	4.0 μm	169.8 nm/s	251.1 nm/s
80% phosphorylated kinesin+ Dynein	117	0.6 μm	4.4 μm	51.7 nm/s	210.9 nm/s

Table 3.3: Motility assay data for mutated and phosphorylated kinesin.

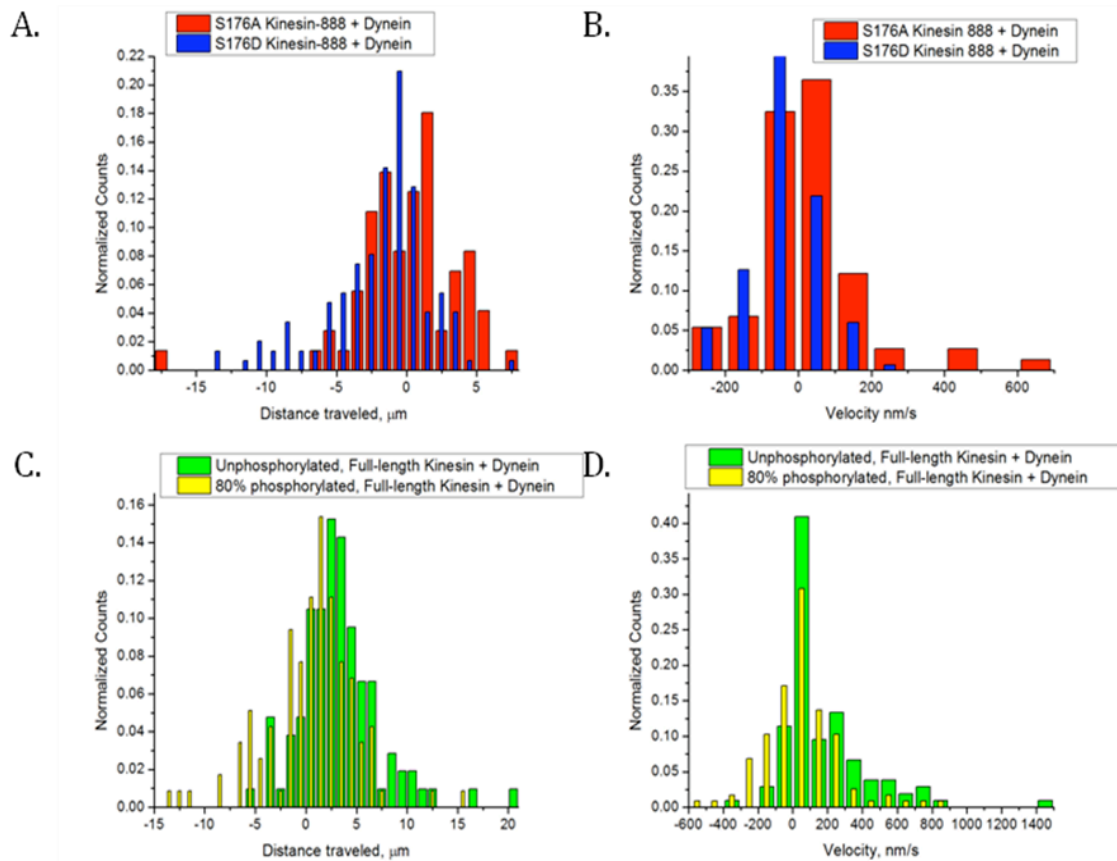


Figure 3.11: A. Distances traveled by beads coated with kinesin-888 and dynein. B. Velocities of kinesin-888 and dynein coated beads. C. Distances traveled by full-length kinesin and dynein coated beads. D. Velocities of full-length kinesin and dynein coated beads. Positive distances indicate net motion toward the microtubule plus end and negative distances and velocities indicate motion toward the minus end.

References

1. Kuznetsov, S. A. and V.I. Gelfand 1986. Bovine brain kinesin is a microtubule-activated ATPase. *Proc. Natl. Acad. Sci. U. S. A.* 83, 8530-8534.
2. Woehlke, G., A.K. Ruby, C.L. Hart, B. Ly, N. Hom-Booher and R.D. Vale 1997. Microtubule interaction site of the kinesin motor. *Cell.* 90, 207-216.
3. Furuta, K., A. Furuta, Y.Y. Toyoshima, M. Amino, K. Oiwa and H. Kojima 2013. Measuring collective transport by defined numbers of processive and nonprocessive kinesin motors. *Proc. Natl. Acad. Sci. U. S. A.* 110, 501-506.
4. Hancock, W. O. and J. Howard 2004. Kinesins: Processivity and chemomechanical coupling. *Molecular Motors.*, 243-269.

5. Vogel, J., V. Anand, B. Ludwig, S. Nawoschik, J. Dunlop and S. Braithwaite 2009. The JNK pathway amplifies and drives subcellular changes in tau phosphorylation. *Neuropharmacology*. 57, 539-550.
6. Meyhöfer, E. and J. Howard 1995. The force generated by a single kinesin molecule against an elastic load. *Proceedings of the National Academy of Sciences*. 92, 574-578.
7. Svoboda, K. and S.M. Block 1994. Force and velocity measured for single kinesin molecules. *Cell*. 77, 773-784.

Chapter 4: Conclusions

4.1: Effects of Serine 175 Phosphorylation

We used biochemical and biophysical assays to probe the effect of serine 175 phosphorylation on the behavior of the kinesin motor protein. Our goal was to discover the mechanism by which this phosphorylation site affected kinesin-based microtubule transport. In three biochemical assays, we found no change. First, we found that a phosphomimetic kinesin did not possess an altered ATPase activity or Michaelis-Menten constant, indicating that addition of a negative charge at S175 did not affect the ability of kinesin to bind and hydrolyze ATP. Second, we have shown that enzyme kinetic parameters are unchanged in phosphomimetic kinesin when microtubule affinity was tested. Third, the processivity of phosphomimetic and non-phosphorylatable kinesin did not significantly differ. In summary there is no observable difference in the biochemical properties of unphosphorylated and phosphomimetic kinesin. However, we did see a difference in a two-motor motility assay and in a stall force measurement. Phosphorylated kinesin had a lower stall force than unphosphorylated kinesin. With a lower stall force the ability of phosphorylated kinesin to pull against a load is diminished. We also found that when both kinesin and dynein were attached to a polystyrene bead cargo, more motion toward the microtubule minus end was observed if phosphorylated or phosphomimetic kinesin was used than if unmodified kinesin was used. These results clearly demonstrate that the mechanical properties of kinesin are attenuated by S175 phosphorylation.

4.2: An Applied Force Leads to Defects in Kinesin Transport

We propose that the attenuation of kinesin from S175 phosphorylation is evident only upon the application of an external force. Two pieces of evidence support this. First, we observe an attenuated stall force that is 0.9 pN less than the stall force in the absence of phosphorylation for full-length protein and 2 pN less in the case of a phosphomimetic construct. Second, in two-

motor transport a recent study suggests that dynein remains bound to the microtubule during plus-end transport, dragging behind kinesin (1). This dragging acts as an opposing force that kinesin must work against. The ability of kinesin to pull against a force is reduced by phosphorylation of S175. A phosphorylated kinesin with a decreased stall force likely cannot pull against a few dynein as effectively as unphosphorylated kinesin. It would therefore lose the “tug-of-war”, thus shifting the balance toward more minus-end directed transport. The conclusion that dynein stays attached to the microtubule during plus-end directed movement is further supported by Tonks-Hoffman observed that in optical trapping experiments, dynein would remain attached to microtubules and take backward steps under an opposing force (2). The model of transport proposed by Blehm et al. and Tonks-Hoffman et al. is known as the “synergistic model” in which kinesin detaches from the microtubule during dynein-driven, minus-end transport, but dynein stays attached during kinesin-driven, plus-end transport (Fig 4.1).

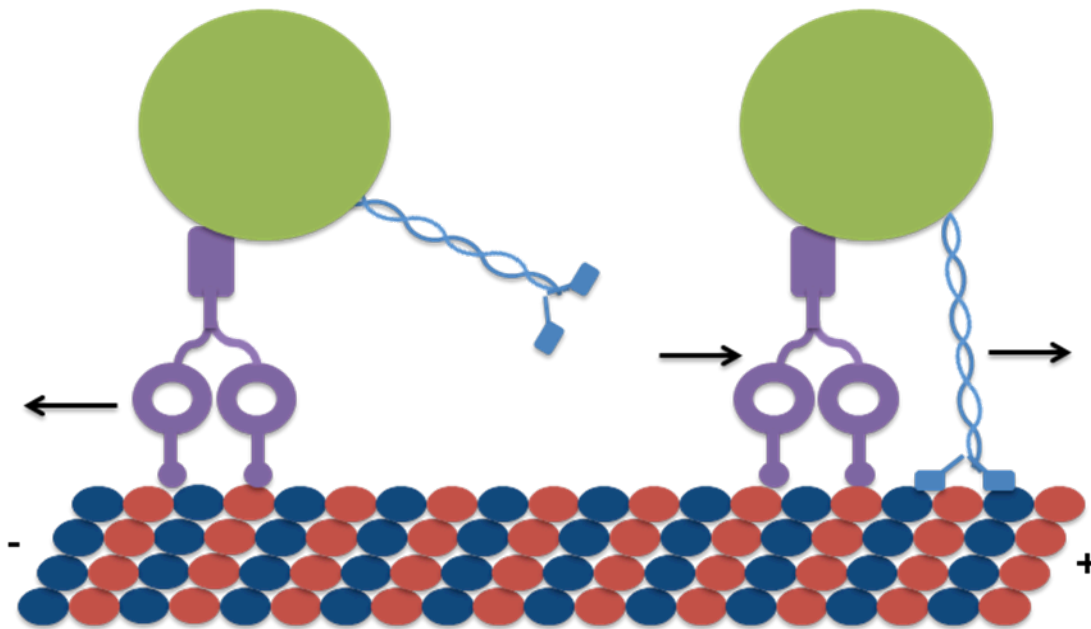


Figure 4.1: The Synergistic model of microtubule transport. During minus-end transport, dynein carries the cargo, but kinesin detaches. During plus-end transport, dynein drags behind kinesin.

Based on the synergistic model, it is likely that the reduction in plus-end motion we observe in phosphorylated kinesin and dynein coated beads is force-mediated. The opposing force

generated by dynein during plus-end directed transport shifts the balance between the two motors to favor minus-end transport as our data demonstrates.

4.3: Addition of a Negative Charge at Serine 175 is Sufficient for Kinesin Attenuation

Our experiments were performed in an *in vitro* system. The lack of external signaling molecules that would be present in a cell or cytoplasm allows us to isolate the effect of JNK3 phosphorylation on kinesin. Previous experiments by Morfini et al. linked JNK3 to transport defects in neurons and in squid axoplasm. The latter contains all of the signaling molecules that would be present in a cell and make it difficult to directly link JNK3 phosphorylation alone to transport defects in kinesin (3, 4). Our results indicate that phosphorylation alone is sufficient to decrease the stall-force of kinesin and bias the movement of cargo towards the minus end of microtubules when dynein is present. No other signaling or coordination molecules are needed.

4.4: S175 Phosphorylation is Consistent with Axonal Transport Associated with Huntington's Disease Pathology

Our results show that phosphorylation of serine 175 in kinesin-1B by JNK-3 leads to a statistically significant bias in a cargo driven by both kinesin and dynein. As such, it may offer neurons the ability to direct traffic in the axon by attenuating plus-end directed microtubule traffic. If constitutively upregulated in a pathological state, as may occur in Huntington's disease or SBMA, serine 175 phosphorylation of kinesin could result in long-term inhibition of kinesin-mediated axonal transport. Such transport defects may result in signaling defects and contribute to eventual neuronal death. Our results are consistent with the JNK3 mediated inhibition of fast axonal transport in squid axoplasm observed by Morfini et al (3, 4).

References

1. Blehm, B. H., T.A. Schroer, K.M. Trybus, Y.R. Chemla and P.R. Selvin 2013. In vivo optical trapping indicates kinesin's stall force is reduced by dynein during intracellular transport. *Proceedings of the National Academy of Sciences*.
2. Hoffman, M. T. 2011. Bidirectional cargo transport by microtubule-based molecular motors. PH.D thesis. University of Illinois at Urbana-Champaign, United States -- Illinois.
3. Morfini, G., G. Pigino, G. Szebenyi, Y. You, S. Pollema and S.T. Brady 2006. JNK mediates pathogenic effects of polyglutamine-expanded androgen receptor on fast axonal transport. *Nat. Neurosci.* 9, 907-916.
4. Morfini, G. A., Y.M. You, S.L. Pollema, A. Kaminska, K. Liu, K. Yoshioka, B. Bjorkblom, E.T. Coffey, C. Bagnato, D. Han, C.F. Huang, G. Banker, G. Pigino and S.T. Brady 2009. Pathogenic huntingtin inhibits fast axonal transport by activating JNK3 and phosphorylating kinesin. *Nat. Neurosci.* 12, 864-871.

Chapter 5: Future Experiments

5.1: Sedimentation Analysis

When autoinhibited, kinesin folds into a compact conformation, where the cargo-binding domain docks near the motor domains (1). Interactions between positively charged amino acids in the cargo-binding domain and the negatively charged phosphate group at S175 could enhance autoinhibition. Enhanced autoinhibition inside of cells could interfere with cargo binding and contribute to diminished axonal transport.

The relationship between phosphorylation and autoinhibition will be probed using a sedimentation analysis. Sedimentation is defined as the ratio of as the velocity to the acceleration of a particle due to centrifugation or another form of sedimentation.

$$s = \frac{v}{a_{centrifuge}}$$

A sedimentation analysis in a centrifuge is a useful way to probe the hydrodynamic radius of biological molecules. In solution, the drag force on a particle in a centrifuge is given by Stokes' law,

$$F_d = 6\pi\eta Rv,$$

where F_d is the drag force, η is the viscosity, R is the radius of the particle and v is the velocity.

The protein will reach a terminal velocity when the drag force is equal to the apparent centrifugal force,

$$F_c = mr\omega^2,$$

where m is the mass of the protein, r is the distance between the protein and the center of the centrifuge and ω^2 is the angular acceleration of the centrifuge. Setting the drag force and centrifugal forces equal, allows for the computation of the sedimentation coefficient, s , according to

$$mr\omega^2 = 6\pi\eta Rv$$

$$s = \frac{v}{r\omega^2} = \frac{m}{6\pi\eta R}$$

Kinesin is known to undergo a transition to lower sedimentation coefficient at elevated salt concentrations. The addition of salt disrupts the docking of the auto inhibition domain to the motor domains and causes the protein to unfold into a spatially extended conformation, which has a larger hydrodynamic radius and hence a smaller sedimentation coefficient. By measuring the sedimentation coefficient of unphosphorylated kinesin and phosphorylated kinesin as a function of salt, changes in the efficiency of autoinhibition may be detectable. If phosphorylation enhanced autoinhibition, higher sedimentation values as a function of salt would be expected.

To perform a sedimentation analysis on protein requires an analytical ultracentrifuge, capable of spinning at very high accelerations (a few hundred thousand g) and simultaneously monitoring the UV absorption within the sample. The sedimentation of the protein can be monitored by measuring the absorption of the protein, typically in the UV regime, as a function of time.

5.2 Stall Force Experiments with Heterodimeric Kinesin

Experiments on phosphorylated kinesin homo-dimers, which were 80% phosphorylated, described a very heterogeneous sample, essentially consisting of three different populations. If a heterodimeric kinesin allowing only for the phosphorylation of one single motor head were prepared, this would reduce the number of populations to only two.

The stall force of 80% phosphorylated kinesin is 0.9 pN lower than the stall force of unphosphorylated protein. However, a 2 pN drop is observed for phosphomimetic kinesin-888 compared with wild-type or non-phosphorylatable kinesin. A phosphate group adds a charge of

-2e and would be expected to have a larger effect than a phosphomimic, which adds a charge of -1e. However, it is possible that to have a decreased stall force requires that both motor domains be phosphorylated.

To test the hypothesis that singly-phosphorylated kinesin do not have a decreased stall force, a heterodimeric kinesin in which only one motor domain can be phosphorylated could be used. Through using two different affinity purification steps, a kinesin in which one motor domain has an S175A mutation and the other is unmutated (residue 175 is the usual serine) could be created and later phosphorylated with JNK3.

References

1. Hackney, D. D. and M.F. Stock 2000. Kinesin's IAK tail domain inhibits initial microtubule-stimulated ADP release. *Nat. Cell Biol.* 2, 257-260.

Chapter 6: SHRImP Measurements of Ion Channels

6.1: Biological Motivation

The plasma membrane of a living cell is more than a static boundary that separates the cell from its environment. It is a highly dynamic structure that governs the interactions of a cell with the environment and other cells. Any signals from other cells or the environment that are destined for the cell interior must pass through the membrane. In animal cells, membrane proteins constitute approximately 30% of the cellular proteins and these proteins are the targets for approximately 40% of commercial pharmaceuticals (1). Knowledge of the structure and function of membrane proteins plays a crucial role in the development of new drugs (2, 3). Traditional structural studies of membrane proteins have relied on electron microscopy and x-ray crystallography of purified proteins that have been extracted from cells. However, membrane proteins have been notoriously difficult to crystallize and crystallization can result in structures with artifacts. For this reason, it is desirable to develop methods that provide information about the structure of membrane proteins in the plasma membranes of cells, their most natural environment.

Ion channels are a particularly interesting class of membrane proteins. These proteins allow cells to control the electric potential and propagation of electrical signals across their membranes. Ion channels can be divided into three groups according to the mechanism which triggers the opening and closing of the pore: mechanosensitive, voltage-gated, and ligand-gated. Mechanosensitive ion channels open and close in response to pressure, shear force, or physical displacement. They act as sensors for hearing, touch, balance and osmoregulation. Voltage-gated ion channels respond to changes in the membrane potential of cells. These are responsible for the propagation of electric signals in neurons. Ligand-gated ion channels open

and close in response to the binding of small molecules and are prevalent in neuron to neuron and in neuron to muscle connections.

Many ligand-gated ion channels are formed from several subunits, which can differ in identity. Knowing the possible combinations of subunits and their arrangement can offer insight into how the channels function as different subunits may impart different properties to the channel. For example, the AMPA (α -amino-3-hydroxy-5-methyl-4-isoxazolepropionic acid) and NMDA (N-methyl D-aspartate) receptors are two families of channels that are known to form from combinations of four subunits, but the geometry of the subunits is an open question. These channels are found in neurons in the central nervous system and play a crucial role in the formation of memories and learning (4, 5). The channels are always tetrameric, meaning they are formed from four different subunits. For both NMDA and AMPA receptors, only certain subunits combinations are possible.

To illustrate how questions of subunit geometry can arise, the heteromeric forms of the AMPA receptor can be considered. While homomeric AMPA receptors consisting of four identical subunits are possible, physiologically, most AMPA receptors are heteromers formed from different subunit types. In the hippocampus, the most common types are formed from two GluR1 subunits are two GluR2 subunits or two GluR2 and two GluR3 (5, 6). The extracellular domain of these subunits has a parallelogram-like shape with two fold symmetry which gives rise to four possible subunit geometries for these receptors as illustrated in figure 6.1

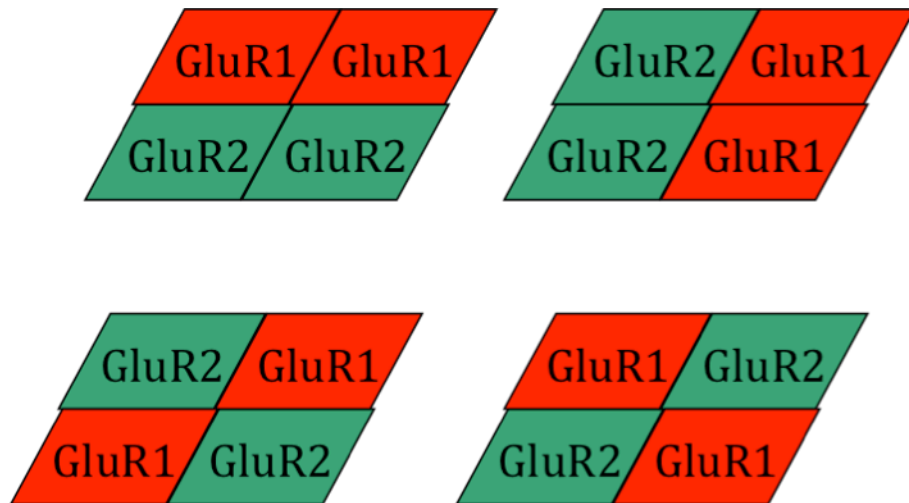


Figure 6.1: Possible heteromeric geometries for the extracellular domain of the AMPA receptor.

6.2: SHRImP Fluorescence Experiments

In our experiments, we attempted to apply fluorescence imaging to measure subunit geometries. The Single-molecule High Resolution Imaging with Photobleaching (SHRImP) technique was used (7). The SHRImP approach involves attaching fluorescent labels of the same dye to two of the receptor subunits at a time. After the first label photobleaches, the center of the point-spread function (PSF) of the remaining label can be located with nanometer accuracy using the FIONA technique, described previously. Subtracting the PSF of this dye from the images containing the fluorescence of two dyes allows us to also measure the position of the first label to photobleach with nanometer accuracy. From the positions of the two dyes, we can compute the distance between the fluorescent labels (Fig. 6.2).

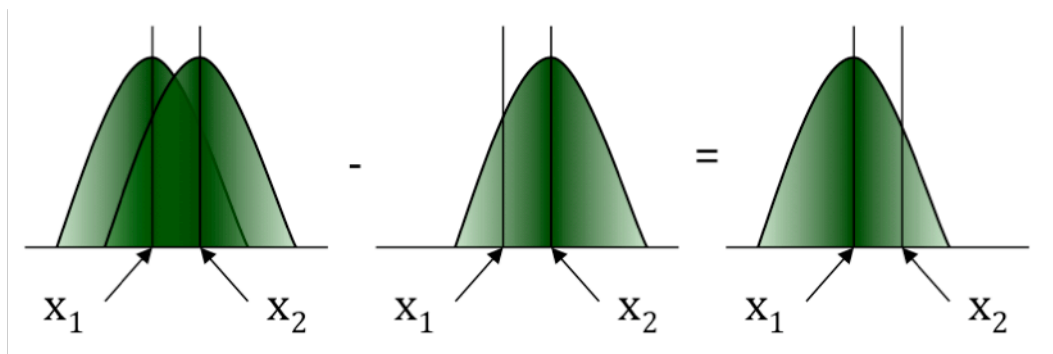


Figure 6.2: Illustration of the SHRIMP technique. The emission of two fluorophores, separated by less than the diffraction limit of light overlaps, making it difficult to measure the distance between them. However, after one of the fluorophores photobleaches, the FIONA technique can be applied to the remaining fluorophore to measure its position with high accuracy. The image of the remaining fluorophore is then subtracted from images containing both to construct an isolated image of the first fluorophore which can then be localized with FIONA.

We chose to use SHRIMP over fluorescence resonance energy transfer (FRET) or another distance measurement technique due to its range. SHRIMP has been successfully applied to measure distances between 10 and 30 nm with nanometer precision, giving it a wide dynamic range (7). FRET functions by measuring the energy transfer from a “donor” fluorophore to an “acceptor” fluorophore. For FRET, the energy transfer efficiency is related to the separation of the fluorophores, r , by

$$E = \frac{1}{1 + \left(\frac{r}{R_0}\right)^6}.$$

In contrast to SHRIMP, which has a broad dynamic range, the dynamic range of FRET is much smaller due to the dependence of the FRET signal on the inverse sixth power of the dye-dye separation. FRET measurements are typically limited to within a few nanometers of R_0 , the Forster radius at which the energy transfer efficiency between two dyes is 50%. Typical Forster radii are between 5 and 7 nm, giving FRET a dynamic range of around 4 to 10 nm. For AMPA receptors, the relevant separations of the subunits are 9 nm, across the short diagonal of the

parallelogram and 12 nm across the longer diagonal. These distances are larger than the range in which FRET functions well but within the range where SHRImp works.

6.3: Neuromuscular Junction Type Nicotinic Acetylcholine Receptor Test Case

Neuromuscular nicotinic acetylcholine receptors (NMJ-nAChRs) have been extensively studied and crystallized with 0.4 nm resolution (8). They play a role in muscle contraction. Acetylcholine binds to these receptors and causes them to open. Sodium ions enter through an open channel and set off a cascade of cell signaling that results in muscle contraction. The well-established structure of NMJ-nAChRs makes them a good control case. These are heteropentameric receptors that contain two α subunits, one β subunit, one δ , and either one γ or ϵ subunit depending on whether the receptor is an adult form (ϵ) or embryonic form (γ) (Figure 6.3). To perform SHRImp distance measurements, fluorescently labeled α -bungarotoxin can be attached to the receptors. This toxin, from *Bungarus multicinctus* (snake), binds naturally with a very high affinity at the α/γ (or α/ϵ) and α/δ receptor interfaces as can be seen in figure 6.3 (9). Bungarotoxin is commercially available with single fluorescent labels. These labels are attached at lysine residues. Our task is to measure the separation between two fluorescent bungarotoxin. Depending on the lysine residue, there is a 7.6 to 10 nm separation of the dyes, with an 8.6 nm separation corresponding to the most probable labeling of solvent-exposed lysines.

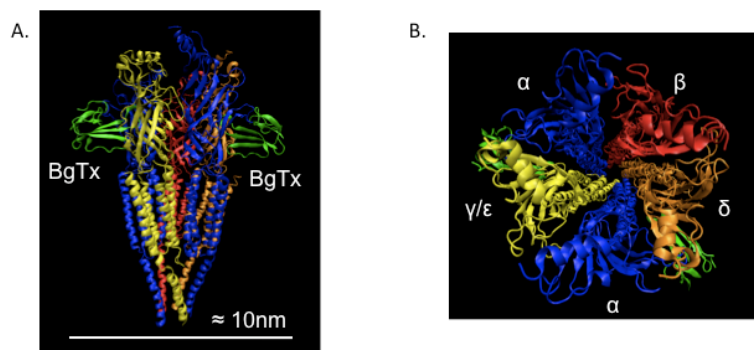


Figure 6.3: Side view (A) and top view (B) of the NMJ-nAChR. Bungarotoxin is shown in green. From PDB structures 2BG9 and 2QC1.

6.4 Materials and Methods for NMJ-nAChR SHRImP

6.4.1 Cell Culture

HEK 293 cells (ATCC) were maintained in DMEM (Gibco) supplemented with 10% fetal bovine serum, 4mM L. glutamine, 25U/ml penicillin and 25mg/ml streptomycin. Cells were grown to 80-90% confluency in 35mm glass-bottom dishes at 37C and 5% CO₂. One day prior to transfection, the media in the dishes was exchanged for media with no antibiotics. To express the NMJ-NAChRs, cells were transiently transfected using lipofectamine with cDNA for the α , β , δ , and γ subunits (a gift from William Green's laboratory at the University of Chicago). 10 ul of lipofectamine and 1ug α cDNA, and 0.5ug each of β , δ , and γ cDNA were added to the dishes 16-20 hours prior to experiments.

6.4.2 Receptor Labeling

Cells were incubated for 30 minutes in a blocking solution of OptiMem containing 8mg/ml BSA and 4 mg/ml casein at 37 °C. We initially used Alexa 647 conjugated bungarotoxin (Invitrogen) to label the receptors but later switched to CF633 due to its enhanced photostability. The bungarotoxin-dye conjugates were added to the blocking solution to a final concentration of 150 nM and cells were incubated in this solution for 30-45 minutes at 37C. To remove unbound bungarotoxin cells were washed 3 times in DBPS and then fixed for 30 minutes in a 4% paraformaldehyde solution in DPBS at room temperature. Following fixation, cells were washed 2 times in DPBS and imaged in DBPS.

6.4.3 Image Acquisition

Total internal reflection imaging of cells was performed on an Olympus IX71 microscope using a 100X 1.45 NA oil-immersion TIRF objective with a 633 nm excitation laser. A Semrock Brightline Di01-R635-25x36 dichroic mirror, a Semrock Brightline FF01-725/150-25 emission filter, and an

Andor iXon+ EMCCD camera were used to image the labeled receptors. Frame rates of 10-20 Hz were used for image acquisition.

6.4.4 Image Analysis

Fluorescent spots were analyzed with an IDL SHRImP analysis code written by Matt Gordon that was edited to include background subtraction of cell autofluorescence (7). The inclusion of background subtraction in the SHRImP analysis was necessary to remove the autofluorescence of the cells. The autofluorescence of the cells photobleached on a longer time scale than the fluorescent dyes, making it possible to average 10 images after the photobleaching of both dyes attached after a receptor and subtract this to remove the autofluorescent background. The counting of photobleaching steps was initially performed “by eye” but later an automated step-finding algorithm was implemented that employed a C++ hidden Markov model (HMM) program. To count the number of photobleaching steps in a fluorescent spot, the C++ code fit HMMs for 1-5 photobleaching steps to the intensity vs. time trace and used the Bayesian information criteria to select the best fit. Only traces which showed two clear photobleaching steps, corresponding to two fluorescent dyes, were used in the SHRImP analysis. The HMM analysis was done in collaboration with Nir Friedman and Karin Dahmen. The HMM used was adapted from code originally written by McKinney (10).

6.4.5 Data Fitting

Although the cells were fixed, this did not eliminate all motion of the proteins in the membrane. Formaldehyde fixes cells by forming methylene bridges between nitrogen atoms, which results in the cross-linking of proteins but does not affect lipids or carbohydrates in the membrane. This does not completely stop motion at the nanometer scale in the cell membrane and the residual motion of the proteins complicates a SHRImP experiment since the receptors can undergo some motion in the membrane in the time between when the pre- and post-photobleaching

images occur. We found this error to be of the same magnitude as the distances we attempted to measure. For this case, the distribution of distances had a non-Gaussian distribution.

Since distance is always defined to be positive measurement errors that overestimate the distance will be more common than errors that underestimate the distance. The exact form of the distribution was initially derived by Churchman, et al (11). The Churchman derivation assumes that the measured position of a fluorophore has a probability density function that is a Gaussian centered at the true position of the fluorophore,

$$p(x) = \frac{1}{2\pi\sigma^2} \exp\left(-\frac{(x - x_{true})^2}{2\sigma^2}\right).$$

If the true separation of two fluorophores is $\mu = x_1^{true} - x_2^{true}$, the probability density of measured separations, $r = x_1 - x_2$, is

$$p(r) = \frac{1}{2\pi\sigma^2} \exp\left(-\frac{(\mu - r)^2}{2\sigma^2}\right).$$

Writing the probability density function in radial coordinates in two dimensions for imaging in a plane and integrating over the angular coordinate yields

$$p(r) = \left(\frac{r}{\sigma^2}\right) \exp\left(-\frac{\mu^2 + r^2}{2\sigma^2}\right) I_0\left(\frac{r\mu}{\sigma^2}\right),$$

where I_0 is modified Bessel function of order zero. This distribution is right-shifted compared to a Gaussian distribution and the skew increases with the error, σ , in the localization of the each fluorophore.

6.5: Results

Figure 6.4 shows a typical image of a cell expressing CF633 labeled NMJ NACHRs and a characteristic intensity versus time photobleaching trace from a single fluorescent spot with and

without TIRF microscopy. The autofluorescence of the cell is significant and it can clearly be seen that TIRF is necessary to acquire clean images of the receptors in the membrane.

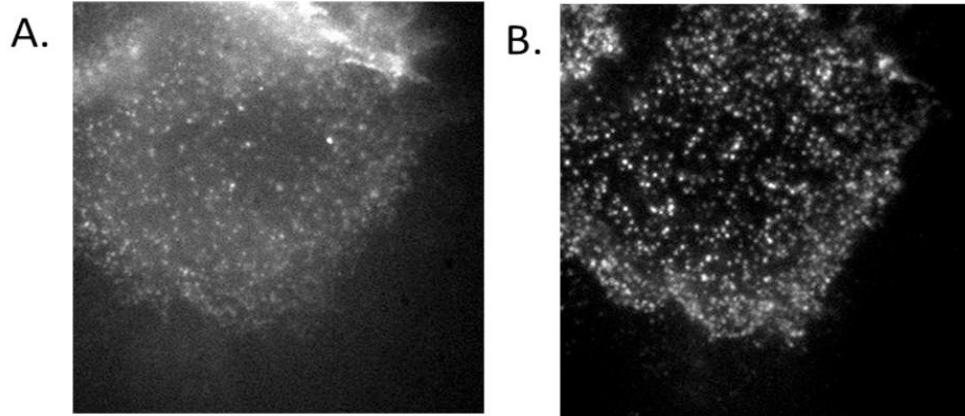


Figure 6.4: HEK cell with fluorescently labeled NMJ-nAChR receptors illuminated (A) with epifluorescence and (B) with TIRF.

The measured SHRIMP distances are plotted in figure 6.5 along with a fit. The distances were fit to the non-Gaussian, Churchman distribution plus a constant to account for background due to two spots on separate receptors,

$$p(r) = \left(\frac{r}{\sigma^2}\right) \exp\left(-\frac{\mu^2 + r^2}{2\sigma^2}\right) I_0\left(\frac{r\mu}{\sigma^2}\right) + C.$$

The addition of a constant background term to account for dyes that non-specifically stick to glass near each other was also found to be necessary in the original Gordon et al. study that established the SHRIMP technique (7).

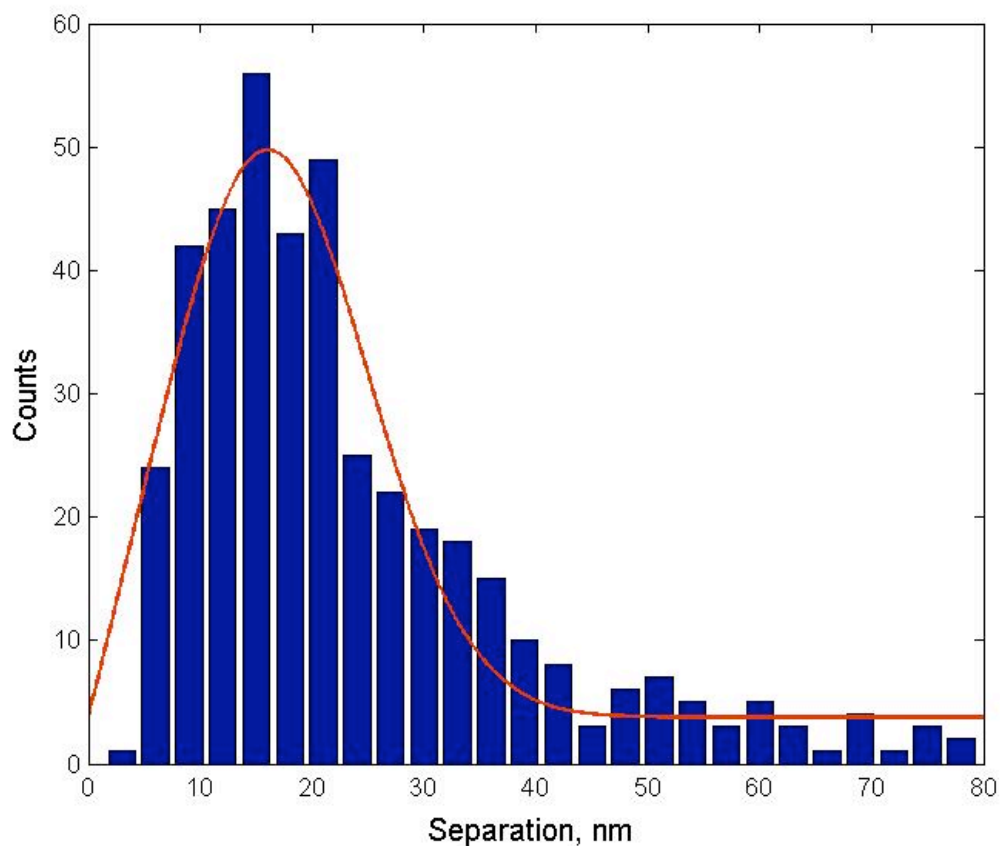


Figure 6.5: Distribution of measured dye separations on NMJ-nAChR using SHRIMP.

From the fit, we measured a true separation of $\mu = 13.8 \pm 1.0$ nm and a standard deviation of the location of individual fluorophores of $\sigma = 9.3 \pm 1.0$ nm.

From the crystal structure of the NMJ-nAChR, we would have expected to measure a smaller separation. Furthermore, from the photon counts of the individual dyes, we would expect a smaller error in fluorophore localization than the 9.3 nm fit to sigma. However, an examination of individual spots indicated that the receptors were not fixed at the nanometer scale, but rather most were motile within an area with a 10-50 nm radius on a timescale commensurate with our imaging rate of 10-100 Hz. We suspected that the chemical fixation was not sufficient to hold the receptors in place and this was corroborated by a previous study (12). If the receptors could be better immobilized, errors in localization would diminish and we may be able to measure

more accurate distances.

To test whether the motion we observed was due to the receptors but not drift of the microscope stage or camera, we examined different fluorescent spots from the same cell image. If drift were the underlying issue, we would expect the motion of the spots to be correlated. However, the spots appeared to move independently, suggesting that random motions within the cell membrane were to blame for the large localization errors (Figure 6.6).

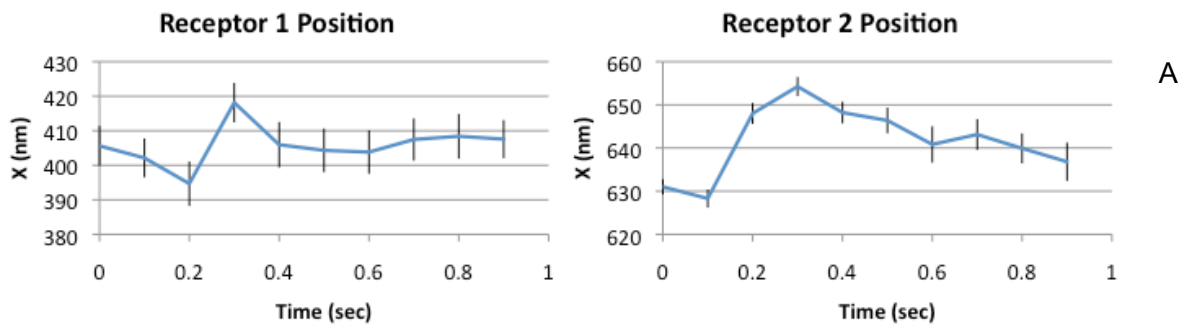


Figure 6.6: Position of two receptors in the same HEK cell as a function of time. The error bars represent the FIONA localization error in each frame. Both receptors move 10-20 nm/sec, but their motion is not coordinated.

variety of fixation techniques were explored, but none eliminated the receptor motion we observed in the membrane. We added 0.1% glutaraldehyde to the 4% formaldehyde mixture. Glutaraldehyde polymers are smaller than formaldehyde and a mixture of the two is commonly used to fix tissue for electron microscopy since glutaraldehyde can penetrate samples faster and more effectively than formaldehyde alone. However, this did not alter the random motion of the receptors. We also tried a variety of mounting agents to see whether these would better immobilize receptors. These were thick fluids that harden and are typically used to preserve fluorescently stained cell samples for long-term storage. We experimented with mowiol (0.1 g/ml in 50 mM Tris with 25% glycerol, pH=8.3), Fluoromount G (Southern Biotech), and Prolong Gold (Invitrogen). These media all had higher indices of refraction than water, which made achieving total internal reflection at the glass-media interface impossible. Instead, total

internal reflection imaging in these media required the use of quartz cover slips and a 1.65 NA objective. The NA objective required the use of ventilation to remove the toxic fumes from the high-NA microscopy oil. The use of media did not offer an improvement in fixation and also suffered from the high cost of quartz cover slips and hassle of ventilation.

Finally, we attempted to track the receptors and thus control their motion. The mAb35 antibody attaches to extracellular surface of the α subunits of the receptors (13). It does not compete with bungarotoxin for binding which binds at the α/δ and α/γ interfaces on the sides of the receptors. Our goal was to use fluorescent mAb35 to track receptors. It was not commercially available with fluorophores attached. We first attempted to use a fluorescent secondary antibody to mAb35. In these experiments, we first incubated cells in the presence of bungarotoxin with CF633 dye and unlabeled mab 35. We then added a secondary antibody labeled with R-PE (R-Phycoerythrin), a fluorophore that is spectrally distinct from CF633. These experiments were not successful. We could track the CF633 bungarotoxin and antibodies simultaneously, but did not see coordinated motion. Figure 6.7 shows an example trace of the positions of the antibody and CF633 over time. The error bars represent the FIONA accuracy for each frame.

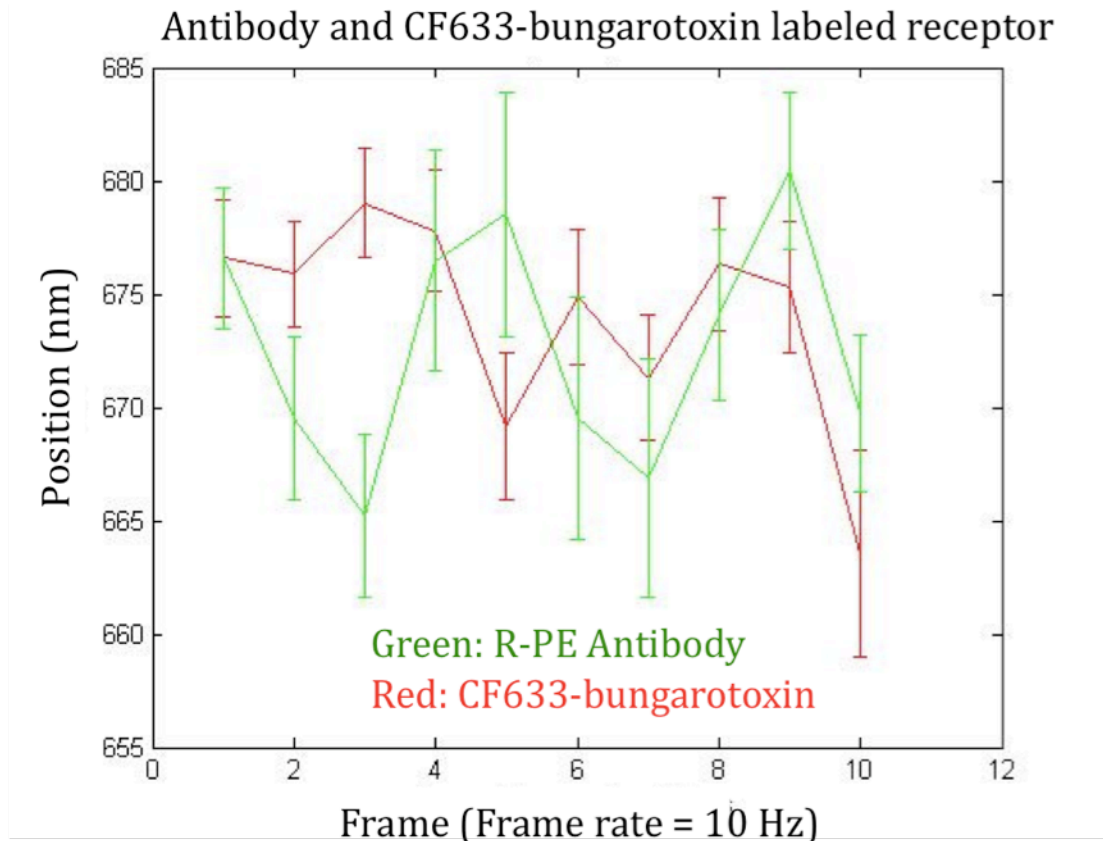


Figure 6.7: Dual-labeling of a single receptor. The green trace tracks the position of the R-PE labeled antibody as a function of time. The red trace is the position of the CF-633 labeled bungarotoxin. The error bars are the FIONA localization errors. It does not appear that the motion of the antibody and bungarotoxin labels are coordinated.

We suspected that the size of the R-PE secondary antibodies could be problematic. R-PE is a very large protein from the phycobiliprotein family and has a molecular weight of 240 kDa. Antibodies are 150kDa and 10-15 nm in size. The use of a secondary and a primary antibody to link R-PE to the channel created a very large antibody labeling complex, that was itself larger than the receptor protein. It is possible that this complex was flexible and the R-PE dye on the secondary antibody moved independently of the bungarotoxin-fluorophore attached to the receptor. If a fluorescent primary antibody were used instead, this would eliminate the need for a fluorescent secondary antibody and it is possible that a primary antibody alone would be less flexible. To test this, we attempted to label mAb35 directly with a fluorophore. We used an Alexa

555 antibody labeling kit (Invitrogen, A20187) but did not obtain good labeling.

6.5 Conclusions

While we were not able to resolve the issue of motion in the cell membrane that persisted after fixation to obtain a precise measurement of the distance across an NMJ-nAChR, our measurement of 14 nm for a true distance separation of ~8nm demonstrates that we are capable of measuring sub-diffraction limited distances associated with proteins in the cell membrane. With further improvement in fixation or tracking to correct for receptor motion, more accurate distances could be measured. SHRImP could be used to answer questions about receptor subunit geometry by directly studying proteins in their native environment of the cell membrane. With improved fixation, SHRImP could be applied to the AMPA receptor to solve the puzzle of how its different subunits are arranged.

References

1. Alberts, B., A. Johnson, J. Lewis, M. Raff, K. Roberts and P. Walter 2002. *Molecular Biology of the Cell*. 4th edition. Garland Science, New York.
2. Kemp, J. A. and R.M. McKernan 2002. NMDA receptor pathways as drug targets. *Nat. Neurosci.* 5, 1039-1042.
3. Paoletti, P. and J. Neyton 2007. NMDA receptor subunits: Function and pharmacology. *Current Opinion in Pharmacology.* 7, 39-47.
4. Pérez-Otaño, I. and M.D. Ehlers 2005. Homeostatic plasticity and NMDA receptor trafficking. *Trends Neurosci.* 28, 229-238.
5. Song, I. and R.L. Huganir 2002. Regulation of AMPA receptors during synaptic plasticity. *Trends Neurosci.* 25, 578-588.
6. Mansour, M., N. Nagarajan, R.B. Nehring, J.D. Clements and C. Rosenmund 2001. Heteromeric AMPA receptors assemble with a preferred subunit stoichiometry and spatial arrangement. *Neuron.* 32, 841-853.
7. Gordon, M. P., T. Ha and P.R. Selvin 2004. Single-molecule high-resolution imaging with photobleaching. *Proc. Natl. Acad. Sci. U. S. A.* 101, 6462-6465.
8. Unwin, N. 2005. Refined structure of the nicotinic acetylcholine receptor at 4Å resolution. *J.*

Mol. Biol. 346, 967-989.

9. Dellisanti, C. D., Y. Yao, J.C. Stroud, Z. Wang and L. Chen 2007. Crystal structure of the extracellular domain of nAChR α 1 bound to α -bungarotoxin at 1.94 Å resolution. *Nat. Neurosci.* 10, 953-962.
10. McKinney, S. A., C. Joo and T. Ha 2006. Analysis of single-molecule FRET trajectories using hidden markov modeling. *Biophys. J.* 91, 1941.
11. Stirling Churchman, L., H. Flyvbjerg and J.A. Spudich 2006. A non-gaussian distribution quantifies distances measured with fluorescence localization techniques. *Biophys. J.* 90, 668-671.
12. Tanaka, K. A., K.G. Suzuki, Y.M. Shirai, S.T. Shibutani, M.S. Miyahara, H. Tsuboi, M. Yahara, A. Yoshimura, S. Mayor and T.K. Fujiwara 2010. Membrane molecules mobile even after chemical fixation. *Nature Methods.* 7, 865-866.
13. Tzartos, S. J., A. Kokla, S.L. Walgrave and B.M. Conti-Tronconi 1988. Localization of the main immunogenic region of human muscle acetylcholine receptor to residues 67-76 of the alpha subunit. *Proceedings of the National Academy of Sciences.* 85, 2899-2903.

Appendix

Glossary of Biological Terms

α -bungarotoxin: A snake toxin that can be attached to a fluorescent dye and used to tightly bind the dye to proteins of interest.

Anterograde: Motion away from the center of a cell toward the periphery.

AMPA receptor: A type of ligand-gated ion channel in the nervous system involved in memory and learning.

ATP (adenosine triphosphate): The “energy currency” currency of the cell. It provides energy that is crucial for many reactions inside cells.

Axon: Long, narrow process that branches off a neuron cell body. Axons are responsible for transmitting chemical and electrical signals across synapses to neighboring neurons. Each neuron has one axon.

Dendrites: Long, narrow processes that branch off a neuron cell body. They are responsible for receiving chemical and electrical signals across synapses sent by axons of neighboring neurons. A single neuron can have hundreds of dendrites.

Dynein: A minus end directed microtubule motor.

Eukaryote: An organism made up of cells with nuclei.

FIONA (Fluorescent Imaging with One Nanometer Accuracy): A technique for localizing a fluorescent dye by fitting the emitted light to a 2-D Gaussian and finding the standard error of the mean.

GluR1/2/3/4: AMPA receptor subunits.

Isoform: One of a variety of forms of a protein that have only slight differences in sequence but share similar structures and functions.

JNK3 (c-Jun N-terminal kinase 3): A stress-signaling kinase. It is capable of phosphorylating kinesin-1.

Kinesin-1: A plus end directed microtubule motor.

Ligand: A small molecule that, in the context of ion channels, binds to a channel to regulate its opening and closing.

Kinase: An enzyme that is capable of phosphorylating other proteins.

Neuron: Cells that are specialized in communicating information in animals. They can receive, process, and transmit chemical and electric signals.

Microtubule: Part of the cytoskeleton, these make up “highways” within eukaryotic cells.

Minus end: End of the microtubule with exposed alpha tubulin. In cells, minus ends tend to point toward the nucleus.

Motor domain: The part of the kinesin protein that binds microtubules and hydrolyzes ATP.

Neuromuscular junction (NMJ) nicotinic acetylcholine receptor nAChR: A ligand-gated ion channel that exists at the junction between central nervous system and muscle cells. It has two natural bungarotoxin binding sites.

NMDA receptor: A type of ligand-gated ion channel in the nervous system involved in memory and learning.

Phosphorylation: Attachment of a phosphate group (PO_4) to a protein.

Plus end: End of the microtubule with exposed beta tubulin. In cells, plus ends tend to point toward the periphery, away from the nucleus.

Processivity: The ability of a motor protein such as kinesin or dynein to take multiple steps along a track before dissociating.

Residue: An amino acid within a protein. Residues are numbered starting with "1" at the N-terminus, which is the end of a protein with an exposed amino group.

Retrograde: Motion toward the center (nucleus) of a cell.

SHRIMP (Single Molecule High-resolution IMaging with Photobleaching): A distance measurement technique that involves using two dyes of the same color. After one of the dyes photobleaches, the fluorescence of the remaining dye is subtracted from the fluorescence of the two dyes before the photobleach to reconstruct the first dye. Both dyes are localized with FIONA and the distance between them is measured.

Stall force: The maximum force that a molecular motor can exert.

Tubulin: The building blocks of microtubules. Tubulin protein comes in two forms, called alpha and beta tubulin.